HZDR-010

TWO-PHASE FLOW EXPERIMENTS IN A MODEL OF THE HOT LEG OF A PRESSURISED WATER REACTOR

Tobias Seidel, Christophe Vallée,
Dirk Lucas, Matthias Beyer, Deendarlianto

Technical Report

Wissenschaftlich-Technische Berichte
HZDR-010 · ISSN 1437-322X

WISSENSCHAFTLICH-
TECHNISCHE BERICHTE

HZDR
HELMHOLTZ
ZENTRUM DRESDEN
ROSSENDORF

Wissenschaftlich-Technische Berichte
HZDR-010
September 2011

Tobias Seidel, Christophe Vallée,
Dirk Lucas, Matthias Beyer, Deendarlianto

Two-phase flow experiments in a model of the hot leg of a pressurised water reactor

Technical Report

HZDR
HELMHOLTZ
ZENTRUM DRESDEN
ROSSENDORF

Technischer Fachbericht

Zweiphasenströmungs-Experimente in einem Modell des heißen Strangs eines Druckwasserreaktors

Technical Report

Two-phase flow experiments in a model of the hot leg of a pressurised water reactor

Reaktorsicherheitsforschung-Vorhaben-Nr./ Reactor Safety Research-project No.:	150 1329
Vorhabenstitel:	**TOPFLOW-Experimente, Modellentwicklung und Validierung von CFD-Codes für Wasser-Dampf-Strömungen mit Phasenübergang**
Project Title:	**TOPFLOW-Experiments, development and validation of CFD models for steam-water flows with phase transfer**
Autoren / Authors:	**Tobias Seidel, Christophe Vallée, Dirk Lucas, Matthias Beyer, Deendarlianto**
Dienststelle der Autoren / Performing Organisation:	**Helmholtz-Zentrum Dresden-Rossendorf e.V. Institut für Sicherheitsforschung**
Berichtsdatum / Publication Date	**September 2011**
Berichts-Nr. / Report-No.:	**HZDR-010**
Überarbeitung von / Revision of:	**FZD-531**

Das diesem Bericht zugrundeliegende Vorhaben wurde mit Mitteln des Bundesministeriums für Wirtschaft und Technologie unter dem Förderkennzeichen 150 1329 gefördert. Die Verantwortung für den Inhalt dieser Veröffentlichung liegt bei den Autoren.

Berichtsblatt

1. ISBN oder ISSN	2. Berichtsart Technischer Fachbericht

3a. Titel des Berichts

Zweiphasenströmungs-Experimente in einem Modell des heißen Strangs eines Druckwasserreaktors

3b. Titel der Publikation

4a. Autoren des Berichts (Name, Vorname(n)) Tobias Seidel, Christophe Vallée, Dirk Lucas, Matthias Beyer, Deendarlianto	5. Abschlussdatum des Vorhabens 30.09.2010
4b. Autoren der Publikation (Name, Vorname(n))	6. Veröffentlichungsdatum September 2011
	7. Form der Publikation Broschüre
8. Durchführende Institution(en) (Name, Adresse) Helmholtz-Zentrum Dresden-Rossendorf e.V. Institut für Sicherheitsforschung Postfach 510119 01314 Dresden	9. Ber.Nr. Durchführende Institution HZDR-010
	10. Förderkennzeichen 150 1329
	11a. Seitenzahl Bericht 87
	11b. Seitenzahl Publikation 367 (inkl. Anhang)
13. Fördernde Institution (Name, Adresse) Bundesministerium für Wirtschaft und Technologie (BMWi) 11019 Berlin	12. Literaturangaben 31
	14. Tabellen 9
	15. Abbildungen 67

16. Zusätzliche Angaben

revision des Berichts FZD-531

17. Vorgelegt bei (Titel, Ort, Datum)

18. Kurzreferat

Zur Untersuchung von Zweiphasenströmungen in einer reaktortypischen Geometrie wurde am HZDR ein Modell des heißen Strangs eines Druckwasserreaktors aufgebaut. Ziel der Experimente war die Bereitstellung geeigneter Daten für die CFD Validierung. Das Heißstrangmodell wurde in der Druckkammer der TOPFLOW-Anlage betrieben, in der Hochdruckexperimente im Druckgleichgewicht mit der Behälteratmosphäre durchgeführt werden können. Diese Technologie ermöglicht es die Zweiphasenströmung auch bei reaktornahen Druckbedingungen über große Fenster zu beobachten. Um die Visualisierungsmöglichkeiten zu optimieren wurde der Teststreckenquerschnitt rechteckig gestaltet.

Versuche mit Luft und Wasser fanden bei 1,5 und 3,0 bar und Raumtemperatur statt während Dampf/Wasser-Experimente bei 15, 30 und 50 bar sowie der jeweiligen Sättigungstemperatur (bis zu 264°C) durchgeführt wurden. Die insgesamt 194 Versuche unterteilen sich in vier Versuchstypen: stationärer Gleichstrom, Gegenstrom, Strömung ohne Wassereinspeisung und transiente Gegenstrombegrenzungsexperimente.

Dieser Bericht beinhaltet eine detaillierte Dokumentation der Experimente mit Informationen zum Versuchsaufbau, zur Versuchsdurchführung, Testmatrix und Kalibrierung der Messgeräte. Die verfügbaren Daten werden dargestellt und die für jedes Experiment erstellten Datenblätter liefern einen Überblick über die wichtigsten Parameter. Mit den Füllstandshistogrammen für Gleichstromexperimente kann die Strömung im heißen Strang charakterisiert werden. Diese Häufigkeitsverteilungsfunktionen können für den quantitativen Vergleich mit CFD-Simulationen genutzt werden. Außerdem wurde die Flutcharakteristik des Heißstrangmodells in den Wallis- und Kutateladze-Diagrammen dargestellt. Dabei stellte sich heraus, dass diese bei Dampf/Wasser und Luft/Wasser-Experimenten unterschiedlich ausfällt. Daraufhin wird ein modifizierter Wallis-Parameter vorgeschlagen, der den Einfluss der Viskosität berücksichtigt.

19. Schlagwörter

Zweiphasenströmung, Heißstrang, Gegenstrombegrenzung, Walliskorrelation

20. Verlag	21. Preis

Document Control Sheet

1. ISBN or ISSN	2. Type of Report Technical Report
3a. Report Title Two-phase flow experiments in a model of the hot leg of a pressurised water reactor	
3b. Title of Publication	
4a. Author(s) of the Report (Family Name, First Name(s)) Tobias Seidel, Christophe Vallée, Dirk Lucas, Matthias Beyer, Deendarlianto	5. End of Project 30.09.2010
	6. Publication Date Februar 2010
4b. Author(s) of the Publication (Family Name, First Name(s))	7. Form of Publication Booklet
8. Performing Organisation(s) (Name, Address) Helmholtz-Zentrum Dresden-Rossendorf e.V. Institut für Sicherheitsforschung Postfach 510119 01314 Dresden	9. Originator's Report No. HZDR-010
	10. Reference No. *) 150 1329
	11a. No. of Pages Report 87
	11b. No. of Pages Publication 367 (incl. Appendix)
13. Sponsoring Agency (Name, Address) Bundesministerium für Wirtschaft und Technologie (BMWi) 11019 Berlin	12. No. of References 31
	14. No. of Tables 9
	15. No. of Figures 67
16. Supplementary Notes revision of the technical report FZD-531	
17. Presented at (Title, Place, Date)	

18. Abstract

In order to investigate the two-phase flow behaviour in a complex reactor-typical geometry and to supply suitable data for CFD code validation, a model of the hot leg of a pressurised water reactor was built at HZDR. The hot leg model is operated in the pressure chamber of the TOPFLOW test facility, which is used to perform high-pressure experiments under pressure equilibrium with the inside atmosphere of the chamber. This technique makes it possible to visualise the two-phase flow through large windows, also at reactor-typical pressure levels. In order to optimise the optical observation possibilities, the test section was designed with a rectangular cross-section.

Experiments were performed with air and water at 1.5 and 3.0 bar at room temperature as well as with steam and water at 15, 30 and 50 bar and the corresponding saturation temperature (i.e. up to 264℃). The total of 194 runs are divided into 4 types of experiments covering stationary co-current flow, counter-current flow, flow without water circulation and transient counter-current flow limitation (CCFL) experiments.

This report provides a detailed documentation of the experiments including information on the experimental setup, experimental procedure, test matrix and on the calibration of the measuring devices. The available data is described and data sheets were arranged for each experiment in order to give an overview of the most important parameters. For the co-current flow experiments, water level histograms were arranged and used to characterise the flow in the hot leg. In fact, the form of the probability distribution was found to be sensitive to the boundary conditions and, therefore, is useful for the CFD comparison. Furthermore, the flooding characteristics of the hot leg model plotted in terms of the classical Wallis parameter or Kutateladze number were found to fail to properly correlate the data of the air/water and steam/water series. Therefore, a modified Wallis parameter is proposed, which takes the effect of viscosity into account.

19. Keywords two-phase flow, hot leg, counter-current flow limitation (CCFL), Wallis correlation	
20. Publisher	21. Price

Contents

Appendix (on CD)

1 Introduction

1.1 Background

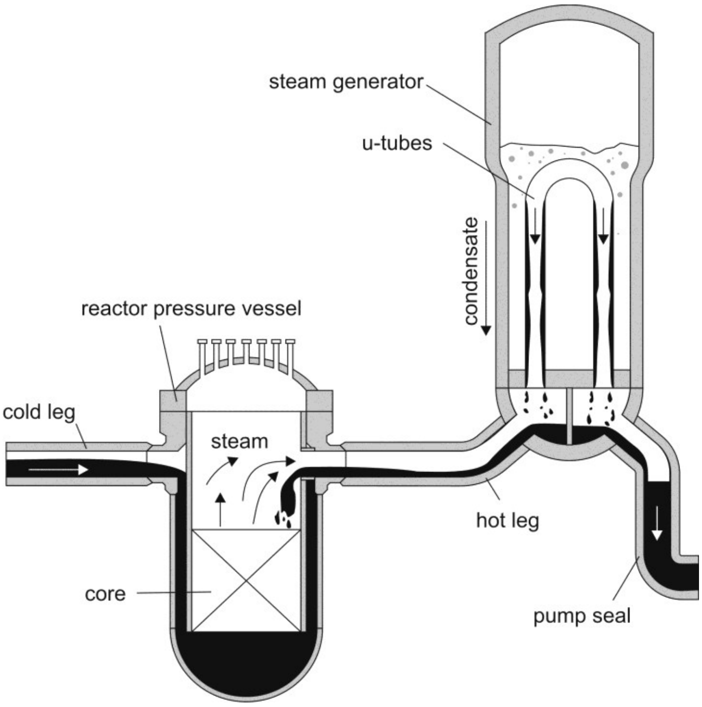

Fig. 1.1 Scheme of the Primary loop during reflux condenser mode

In the event of a loss-of-coolant-accident (LOCA) in a pressurised water reactor (PWR), emergency strategies have to be mapped out, in order to guarantee a safe removal of heat from the reactor core, also in case of component breakdown. Different scenarios of small break LOCA (Tusheva et al. 2009), e.g. with partial failure of the high-pressure emergency core cooling systems and main feed pumps, a natural circulation starts in the primary circuit. This allows the heat removal, also if steam is generated in the reactor core due to the depressurisation of the primary circuit. However, if the water level in the reactor pressure vessel (RPV) decreases down to the level of the hot leg nozzle steam flows towards the steam generator (SG). This may cause a breakdown of the natural circulation. In case of a water level below the hot leg nozzle, pure steam enters the hot leg and a so-called reflux condenser mode may establish. In this mode the steam coming from the RPV, condensates in the vertical U-tubes of the steam generator. In each half of the steam generator, the condensate flows down the tube in which it has been formed (see figure 1.1). Therefore, about one-half of the condensate flows as usual over the pump to the downcomer, whereas the other half flows over the hot leg back to the upper plenum. In the hot leg, the condensate has to flow in counter-current to the steam.

The horizontal stratified counter-current flow of condensate and steam is only stable for a certain range of flow rates. If the steam flow increases too high, the condensate is clogged in the hot leg. This is the beginning of the counter-current flow limitation (CCFL): the liquid is carried over by the steam and partially entrained in opposite direction to the steam generator. Therefore, the hot leg and steam generator are flooded, which further decreases the water level in the RPV and, therefore, lowers the core cooling. In case of an additional increase of the steam flow, the condensate flow is completely blocked and the cooling of the reactor core from the hot leg is impossible.

For the validation and optimisation of accident management strategies, such transient scenarios are reproduced in dedicated facilities or rather simulated numerically. The use of one-dimensional system codes is state of the art, but these programs are not able to predict the local flow conditions. Instead, they apply empirical correlations obtained from special experiments. The co- and counter-current flow in a hot leg geometry and especially CCFL conditions are dominated particularly by 3D effects, which require the use of a computational fluid dynamics (CFD) approach. However, the actual CFD codes applied to two-phase flows are not yet mature, i.e. they still do not meet the high level of confidence needed in the field of nuclear reactor safety. Moreover, the developed models and closure laws embedded in CFD must be validated to allow reliable simulations. Therefore, high-resolution experimental data at reactor typical boundary conditions is needed for comparison with CFD calculations.

The qualification of CFD codes for two-phase flows is one of the main tasks addressed by the so-called German CFD alliance, initiated by the Gesellschaft für Anlagen und Reaktorsicherheit (GRS). It should prepare CFD codes for their use in safety analyses in future. The German CFD alliance coordinates the corresponding research activities at research centres, university groups, code developers and nuclear regulating authorities. Stratified flows in horizontal components and CCFL are special tasks in the target specification for these activities. From the modelling, open questions especially concern the momentum transfer at the free interface and the coupling of turbulent fields. Both problems are closely connected with local structure of the interface. Therefore, new experiments should include detailed measurements or observations of the local interface.

One contribution of FZD to this problem was the generic investigations performed in the Horizontal Air/Water Channel (HAWAC) in the frame of a previous project. Experimental results obtained principally with optical measuring systems were used for the validation of the CFD-code *ANSYS-CFX* (Vallée at al., 2007). The hot leg experiments described in this report are the continuation of this work, however, these are more closely connected with the industrial application. In fact, the investigations were done in a typical pressurised water reactor geometry and at typical LOCA boundary conditions.

1.2 Previous investigations in hot leg geometries

1.2.1 Two-phase natural circulation

Several experimental investigations of co-current flows in hot legs, simulating the two-phase natural circulation, were performed in dedicated test facilities over the last decades. Gardner (1989) for example performed experiments with air and water at atmospheric pressure conditions. The used acrylic-glass test facility reproduces the hot leg and a part of the steam generator of the British “Sizewell B” nuclear power station (design based on the *Westinghouse* 4-loop PWR) at a scale of 1:8.8. From visual observations of the two-phase flow in the hot leg, a flow regime map was arranged in terms of the non-dimensional Wallis parameter. The flow map includes the transition from stratified to intermittent flow regimes, the presence of a hydraulic jump in the test section as well as the onset of spray formation. Furthermore, the water level measured in the reactor pressure vessel was compared with the results obtained using a model developed previously by Gardner (1988) for the two-phase discharge through a horizontal break. This model was found to be also adapted to the co-current flow conditions through a hot leg geometry.

Furthermore, natural circulation experiments were performed at the ROSA-IV Large Scale Test Facility (LSTF), a full-pressure and full-height model of a *Westinghouse* 4-loop PWR with a volumetric scale of 1:48. The test facility includes two symmetric primary loops with active steam generators and main coolant pumps. The hot and cold legs are dimensioned to conserve the volumetric scale of 1:24

as well as the ratio of length to square root of the diameter ($L/\sqrt{D}$) in order reproduce accurately the two-phase flow regime transitions. Kukita et al. (1989) and Asaka & Kukita (1996) reported about results focused on the main characteristics of the two-phase flow in the hot leg during natural circulation at pressures of about 7 MPa. They observed a stratified flow pattern in the horizontal part of the hot leg which turns into intermittent flow regimes in the riser. At high water flow rates, a hydraulic jump as the discontinuous transition between super- and subcritical flow was noticed at the connection to the riser. It was found that the transition to supercritical flow dependents on the steam flow rate. Furthermore, Asaka & Kukita (1996) extended the model developed by Gardner (1988) in order to predict the transition from sub- to supercritical flow conditions as well as the water level in the hot leg under supercritical conditions.

Moreover, extensive steam/water experiments under increased pressure conditions were performed in the Upper Plenum Test Facility (UPTF), which simulates the primary circuit of a PWR at the original power plant scale. From 1991 to 1997, transient small break LOCA scenarios and accident management measures were investigated in the frame of the UPTF TRAM (TRansient Accident Management) program. The flow regimes in the hot leg during two-phase natural circulation were examined during the TRAM-A2 experimental series (Weiss, 1992). Different combination of steam and water flow rates were injected in the core simulator at system pressures of 3, 5 and 15 bar in order to show the development of stratified two-phase flows in the hot leg. It was found that the flow regime in the hot leg as well as in the riser changes with the water flow rate. The sub- and supercritical flow regimes as defined by Gardner (1989) were observed. However, the results show that the generic flow regime maps for horizontal channels are not adapted for the particular geometry of the hot leg. In fact, during stationary experiments, only stratified flow regimes were observed, whereas intermittent flow regimes were also predicted by these maps. Therefore, a qualitative flow regime map was developed for the hot leg geometry.

In order to precise the observations made previously in particular at UPTF, Petritsch & Mewes (1999) built a large scale acrylic-glass test facility for air/water experiments at atmospheric pressure and room temperature. In a first series of experiments, the flow map of the facility was determined for a horizontal pipe only, with an inner diameter of 0.441 m. Petritsch & Mewes found similar results compared to the classical flow regime maps for horizontal two-phase flows, although these were obtained in systems with significantly smaller pipe diameter and higher length. In a second stage, the experiments were repeated with a hot leg geometry (i.e. with a riser and steam generator simulator) of the same inner diameter, corresponding to a scale of 1:1.7. The obtained results were very different to those for horizontal pipes, pointing out the important influence of the riser and steam generator on the flow in the hot leg. Consequently, a specific flow regime map was proposed for this geometry.

1.2.2 Reflux-condenser cooling mode and counter-current flow limitation

Wallis (1969) studied the counter-current gas liquid-flow in vertical pipes first. He formulated the basic principle that the boundary between possible and impossible velocities can be found in a diagram of specially adapted dimensionless parameters. Because of the significance of this conclusion, the used dimensionless superficial velocity was called Wallis parameter afterwards. Compared to the Froude number (1.1, h – depth of liquid, u – velocity, g – gravity acceleration) the Wallis parameter (1.2, D –

Diameter, ρ_k - density of k, $k \in \{L,G\}$ - phase liquid or gas) is defined for closed pipes and channels with the superficial velocity j_k and takes the effect of the density difference in account.

$$Fr = \frac{u}{\sqrt{g \cdot h}} \tag{1.1}$$

$$J_k^{\;*} = \frac{j_k}{\sqrt{g \cdot D}} \sqrt{\frac{\rho_k}{\rho_L - \rho_G}} \tag{1.2}$$

Wallis also formulated the flooding curve (1.3).

$$J_G^{\;*1/2} + m \cdot J_L^{\;*1/2} = C \tag{1.3}$$

Stable counter-current flow is observed with smaller velocity. Flow conditions on the flooding curve are characterized by a limited liquid flow rate for a given gas flow rate, while the flow velocity combinations above are not stable.

The first detailed investigations on counter-current flow limitation in a hot leg typical geometry (i.e. a horizontal conduit connected to a riser) date back to the late seventies. Richter et al. (1978) performed air/water experiments in a scaled down model of the hot leg of a PWR. The test section was made of acrylic glass in order to allow visual observation of the two-phase flow. They proposed to correlate the obtained flooding data with the Wallis-correlation according to equation 1.3 with the parameters $m = 1$ and $C = 0{,}7$. Krolewski (1980) established the experimental flooding characteristic of five different hot leg geometries with air and water. She shows that the characteristic of the CCFL depends significantly on the angle of the riser as well as on the inlet and outlet geometry.

Later on, Ohnuki (1986) performed counter-current flow limitation experiments in a horizontal pipe connected to an inclined riser with air/water and saturated steam/water, both under atmospheric pressure conditions. From his results, Ohnuki concluded that the flooding characteristic in terms of Wallis parameters is independent from the fluid combination. Furthermore, he varied the most important geometrical aspects of the hot leg: the conduit diameter, the length of the straight pipes and the angle of the riser. As a result of his investigations, Ohnuki proposed an empirical correlation (equation 1.4) to predict the onset of flooding by using the Wallis parameter, in which the constant C is a function of the length *L* to diameter *D* ratio of the horizontal pipe as well as of the length *I* of the inclined riser.

$$m = 0{,}75\,;\; C = 0{,}88 - 0.066 \cdot \ln\left(\frac{L}{D \cdot I} \cdot [m]\right) \tag{1.4}$$

At the same time, Wan investigated the CCFL in a horizontal pipe connected with a 90° elbow to a vertical one, which reproduces the geometry of the coolant inlet and outlet lines of a CANDU reactor. Experiments were performed at atmospheric pressure with air and water (Wan & Krishnan, 1986) as well as with steam and slightly subcooled water (Wan, 1986). In order to investigate the influence of condensation effects, the water subcooling was varied during the steam experiments between 0 and 6 K. However, the results obtained with each fluid combination were published separately and never compared with each other.

Furthermore, extensive steam/water CCFL experiments under increased pressure conditions were performed in the Upper Plenum Test Facility (UPTF), which simulates the primary circuit of a PWR at full scale. The experiments related by Weiss & Hertlein (1988) simulate the reflux condenser mode after a small break LOCA. These were conducted at pressures of 3 and 15 bars and saturation conditions. A comparison of the results with the correlations of Richter et al. and Ohnuki confirmed that the Wallis parameter allows a proper geometrical scaling of the effects of counter-current flow limitation.

Moreover, reflux condenser experiments were performed in the German integral test facility PKL at a pressure of 40 bar (Schmidt & Limprecht, 1991). The power of the reactor core simulator was increased stepwise to reach CCFL in the hot leg or steam generator. As a result, the distribution of the coolant in the primary circuit was measured in function of the core power. However, the flooding characteristic was not determined.

More recently, Kim and No (2002) have merged in one database the experimental results obtained by eight different research groups, which were published between 1986 and 1999. The database includes cold air/water as well as steam/water experiments. By the regression through a total of 356 data points, Kim and No proposed a flooding correlation as function of the length to diameter ratio of the horizontal part of the hot leg. The prediction error of the correlation was evaluated against the considered database to 8.7%.

Minami et al. (2008) performed experiments in a model of the hot leg of a pressurised water reactor with rectangular cross-section. The test section is made of acrylic glass and the fluids used were air and water at atmospheric pressure and room temperature. The study of Minami et al. focuses on the flow patterns observed in the hot leg and the results were compared with the flooding characteristic of the test section.

Furthermore, Gargallo et al. (2005) investigated the occurrence of two-phase counter-current flow limitation for the German ECC injection system “Hutze”. In the WENKA test facility, a closed channel with rectangular cross-section, a super-critical water flow was injected in counter-current to a constant airflow. By reducing the water flow rate, a hydraulic jump occurs in the test-section, which was found to be the initiator for a water flow reversal. Consequently, the water flow rate in the direction of the RPV is limited by the gas flow.

1.2.3 Lacks of available data for CFD validation

This non-exhaustive review of the literature shows that previous investigations cover many aspects of co- and counter-current flows including CCFL in hot leg typical geometries. However, the goal of most of the previous experiments was the development and validation of one-dimensional system codes. Therefore, the available data mainly focuses on macroscopic effects, which do not allow a detailed validation of the CFD codes. Furthermore, to the knowledge of the authors, no experiments were performed in one facility with the fluid combinations air/water and steam/water over a wide range of pressure and temperature conditions. However, Damerell & Simons (1993) indicated that the reflux condenser mode could appear at primary system pressures of up to 80 bars. Therefore, the CCFL experiments performed in the hot leg model of FZD provide improved comparison possibilities between air/water data at low pressure and room temperature on the one hand and steam/water data at pressures of up to 50 bars on the other hand.

For the CFD code validation, it is very important to ensure a good access for measurements of distributed flow parameters. In many facilities where CCFL experiments were carried out previously, optical access was possible (e.g. acrylic-glass test section, sight glass). The observation of the flow was mainly used to support the interpretation of the results. The few pictures of the flow published in the past from experiments in hot leg typical geometries do not allow recognising detailed structures like bubbles and droplets. Furthermore, since these investigations were performed in pipes, the three-dimensional shape of the interfacial structure limited the optical quality. For these reasons, the new test section build for this work was optimized for the application of optical observation. The flooding experiments reported in this work were conducted in a flat model of a PWR hot leg. The objective of these experiments was to get a data set of high-resolution pictures of the flow taken during counter-current flow limitation. The high-speed video observation can be useful for the understanding of the flow phenomena involved in flooding as well as for CFD code validation purposes.

The flow types investigated comprise co-current, counter-current flows, flows without water circulation and CCFL experiments. The latter were performed before and around the onset of flooding. The fluids used are air and water as well as steam and water at pressures of up to 50 bars. The measured global parameters like water levels and pressure drop are analysed in order to characterise the flow. Furthermore, the comparison with detailed visual observations is used to explain the flow structure.

1.3 Overview

The present report is an overview of all the hot-leg model experiments in the TOPFLOW facility. It gives an extensive introduction in the facility and all the measurement principles and closes with the first steps for analysing the results.

In the first part, the construction of the TOPFLOW facility in general and the hot-leg model test-section in particular is described focusing on the pressurised tank technology and the special observation technique. Afterwards, the measurement equipment is described with detailed information about the calibration and the synchronisation between the two acquisition systems. Furthermore, the experimental procedures for start-up and operation are specified. The different types of experiments are distinguished between the overall mass flow directions. The access and type of available data is described parallel to the accuracy estimation. Water level plots are introduced for the assessment of the experimental quality.

The most important part is the review of the experimental results for each experiment type, along with the description of exemplary experiments. For the co-current experiments, probability density functions are analysed. Counter current flow limitation experiments are more extensively treated. The flooding characteristic of the hot leg model is determined and plotted in terms of different non-dimensional parameters. Finally, the proposed non-dimensional parameter, which succeeds to cover all the experimental series, is discussed with the results of previous investigations.

2 Construction

2.1 *Fluid supply systems of the TOPFLOW facility*

The thermal hydraulic test facility TOPFLOW (Transient **T**w**O** **P**hase **FLOW** test facility) is one of the major research facilities at Forschungszentrum Dresden - Rossendorf, designed for studying thermal hydraulic phenomena of two-phase flows at high pressures and temperatures. An electrical steam generator with a power of 4 MW represents the heat source and the heat sink consists of a blow-down tank to quench the exhaust media (Fig. 2.1). These are the two main infrastructural components of TOPFLOW (see Schaffrath 2001, Prasser 2006 and Beyer 2004). Between these two ends, the flow passes through various test rigs, which makes TOPFLOW a multi-purpose test facility.

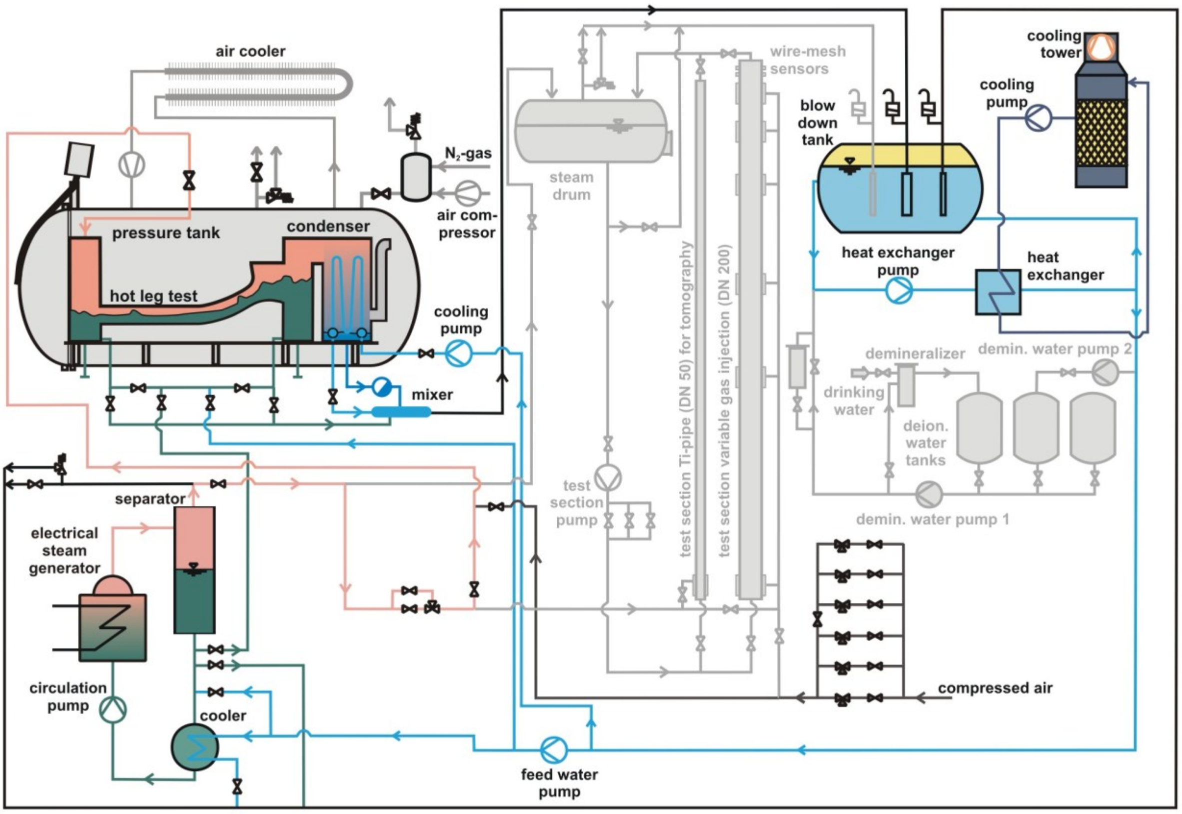

Fig. 2.1 General scheme of the TOPFLOW facility, systems used for the hot leg experiments are shown coloured

At the end of 2002, the facility was completed and reached its working parameters of 7 MPa and the corresponding saturation temperature of 286 °C. The maximum steam mass flow is about 1.4 kg/s and the maximum water flow into the test section circuit is 50 kg/s. Within former projects, the TOPFLOW facility was mainly used for the analysis of two-phase flows in vertical pipes with different inner diameter and with various kinds of gas injection modules. (see Prasser et al. 2005, 2008)

For the hot leg experiments, a new wing (Fig. 2.2) had to be added to the TOPFLOW building, where a pressure vessel was installed and supplied with the necessary systems and piping.

Fig. 2.2 New wing of the TOPFLOW building

Figure 2.1 shows the main components and circuits of the TOPFLOW facility, which was used for the air/water and steam/water experiments with stratified, flows in the hot leg model. The saturated steam for these tests was generated in the steam generator circuit (see the bottom left corner in Fig. 2.1). The main component of this system is an electrical heater. It consists of 24 directly heated stainless steel pipes, supplied from a power transformer. In these pipes, a maximum of 15% of the circulating water evaporates. The capacity of the steam generator can be adjusted coarse into 9 modes between 0.5 and 3.9 MW by a switch on the transformer and it is set precisely by the cooler (Fig. 2.1). After the separation, the steam flows to the test rigs controlled by 2 parallel units, each consisting of a flow meter and a regulating valve.

The steam generator circuit also supplied the saturated water (maximum 1 kg /s) for the hot leg tests. It was taken from the bottom of the separator and directed to one of the test sections separators. By that, it was possible to set co-current or counter-current flows in the test section (see Chapter 4.2). The mass flow diverted from the steam generator circuit (steam and saturated water) was compensated with feed water from the blow down tank. The entire facility is filled with chemically demineralised water with a conductivity smaller then 5 µS/cm.

In the case of air/water experiments, the gas was supplied by the compressed air system (see the bottom right corner in Fig. 2.1) that consists of 6 parallel arranged integrated volume flow meters and regulating valves. This system is able to control air volume flows up to 900 Nm³/h. The compressed air was taken from the central compressor station of the FZD, which provides filtered and dry air with a pressure less then 0.7 MPa.

2.2 Pressurised tank technology

Experiments with steam and water at power plant typical boundary conditions implicate to deal with two main constraints: the high pressure and the high temperature. Usually these harsh boundary conditions limit the measuring techniques strongly. In order to broaden range of applicable instrumentation, a new operation technique was developed at FZD, which makes it possible to perform high-pressure steam/water experiments under pressure equilibrium.

A pressure tank, that is 6.5 m long, with a diameter of 2.45 m and a volume of ca. 32 m^3, is used (see figure 2.3). It can be pressurised with air for experiments at ambient temperatures or with nitrogen for steam experiments up to 5 MPa. The facility is equipped with a compressor station (Fig. 2.4) and a nitrogen-supply unit (Fig. 2.5). Both systems can deliver a gas flow rate of about 350 Nm³/h up to a pressure of 5.5 MPa. The temperature of the inner tank atmosphere has to be kept below 60 °C for safety reasons by using an effective thermal insulation of the test rig itself and an air circulation system, which is connected to a gas/air cooler. In order to protect all the present electronic devices inside the tank, the temperature had to be below 50 °C.

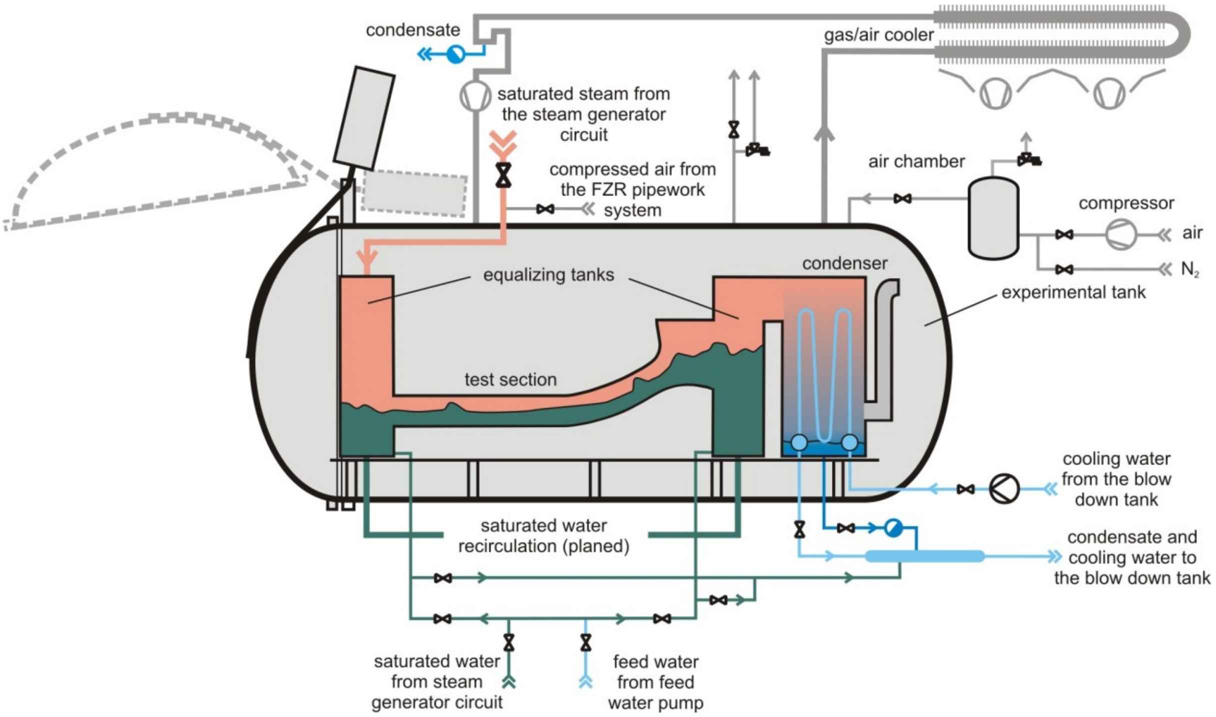

Fig. 2.3 Pressurised tank for tests under pressure equilibrium

For steam/water experiments, a special heat exchanger condenses the exhaust steam from the test section directly in the pressure chamber. Detailed information about the construction and dimensions of the built-in condenser and the tank can be found in the engineering drawings in appendix III.

Figure 2.3 schematically shows the entire experimental design inside the pressure tank. The hot leg model is mounted between two equalising tanks. The left serves as a simulator for the reactor pressure vessel and the right tank works as a separator and stands for the steam generator in this test series. The dimensions of these tanks are 1.55 x 0.8 x 0.5 m with a total volume of about 0.6 m³. They are equipped with one rectangular flange each (1.04 x 0.1 m open area) for connection to various kinds of test sections.

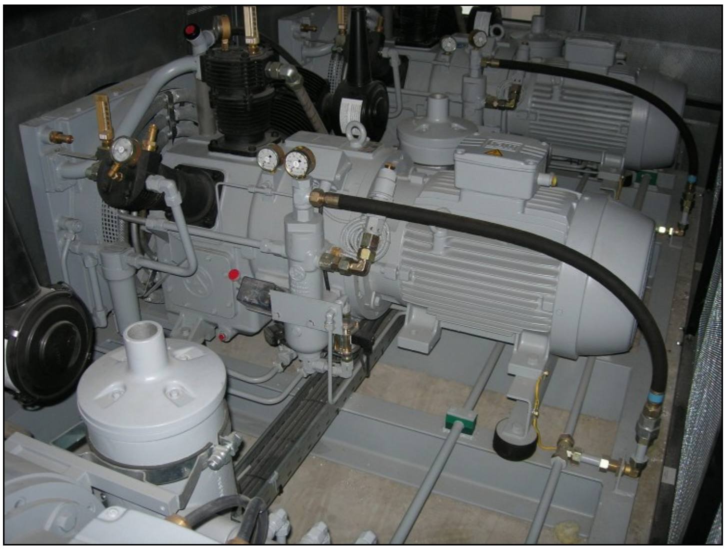

Fig. 2.4 Compressor station consisting of 3 devices

Fig. 2.5 Nitrogen-supply unit

The steam/water mixture enters the separator so that only the steam flows into the condenser and the resulting water is been taken out of the facility. The condenser unit is open to the pressure tank atmosphere and therefore, it is operated with two gases: the steam to condense and a non-condensable gas (air or nitrogen) which fills the pressure chamber. Both gases stratify because of the density difference: the lighter steam is injected from the top and the heavier non-condensable gas stays at the bottom. The stratification layer in the condenser unit allows a self-regulation of the heat exchangers cooling power according to the arriving steam flow rate. In fact, by displacing the stratification layer up and down, the steam uncovers exactly the surface of the vertical heat exchanger tubes needed for its full condensation. In order to allow the free movement of the stratification layer inside the condenser unit while changing the steam flow rate, the cold end of the heat exchanger is permanently connected to the inner atmosphere of the chamber, which guarantees the full pressure equilibrium at all times.

This technology allows the test section to be designed with thin walls and extraordinary shapes, because they do not have to take the pressure stress during high-pressure experiments. Further advantages of the pressure equilibrium technology are:

- the manufacturing of the tests itself is cheaper,
- thin walls make it possible to apply instrumentation, for instance temperature filed measurements via infrared camera observations and
- no expensive licensing procedure is necessary for the test rig itself.

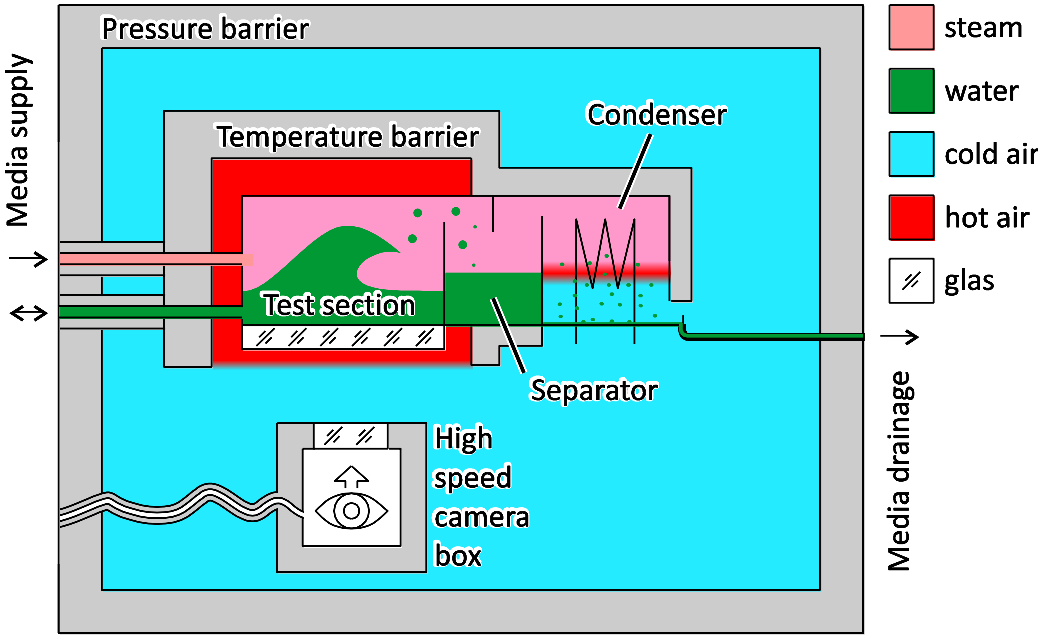

Fig. 2.6 Pressurised Tank Technology in principle

In order to afford the visual observation of macroscopic two-phase flow phenomena at high pressure and high temperature levels, several arrangements have been made (see Fig. 2.6). The basic problem that the camera can not stand the high pressure and temperature cannot simply be solved by the use of windows, because there is no transparent material to separate high pressure and temperature gradients at the large dimensions needed. The basic used principles for solving this problem are the usage of *density stratification* and the *separation of barrier functions* in order to use one small window as a pressure barrier for the camera at low temperatures and another large window for the separation of the hot fluids. The thermal barrier is represented by insulation material (see section 2.3 for details) that is in direct contact with most parts of the hot surfaces. For observed areas, the Insulation is realized as a cap with an open bottom. The transparent temperature barrier is the stratification layer between hot and cold air in this area.

Fig. 2.7 insulated hot leg model test section

In order to assure fast and full access to the test set-up, the pressure tank is equipped with a fast operating full-size port on one side (Fig. 2.3 and 2.7). The test section can be disconnected from the condenser unit and taken out of the vessel by moving it on a rail track. In front of the full-size port, there is a service platform, where parts of the facility can be assembled or maintained. The entire set-up can also be taken off by a traverse and a crane and put to the floor of the experimental hall, from where a second test section can be picked up and inserted into the pressure tank. In this way, the tank can be used for different tests in an effective way.

2.3 Experiences with thermal insulations under overpressure

As mentioned before, the temperature of the tank atmosphere should not exceed 50 °C. Since the saturation temperature at 50 bars is 264 °C, a thermal isolation of the test section is needed in addition to the cooling system.

After assembling of the equalizing tanks and the condenser at the platform it was decided to carry out the first commissioning tests with a straight horizontal channel (Fig. 2.8) with a rectangular cross-section (0.25 x 0.05 m, about 3 m long). This set-up was completely insulated with mineral and glass wool matting. The result of the first test in March 2005 showed that it was impossible to reach the designated parameters. The steam experiment was terminated due to a heat-up of the tank atmosphere above 60 °C at a system pressure of about 0.8 MPa and a temperature inside the test rig of app. 160 °C.

The problem with the thermal insulation was affected by the large difference between the gas densities at about 40 °C inside the pressure tank and maximal 265 °C near the metal walls of the test rig at 5 MPa. This difference of more than 20 kg/m³ forces a strong natural convection even within the fibre packages, made of conventional insulation mats. Furthermore, the dynamic viscosity of air as a nearly ideal gas is approximately independent from the pressure. Due to the increasing density, the kinematic viscosity decreases with growing pressure what additionally reduces the insulation characteristics.

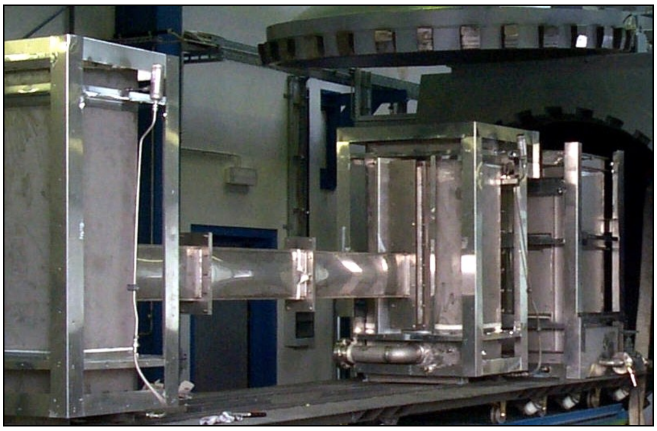

Fig. 2.8 Commissioning test with a straight horizontal channel

It was found that both, insulation capability of the mineral wool and the heat removal capacity of the first configuration of the gas/air cooler were insufficient. This cooler was designed as a system of two finned U-tubes with natural convection on the secondary side. The gas inside the pressure vessel circulated through these U-tubes forced by a pressure-proof electric fan installed in the circulation pipe (see Fig. 2.3). The achieved cooling power was between 0 and 4 kW, heavily depending on the ambient air temperature and air movement. Therefore, the basic cooler was equipped with a radial ventilator forcing the convection cooling on the secondary side. With this improvement, the power increased to approximately 12 kW and the cooling system works more reliable.

Nevertheless, the problems concerning the isolation materials remained. The first try was to compact the mineral wool and to fill identified thermal bridges with additional amounts of insulation material. As a result, a commissioning test was accomplished, where the facility reached nominal parameters. It was not possible though to keep the temperature in the tank below 50 °C. In September 2005, a steam experiment at a pressure of 5 MPa was accompanied by an increasing temperature in the tank up to about 70 °C. This is the limiting value of the safety circuit, which disconnected the tank from the steam supply.

In order to identify an appropriate thermal insulation material for the test section, an autoclave was built and equipped with an electrical heater, which allowed testing samples of different materials under the design conditions of the hot leg tests. The insufficient properties of mineral wool were reproduced. After numerous series of tests with different materials, foam glass was found to be applicable. It showed excellent insulation properties, together with a full stability in air at 5 MPa and about 280 – 300 °C.

Relying on these positive results, at October and November 2005 the preliminary test section was insulated with bricks of foam glass (quality S3) and glued to the surface of the test section with a high temperature silicon resin (Coltogum). Figure 2.9 shows a part of the insulated test rig. At December 2005 in the first hot large-scale test inside the pressure tank, a large part of the foam glass bricks ruptured and disintegrated into debris at a pressure of 2.2 MPa and the corresponding saturation temperature (217 °C) inside the test section. Because this effect was never found in autoclave tests, a chemical analysis of the foam glass was ordered. The results showed that this material contains not only a lot of carbon dioxide, but also a bit of carbon monoxide and hydrogen sulphide which are chemical reactive. Probably, these two gases were generated during the production process of the foam glass from a mixture of glass and coal powder, because the coal mostly contains sulphur. In the same time, the silicon resin used for fixing of the bricks showed no signs of degradation during this experiment.

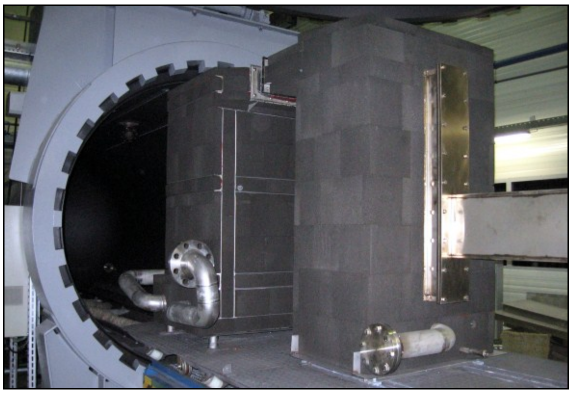

Fig. 2.9 Foam glass insulation

Fig. 2.10 Silicon resin insulation

A continued search for an applicable insulation material led to the discovery that a self-foaming two-component silicon resin (Polysiloxan RTF762 long-chain polymer) is both insulating and stable under the test autoclave conditions. Additionally, the silicon resin foam is easy to handle if components of complicated geometry have to be covered, since the two-component mixture is a high-viscosity liquid that can be casted into surrounding forms. In this way, from March to Mai 2006 the entire preliminary test section together with the built-in condenser and the insulation cap was covered, using about 350 kg of silicon resin (see Fig. 2.10).

The test of this thermal insulation was performed in three steps. In the first step, the test section was heated up to app. 100 °C without pressurising it. This was done to assure that the entire mass of the two-component resin arrived at fully polymerized conditions and residues of organic solvents were eliminated. In the second step, the tank was pressurised up to the maximum pressure of 5.0 MPa without heating-up, to check the behaviour of the insulation foam under pressure conditions.

The third experiment was a hot test with steam supply and a continuous pressure increase. It was planned to reach nominal parameters, both for pressure and temperature of the steam. The insulation properties of the silicon resin foam proved to be excellent until a system pressure of 4.7 MPa. The temperature in the pressure tank remained at 44 °C. Around this stage of the pressurisation and temperature, a sudden increase of the pressure and the temperature inside the tank appeared, which was caused by the onset of a fast oxidation and decomposition process of the silicon resin. The fire lasted for about 4 minutes and led to the nearly complete destruction of the thermal insulation material. The safety valve of the pressure tank was activated at a pressure of about 5.5 MPa and limited the pressure growth to 5.8 MPa. During the blow-off period, the gas flowed through the safety valve and the connecting pipes with a temperature of more than 1300 °C with very high velocities. Thus, the pipe connecting the tank with the valve heated-up to red heat and broke. After that, the discharging gas jet uncovered a part of the buildings roof and led to further destructions on the infrastructural equipment.

A fault analysis of the silicon foam insulation showed that at high temperatures of about 260 °C the long-chain polymer decomposes to short-chain compounds. These substances are combustible at temperatures of about 100 °C in an oxygen atmosphere. During the preliminary small-scale tests inside the autoclave, the concentration of short-chain Polysiloxans never increased the critical level, because inside the autoclave the ratio of insulation material to air (oxygen) was advantageous.

Directly after the fire, the technical surveillance organization TÜV checked the pressure tank, the safety valve, the cooling system and the internals. The result was a list of requirements, which was fulfilled until August 16th 2006. The most important actions were the changing of the safety valve and the connecting pipes with equipment of larger diameter, the repair of the pressure tank and a pressure test of this tank with an inspection pressure of 8.1 MPa. Parallel to these actions the repair works on the infrastructural equipment were finished until October 2006. It included the removal of residua of the silicon foam, the cleaning of the internals of the tank and the cooling system as well as the reconstruction of the roof, the repair of the heating system and the electrical installation. Additionally to the requirements of the technical surveillance organization, FZD installed a high-pressure nitrogen unit (see Fig. 2.5) for inertisation of the tank atmosphere. This gas supplying system allows decreasing the oxygen concentration in the pressure tank under 1 Vol% after pressurisation up to 5 MPa without flushing. This small O_2 concentration securely avoids the accumulation of some combustible mixture in the tank volume.

During the repair and cleaning works on the facility, a series of new thermal insulation materials was checked. To avoid further chemical problems with the insulation material, parallel to the estimation of the thermal conductivity as well as the check of the pressure- and temperature stability in the autoclave, chemical analysis were ordered for the favourite materials.

Fig. 2.11 Thermal insulation with Multitherm and covering with stainless steel sheets

Fig. 2.12 Insulation of a hose with Superwool blanket

The result of this selection process was the identification of two pure inorganic oxidic insulation materials: Multitherm 550 and Superwool 607 blanket. Both are mixtures of about 75% SiO_2 with app. 25% MgO and CaO as well as traces of Na_2O, K_2O and Al_2O_3. The first material (plates 0.5 x 0.5 x 0.03 m) is used for the insulation of plane surfaces like walls of tanks etc. It was installed in 2 layers with a covering of 1 mm stainless steel sheets for prevention of mechanical damage and protection against splash water (see Fig. 2.7 and 2.11). The second one is a more flexible blanket, which is used for insulation of curved surfaces, e.g. pipes or hoses. Figures 2.7 and 2.12 shows a multi-layer insulation of a hose, where each Superwool layer is covered with a 50 µm foil of stainless steel. This method leads to an essential decreasing of the thermal conductivity for Superwool insulation compared to the pure material (see table 2.1).

Table 2.1 Physical and thermal characteristics of used inorganic insulation materials

Property		Multitherm 550	Superwool 607 blanket
Classification temperature		550 °C*	1100 °C*
Density		130 kg/m^3*	128 kg/m^3*
Thermal conductivity	@ 0.1 MPa, 250 °C	0.034 W/(mK)*	0.1 W/(mK)*
	@ 5 MPa, 280 °C	0.08 W/(mK)**	0.06 W/(mK)***
Heat capacity	@ 0.1 MPa, 250 °C	1.1 kJ/(kgK)*	1.05 kJ/(kgK)*

*	all properties were taken from the data sheets of the manufacturer
**	estimated during autoclave tests for a single layer probe
***	estimated during autoclave tests for a multi layer probe with stainless steel foil as convection barrier

The values for the thermal conductivity (λ) at 5 MPa in table 2.1 were estimated during several autoclave tests which were carried out with a combined probe of the insulation material and a plate with this well-known parameter (Teflon, $\lambda_{Tef} = 0.25$ W/(mK)). During these tests, the temperature differences (Δt) over the insulation material and over the Teflon plate were measured. If both material thicknesses (δ) are known and the heat flow density through the probe is assumed as constant, than with equitation (2.1 can be estimated the unknown parameter:

$$\lambda_{insu} = \frac{\lambda_{Tef} \cdot \Delta t_{Tef} \cdot \delta_{insu}}{\delta_{Tef} \cdot \Delta t_{insu}} \tag{2.1}$$

Using this knowledge, the hot leg test rig and the built-in condenser were completely insulated (see Fig. 2.7).

As aforementioned in this chapter, it is necessary for the hot leg tests to ensure an effective thermal insulation and the possibility of optical observation simultaneously. It is clear, that the part of the test section, which needs observation, must not be covered with insulation material. Therefore a cap was used, that surrounded the transparent part of the test section (see also Figs. 2.7 (b) and 2.10). During the steam experiments, the hot gas forms a stable stratification inside this cap that stays under the cap thanks to the density difference between the hot gas around the test section and the cold inventory of the pressure tank. Thus, the insulation cap can only be opened to the bottom, which allows the pressure equalization and a free optical path for observation.

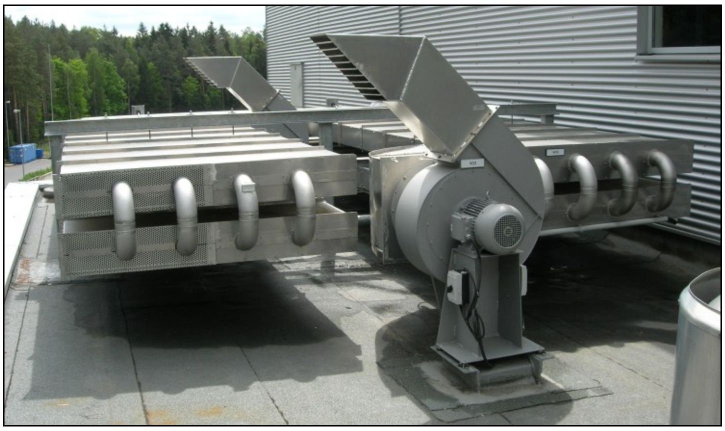

Fig. 2.13 The upgraded over-roof cooling system

With the information about the thermal conductivities and the geometry of the hot leg test, it is possible to estimate the heat losses inside the pressure tank. In order to avoid an incorrect temperature rise in the tank during steam experiments, it was decided to improve the over roof gas/air cooler a second time. Therefore, it was upgraded from 2 to 8 finned U-tubes with effective forced circulation on the secondary side. Figure 2.13 shows the improved heat exchanger with both new electric fans and the 4 stainless steel boxes enclosed the finned U-tubes. During the 5 MPa hot leg tests with steam and saturated water the cooling system of the pressure tank achieved a heat removal capacity in the range of 32 to 38 KW at ambient temperatures between 18 and -1 °C respectively.

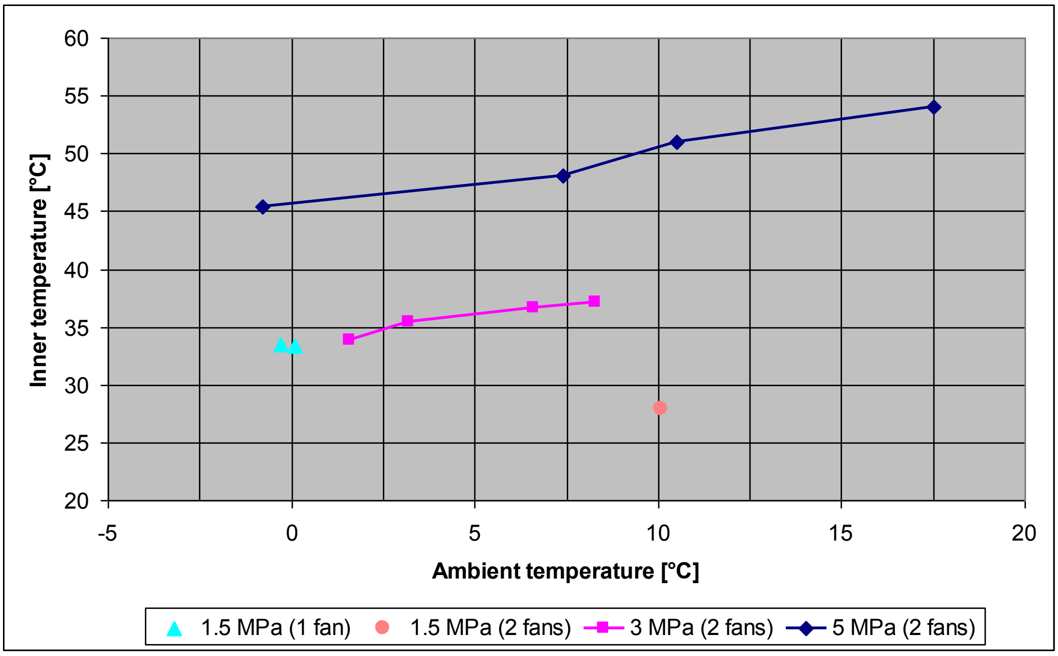

Fig. 2.14 Dependency of the temperature inside the pressure vessel to the ambient temperature

The dependency of the temperature inside the pressure vessel to the ambient temperature in accordance of the pressure (saturation temperature) in the test rig is shown in Figure 2.14. For the pressures 1.5 (at 10 °C), 3 and 5 MPa both fans on the secondary side of the cooler were activated. For 1.5 MPa and 0 °C ambient temperature, one fan was sufficient to remove the heat. For this reason, the temperature inside the vessel for 1.5 (at 0 °C) and 3 MPa was nearly equal. Figure 2.14 proves the operability of the pressure vessel system for pressures up to 5 MPa and the corresponding saturation temperature of 265 °C in the test rig up to ambient temperatures of 20 °C.

2.4 The hot leg test-section

The test section of the hot leg model is schematically shown in Figure 2.15. The main components are the test section itself, the reactor pressure vessel (RPV) simulator located at the lower end of the horizontal channel and the steam generator (SG) separator connected to the SG inlet chamber. The test section reproduces the hot leg of a pressurised water reactor of the German *Konvoi* type at a scale of 1:3. In order to provide optimal observation possibilities, the test section is not composed of pipes like in the original power plant; it is a 50 mm wide channel representing a cut through the vertical mid-plane of the hot leg and of the steam generator inlet-chamber. Consequently, the horizontal part is also composed of a horizontal rectangular channel, a bend that connects it to an upward inclined and expended channel, and a quarter of a circle representing the steam generator inlet-chamber. The horizontal part of test section is 2120 mm long and has a rectangular cross section of 50 x 250 mm². The SG and RPV simulators are identical vessels with 800 x 500 x 1550 mm³ (D x W x H) cubic shape.

Detailed information about the construction and dimensions of the test section can be found in the engineering drawings in the appendix III.

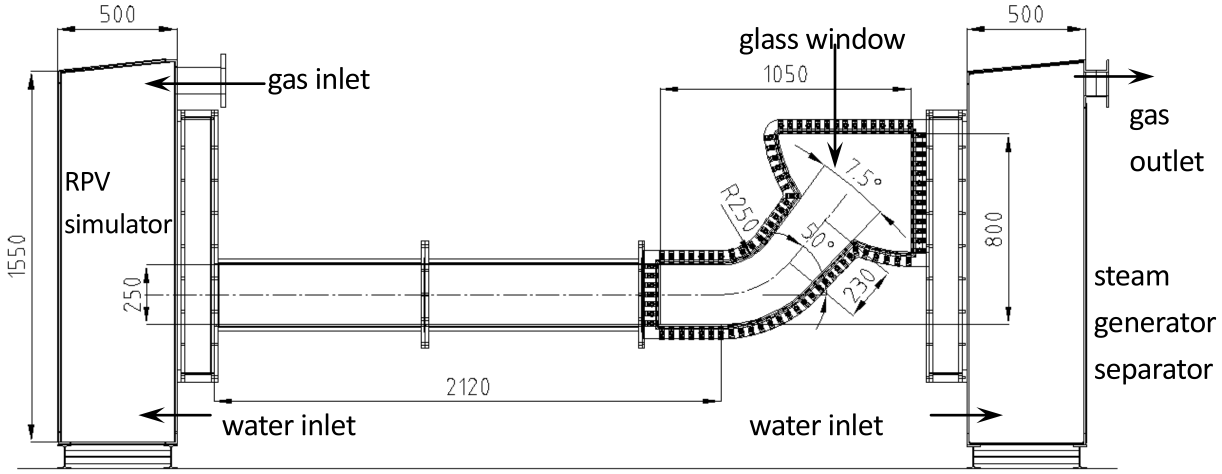

Fig. 2.15 Schematic view of the hot leg model test section (dimension in mm)

2.5 Observation systems

2.5.1 LED illumination

For the cold air/water experiments, a LED illumination system was chosen. LED array modules of the type *seelectorLUX A150* manufactured by *hema electronic GmbH* were used, which contain 100 ultra bright LEDs each (see detailed technical specifications in the annex). The advantages of this kind of LED illumination are:

- pressure proof design (tested in house);
- low voltage power supply: according to the technical rules, the power line can be transmitted through the wall of the pressure chamber and consequently the LED modules can be operated directly in the pressure chamber;
- high-power illumination;

- high number and well distributed light sources
  (i.e. best preconditions to achieve homogenous illumination).

17 single LED array modules were disposed in front of the tests section (see Fig. 2.16-a or detailed drawing in the annex). Due to ventilation slots designed on the side of the LED modules for their active air-cooling, a space of about 20 mm had to be left free between the modules. In order to achieve a homogeneous background illumination, a diffuser plate was mounted between the LED modules and the test section. For the diffuser, a 5 mm thick glass plate sandblasted on both sides was chosen and was fixed on the steal frame of the test section. The distance between LED modules and diffuser plate was about 0.4 m. The power of the single LED modules was adjusted via output voltage of the power supply units in order to achieve the best possible background uniformity. Moreover, steel sheets were mounted around the transparent part of the test section in order to restrict the illuminated area to the domain of interest.

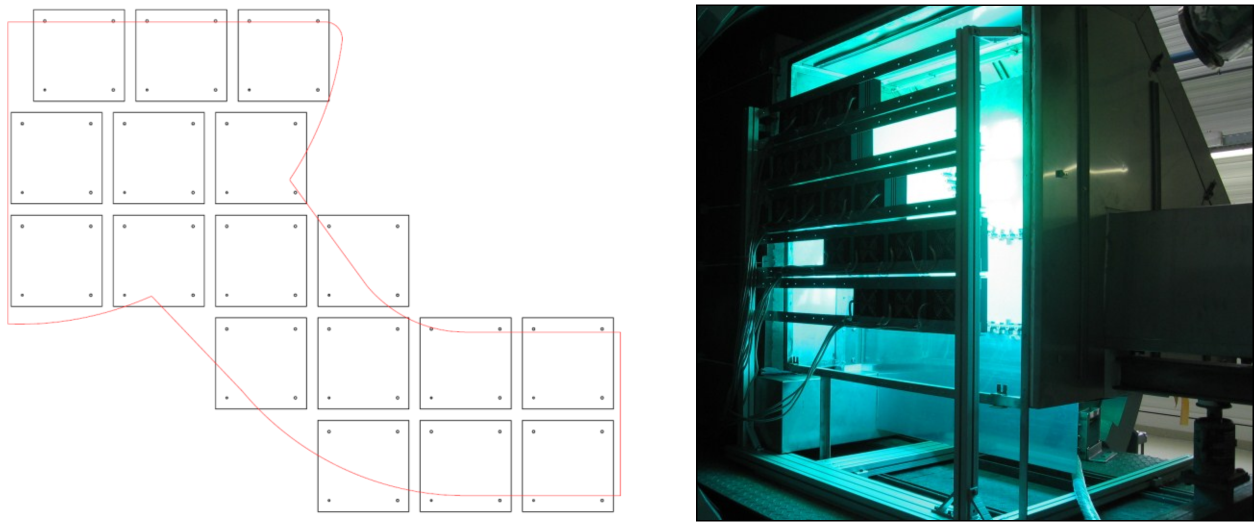

(a) Disposition of the LED modules (black) in front of the diffuser plate (red)

(b) Mounted LED modules and the test section

Fig. 2.16 LED illumination for the air/water experiments

2.5.2 Fibre optics illumination system

Unfortunately, the LED illumination system could not also be used for the steam/water experiments, because the operation of the LED modules is limited to low surrounding temperatures. Therefore, a second illumination system was build up for the hot steam/water experiments. Apart from the LED illumination, no other powerful light source was found which could be installed in the pressure chamber. Therefore, the light had to be generated outside of the pressure chamber, transmitted through a sight glass and guided via fibre optics to the test section.

A high power gas-discharge lamp (see Fig. 2.17-a) was used as light source (*TSO* type *HMI 1200*, further details in the annex). The power supply of the gas-discharge lamp was chosen with a flicker free mode for high-speed observations up to 1.0 kHz (type *ARRI 575/1200 EB* by *Arnold & Richter Cine Technik GmbH & Co*). The beam of parallel light enters the pressure chamber through one of its sight glasses DN125. Afterwards, the light beam is collected with a lens in order to penetrate transversely the inlet of a dedicated fibre optics bundle. Special glass fibres withstanding high temperature gradients were chosen, because the other end of the fibre optics is exposed to the high temperatures below the insulation cap. The fibre optics bundle was designed with one inlet and multiple outlets (see Fig. 2.17-c) in order to distribute the light uniformly over the complete observed area and consequently to achieve a homogeneous illumination of the test section background (see chapter 5.1 for the resulting pictures). Therefore, each of the seven outlets of the fibre optics bundle was connected to wide angle optical systems (Fig. 2.17-d) disposed behind the diffuser plate (Fig. 2.17-b). Contrary to the LED modules, the wide-angle modules were not placed perpendicularly to the diffuser plate, but were directed to the high-speed camera. Therefore, the ideal room position of the modules has been determined in 3D in function of their angle to the optical axis of the camera. Accordingly, a target was arranged and placed on the test section in order to position the modules correctly with a laser beam.

(a) high power gas-discharge lamp

(b) lightening system mounted on the test section

(c) fibre optics bundle

(d) single wide angle module

Fig. 2.17 lightening system for steam/water experiments

2.5.3 Special measures needed for the camera observation

One additional issue was to enable the observation of the hot steam/water flow without inducing substantial heat losses. For this, the high density difference between the hot and cold gas observed at high pressures was used as an advantage. In fact, the transparent part of the test section was surrounded with an insulation cap (see Fig. 2.7) where the hot gas forms a stable stratification and stays like in a hot-air balloon. In order to reduce the heat losses to a minimum, the insulation cap is only open to the bottom. This allows placing the camera outside of the hot regions, but implies to place the camera vertically.

Consequently, the observation of the test section from the side is only possible over a 45° inclined mirror placed under the insulation cap (see Fig. 2.19), which deflects the light from the test section to the camera. Due to this configuration, the mirror must be designed to withstand temperatures of up to 264°C at which it could be exposed in this region. Furthermore, a front surface mirror should be used in order to avoid ghost images. Therefore, a glass plate was coated to mirror with a 100 nm aluminium layer, which was protected from oxidation by an additional 100 nm SiO_2 coat. Such samples were successfully tested in an air atmosphere at 50 bar and 280°C, which is more than the expected conditions under the insulation cap.

For the evaluation of the position and dimensions of the mirror, a 3D CAD model of the test apparatus was arranged. The optical path was simulated from the camera objective over the mirror to the main outer edges of the transparent part of the test section (Fig. 2.19). From the model, the minimum mirror dimensions were estimated to about 745 x 760 mm (L x H). For an easier adjustment as well as for safety margins, a mirror with a reflecting surface of 825 x 825 mm (i.e. after subtraction of the borders for the support) was planned.

After the manufacturing and assembling of the components, the position of the high-speed camera and mirror were adjusted in order to best visualise the test section. The result is shown in a test picture of the high-speed video camera (see Fig. 2.18). The border between mirror and its support frame was marked in red in the figure, which shows that the adjustment latitude in the vertical direction is limited. However, this test proves that the 3D CAD model was a good way for the global design the optical system and in particular for the dimensioning of the mirror.

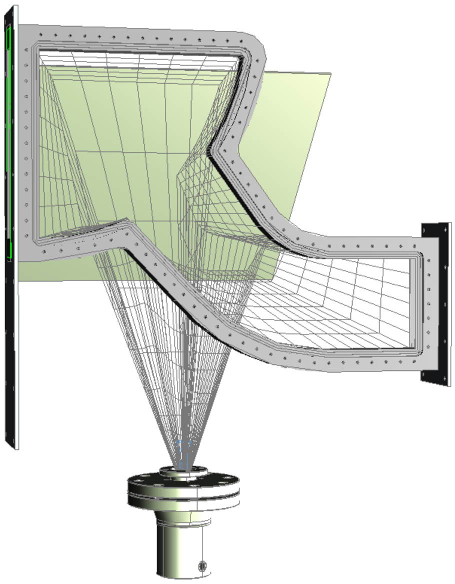

Fig. 2.18 3D Model of the optical path for observation of the test section over the mirror

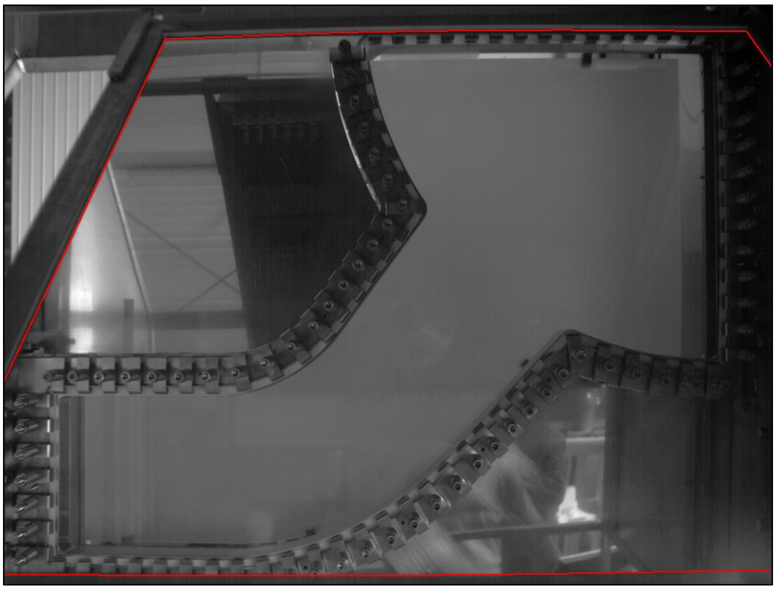

Fig. 2.19 Picture of the test section after positioning of the high-speed camera and adjustment of the mirror (inner frame edge in red)

3 Measurement technique

The TOPFLOW facility is equipped with various kinds of measurements. During the design- and installation period of the facility, one important requirement was high accuracy not only of the transducers but also of the entire measurement system. Most transducers scale a measured physical value (pressure, temperature, concentration etc.) and transform it into a standard output signal. Beside the transducers, most measurement channels include an electronic device that converts this standard analogue output signal into digital information. The electronic devices are combined in groups and connected to Interbus modules, which manage the communication among each other and with an OPC server. This server stores the measured data and delivers information for visualization and controlling. Additionally, it serves as a data source for the operational data logging system, which operates at a frequency of 1 Hz.

3.1 Measured data

During operation of the facility, the accuracy of the measurement channels may degrade. For this reason, it is necessary to calibrate the transducers and check the measurement channels. Because the TOPFLOW facility includes hundreds of measurements, it is very time-consuming to calibrate the entire equipment. Therefore, the gauging is focused on the most important devices (see Fig. 3.1 and Tab. 3.1) which participate in the planned test series. The air/water- and steam/water experiments with the hot leg test section were carried out from Mai 23rd to October 30th 2007 and between December 14th 2007 and Mai 06th 2008 respectively.

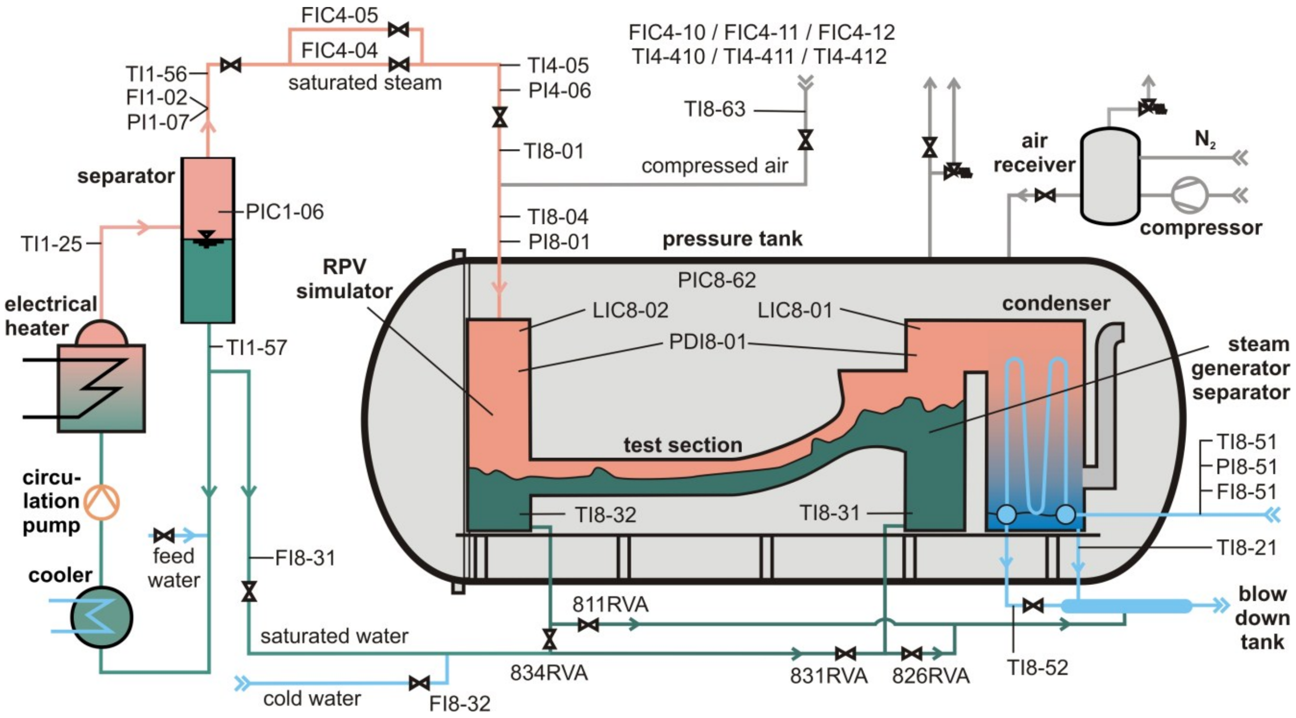

Fig. 3.1 Schematic view of the operational instrumentation for the hot leg tests

Table 3.1 Overview over available measurement data

code	Physical size	range
FI1-02.1	Steam mass flow rate out of TOPFLOW separator	0.27 – 2.7 kg/s
FIC4-04	Steam mass flow rate next to regulation valves	0.25 – 2.7 kg/s
FIC4-05	Steam mass flow rate next to regulation valves	0.027 – 0.26 kg/s
FIC4-10	air mass flow rate next to regulation valves	0 – 1000 Nm³/h
FIC4-11	air mass flow rate next to regulation valves	0 – 500 Nm³/h
FIC4-12	air mass flow rate next to regulation valves	0 – 50 Nm³/h
FI8-31	water mass flow rate of saturated water	0 – 1 kg/s
FI8-32	water mass flow rate of cool feed water	0 – 1 kg/s
LIC8-01	water level (pressure difference) of SG-separator	0 – 20 kPa
LIC8-02	water level (pressure difference) of RPV-simulator	0 – 20 kPa
PIC1-06	Pressure in TOPFLOW separator	0 – 10000 kPa
PI8-01	Pressure in main steam line	100 – 5500 kPa
PIC8-62	Pressure in pressure tank	100 – 5500 kPa
PDI8-01	Pressure difference between separators	0 – 50 kPa
TI1-57	Temperature of saturated water	50 – 300 °C
TI4-410	Temperature of air line 10	35 – 50 °C
TI4-411	temperature of air line 11	35 – 50 °C
TI4-412	temperature of air line 12	35 – 50 °C
TISA+8-02	Temperature of the air in the condenser opening	50 – 100 °C
TI8-04	Temperature of the steam in main steam line	50 – 300 °C
TI8-31	temperature	50 – 300 °C
TI8-32	temperature	50 – 300 °C

3.2 Calibration

Calibration information relating these tests is listed in table 3.2. It includes flow- (FI or FIC), level- (LIC), pressure- (PI or PIC), pressure difference- (PDI) and temperature (TI) measurements. The first numeral of the identifier in the left column of table 3.2 characterizes the corresponding circuit of the facility and the last number is an item count.

Table 3.2 Calibration data for measurements used during the hot leg test

Measurement	Measuring range	Calibration range	Maximal deviation	Calibration date	Comments
FI1-02.1 (*)	0.27 – 2.7 kg/s	0.27 – 2.7 kg/s	1.01 %	21.05.02	ISA nozzle, Rosemount 3095MV
FI1-02.2 (*)	0.27 – 2.7 kg/s	0.27 – 2.7 kg/s	1.09 %		
FIC4-04.1 (*)	0.25 – 2.7 kg/s	0.24 – 2.7 kg/s	0.69 %	21.05.02	ISA nozzle, Rosemount 3095MV
FIC4-04.2 (*)	0.25 – 2.7 kg/s	0.24 – 2.7 kg/s	1.30 %		
FIC4-05.1 (*)	0.013 – 0.25 kg/s	0.013 – 0.26 kg/s	0.90 %	21.05.02	ISA nozzle, Rosemount 3095MV
FIC4-05.2 (*)	0.013 – 0.25 kg/s	0.013 – 0.26 kg/s	1.26 %		
FI8-31	0 – 1 kg/s	0.4 – 4 kg/s	0.42 %	24.01.07	VORTEX 8800CF
FI8-32	0 – 1 kg/s	0.4 – 4 kg/s	0.42 %	24.01.07	VORTEX 8800CF
FIC4-10	500 – 1000 nm^3/h	400 – 950 nm^3/h	0.64 %	02.10.06	Bronkhorst IN-Flow (see section 3.3)
FIC4-11	50 – 500 nm^3/h	50 – 450 nm^3/h	0.07 %	04.10.06	Bronkhorst IN-Flow
FIC4-12	5 – 50 nm^3/h	5 – 50 nm^3/h	0.11 %	15.09.06	Bronkhorst EL-Flow
LIC8-01	0 – 20 kPa	0 – 20 kPa	0.92 %	21.05.07	Rosemount 3051C
LIC8-02	0 – 20 kPa	0 – 20 kPa	0.58 %	21.05.07	Rosemount 3051C
PIC1-06	0 – 10000 kPa	0 – 10000 kPa	0.13 %	22.10.07	Rosemount 3051C
PI8-01	1 – 5400 kPa	1 – 5400 kPa	0.06 %	15.01.07	Rosemount 3051C
PIC8-62	1 – 5400 kPa	1 – 5400 kPa	0.04 %	18.01.07	Rosemount 3051C
PDI8-01	0 – 50 kPa	0 – 50 kPa	0.85 %	11.01.07	Rosemount 3051C
TI1-57	-270 – 1200 °C	50 – 300 °C	0.6 K	13.11.06	TE Type K Ø 1.5 mm
TI4-410	-270 – 1200 °C	35 – 50 °C	< 0.1 K	16.11.06	TE Type K Ø 1.5 mm
TI4-411	-270 – 1200 °C	35 – 50 °C	< 0.1 K	16.11.06	TE Type K Ø 1.5 mm
TI4-412	-270 – 1200 °C	35 – 50 °C	0.1 K	16.11.06	TE Type K Ø 1.5 mm
TISA+8-02	-270 – 1200 °C	50 – 100 °C	0.8 K	30.11.06	TE Type K Ø 1.5 mm
TI8-04	-270 – 1200 °C	50 – 300 °C	1.0 K	30.11.06	TE Type K Ø 1.5 mm
TI8-31	-270 – 1200 °C	50 – 300 °C	0.7 K	05.12.06	TE Type K Ø 1.5 mm
TI8-32	-270 – 1200 °C	50 – 300 °C	0.9 K	08.11.06	TE Type K Ø 1.5 mm

(*): The transducers are different for low absolute pressure (.1) and for high pressure (.2). The Maximal deviation was calculated from the calibration according to DIN EN ISO 5167-1 (2003).

The manufacturer prefabricated the steam mass flow meters FI1-02 as well as both controllers FIC4-04 and FIC4-05. The associated transducers (Rosemount 3095MV) determine the density and the kinematic viscosity of the fluid (steam) using his pressure and temperature. Afterwards, they calculate the mass flow by means of these physical properties, the pressure difference (measured over an ISA nozzle) and geometrical parameters of the nozzle and the tube. During the erection of the TOPFLOW facility, the nozzle measurement devices were welded on the pipes. Therefore, it is impossible to calibrate these measurements with maintainable effort. Thus, the data of the factory calibration are included in table 4.1, because the manufacturer guaranteed 5 years of operation with a measurement error less than 1% for the mass flow.

The parallel-arranged controllers FIC4-10 to FIC4-12 supply the volumetric airflow for the air/water tests. The thermal mass flow meters and controllers for gases delivered by the company Bronkhorst are used for air experiments. Behind a turbulence filter, a defined partial flow is separated from the total airflow and lead through the measurement cell. Insight this cell, a heater element is installed between two measurement resistors, which are arranged successively in flow direction. The measured temperature difference is a function of the air mass flow. In order to convert the air mass- into volumetric flow, the density is used again. It is calculated from the air pressure and temperature before heating. For the FIC4-11 and 12, a magnetic regulated valve, directly arranged after the measurement cell, does the control of the volumetric airflow. A downstream pneumatic operated control valve observes the very large airflows of the FIC4-10. In order to avoid leakages from the parallel switched air controllers into the test section, each line is equipped with a three-way valve that blocks the inactive controllers and drains possible leakages into the TOPFLOW building (comp. Figs. 2.1 and 3.1). The polynomial calibration of the volumetric airflow controllers were performed at the manufacturer Bronkhorst. The results are presented in table 3.2 and in the appendix.

FI8-31 and FI8-32 are vortex meters for the liquid mass flow of the saturated- and the cold feed water respectively injected into the equalizing tanks (Fig. 3.1). The measurement principle is based on the Kármán vortex street. The fluid streams through the sensor including a special tube with a well-defined obstacle. Behind this barrier, the flow forms counter rotating vortexes whose separation frequency is detected with a piezoelectric element. The volume flow is calculated from this frequency and geometrical parameters of the sensor using the Strouhal number. The sensor processes the mass flow from this, using the density of the fluid. Beside some advantages, these sensors have two relevant limits: On one hand, the measurement error increases for very low flow velocities (less then 5 % of the measurement range). This fact was incorporated in the test matrix, which contains only liquid mass flows above 0.3 kg/s. On the other hand, the definition of mass flows for saturated water may be disturbed, if some steam bubbles occur in the flow due to pressure loss, e.g. over valves or bends. This effect came out at the hot tests and was considered by special filtering and reconstruction algorithms during the data evaluation (see chapter 5.2).

Especially during steam/water tests, it is important to know the pipe routing between the mass flow meters and the test section. Furthermore, this information may be useful for CFD calculations. For this reason, appendix III contains some isometric drawings of relevant pipes in the facility. In addition, they show the entrance- and end section before and after the mass flow meters that should be more then 10 or 5 times the diameter of the tube.

The pressure-, pressure difference- and level measurements were calibrated with an UNOMAT MCX/1910 being checked annually (inspection date: June the 20th 2006 and September the 14th 2007) at the company Druck Nederland B.V. The gauging of the FZD transducers was done by adjusting several pressure values within the calibration range, while the points are checked both at the increment and at decrement of the pressure. Afterwards the output signals were compared with the set values and, if necessary, the transducer was adjusted accordingly. The calculation of the level of the pressure difference over the equalizing tanks is down in consideration of the liquid and gas density inside the tanks in accordance to equitation 3.1:

$$L_L = \frac{L_{imp} \cdot \left(\rho_{imp} - \rho_G\right) - \frac{\Delta p}{g}}{\rho_L - \rho_G} \tag{3.1}$$

Thereby: L_L is the level in the equalizing tank in m; L_{imp} is the difference between the measuring points on the tank in m; ρ is the density of: L – liquid, G - gas and imp – fluid in the impulse pipe in kg/m³; Δp is the pressure difference over the tank in Pa and g is the gravitational acceleration.

The thermocouples were examined with a metal block calibrator (Jupiter 650SN). For the comparison of the temperature indications, a platinum resistance thermometer was used. Both available reference devices were controlled on October the 10th 2006 by the company Klasmeier Kalibrier- und Messtechnik GmbH. In case of deviations from the set values, it is possible to compensate these deviations at the electronic digital/analogue converters. The maximum deviation within the calibration range after the compensation is shown in table 3.2.

Technical parameters of the measurements, detailed results of the gauging and calibration protocols of the reference devices are included in the appendix.

3.3 Correction of the air flow meter FIC4-10

Unfortunately, after all the measurement series have been completed, an error in the implementation of the air flow meter FIC4-10 into the test facility was noticed. As a consequence, the raw flow rates recorded by the digital data acquisition system of TOPFLOW with this flow meter (highest measuring range) are wrong. This concerns only the air/water CCFL experiments. In order to correct the measured flow rates afterwards, a calibration curve was recorded with a certified rotameter. This flow meter was mounted in series with the FIC4-10, its outlet being open to the atmosphere. The scale of the rotameter (Yokogawa type RAMC08) was established for air at reference conditions of 20.0°C and 1.0 bar. Because the measuring conditions were slightly different, the determined values were corrected according to the indications given by the manufacturer as follows:

$$\dot{V}_{N,corr} = \dot{V}_{N,read} \cdot \sqrt{\frac{T_{ref}}{T_{real}} \cdot \frac{p_{real}}{p_{ref}}} \tag{3.2}$$

The actual temperature T_{real} was measured with a thermocouple placed in the flow section at the outlet of the rotameter. The actual pressure p_{real} was obtained from the value at the sea level p_0 published hourly in the internet (site: www.wetter.com / meteorological station of Dresden-Klotzsche), which was converted to the altitude z of FZD using the barometric formula:

$$p_{real} = p_0 \cdot \exp\left(-\frac{g \cdot M_{air}}{R \cdot T_{real}} \cdot z_{FZD}\right) \tag{3.3}$$

with M_{air} the molar mass of air ($28.96 \cdot 10^{-3}$ kg/mol) and R the universal gas constant ($8.314\ J \cdot mol^{-1} \cdot K^{-1}$). For the calculations, an altitude of 290 m was taken for the FZD.

After conversion of the volume flow rates (indicated by the meters in norm cubic meter per hour) to mass flow rates, the obtained calibration points could be modelled with a quadratic function as shown in Figure 3.2. The resulting correction function, leading to a sufficient correlation coefficient, is:

$$\dot{m}_{corr} = -2.43822773 \cdot \dot{m}_{raw}^{\ 2} + 2.38124793 \cdot \dot{m}_{raw} - 0.117486184 \tag{3.4}$$

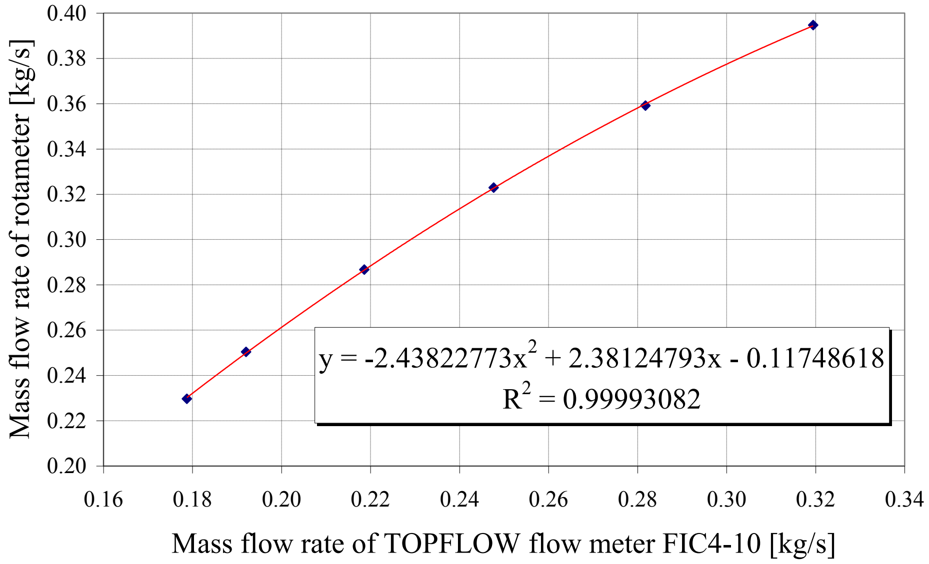

Figure 3.2: Calibration curve of the air flow meter FIC4-10

3.4 Synchronisation

While recording the flow conditions in the hot leg model, two independent systems were running – the controlling and measurement system of the TOPFLOW facility and the high-speed camera. They were synchronised with a very robust method similar to the clapperboard in film productions. In the central instrumentation, system of TOPFLOW a signal was implemented which was manually switched on from the control room, actuating a LED inside the pressure vessel to glow. This signal was recorded in the measuring plots and the LED was in the visual range of the high-speed camera. Assumed that the clock speeds of both systems were similar, the signals could have been adjusted.

The accuracy of simultaneity depends on the delay of the bus system and the signal processing components. The time shift is smaller than ± 1 s. This is good enough for the relatively continuous variation of the measured data we expected and see.

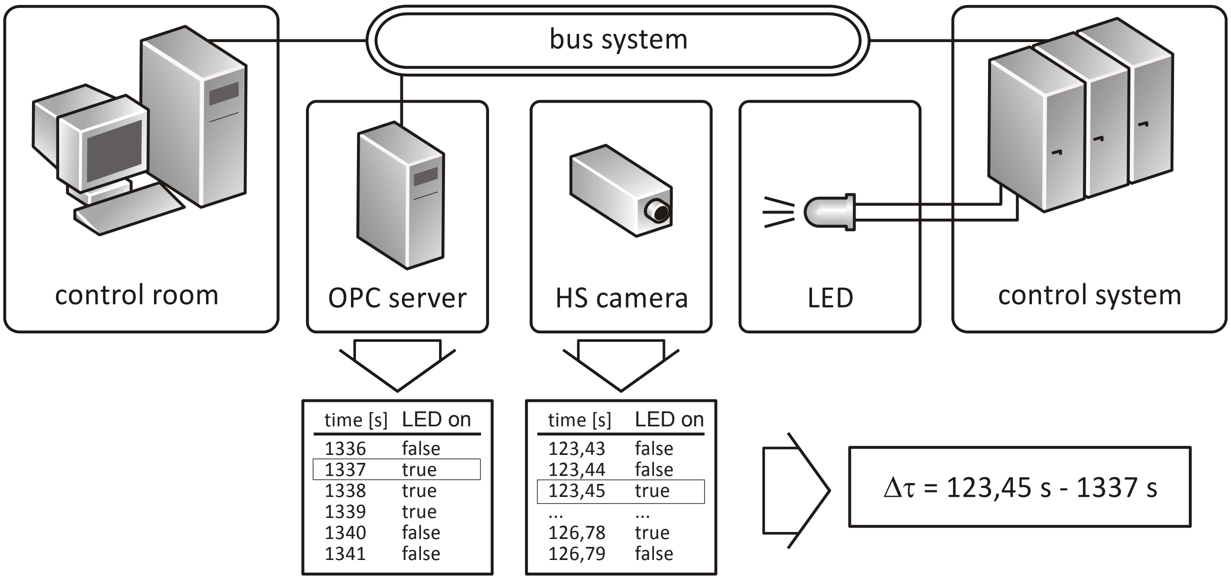

time [s]	LED on
1336	false
1337	true
1338	true
1339	true
1340	false
1341	false

time [s]	LED on
123,43	false
123,44	false
123,45	true
...	...
126,78	true
126,79	false

$\Delta\tau = 123{,}45\ \text{s} - 1337\ \text{s}$

Fig. 3.3: synchronisation method of the different measurement systems

4 Experimental procedure

4.1 Preparation procedure

Before the measurements could have been started, some preliminary operations were necessary: First, the impulse pipes were flushed and the function of the pressure- and differential pressure transducers were checked especially to get accurate level information of the equalizing tanks. Furthermore, the equipment for optical observation and the measurement data-acquisition system were examined.

For the two different gas/liquid combinations, air/water and steam/water different start up procedures have been developed. For the air/water tests, the two separation tanks and the hot leg test section were filled with deionised water until the liquid levels defined in the test conditions. The water mass flow to one of the test section (see Fig. 2.3) was supplied by the feed water pump (see Fig. 2.1) and controlled by the valves 831RVA or 834RVA and the frequency converter of this pump. The air/water tests were carried out under overpressure in the pressure vessel so that the drain water from the equalizing tanks could flow via 811RVA or 826RVA to the blow down tank. The gas was supplied by the compressed air system (comp. figure 2.1).

For the steam/water experiments, the entire hot leg test section with both separators was filled with deionised water up to the lower level of the connecting pipe between the steam generator separator and the condenser at a pressure of about 0.3 MPa in the vessel. Additionally the electrical heater circuit was put into operation with air pressure of 0.6 MPa without heating power and was connected via the flow meter FI8-31 (see Fig. 3.1) to the RDB simulator of the hot leg test (834RVA open). After opening the drainpipe of the steam generator separator (826RVA), a part of the medium of the electrical heater circuit flowed through the test section to the blow down tank, because of the pressure difference. Thereby the levels in the separation tanks were controlled by LIC8-01 and LIC8-02 (comp. Fig. 3.1). Then the electrical heater was powered up on the minimal level. With the cooling system of the electrical heater circuit, the increasing of the temperature inside the hot leg test was limited to 50 K/h to minimise the temperature stress of the thick glass windows. In this way, the test-section was heated up to app. 150°C, with simultaneous increasing of the pressure in the pressure tank up to ca. 0.5 MPa.

After that the level in the equalizing tanks was been decreased, the cooling system in the condenser was activated and steam was fed into the RPV simulator carefully. Then pressure and temperature in the electrical heater circuit and inside the pressure tank were increased slowly up to the planned working conditions inside the pressure tank with an offset of about 0.5 MPa in the electrical heater circuit. After reaching the necessary conditions inside the hot-leg test section, the flow-direction and the mass flow of the saturated water was set according to the experimental requirements. Afterwards, the steam mass flow rate was increased up to the matrix conditions. See the operation guide of the TOPFLOW-facility (Beyer, 2004) for comparison.

4.2 Type of Experiments

There have been four different types of experiments, depending on the global water flow direction in the Hot Leg Model. This has been varied with the position of the water inlet and outlet valves. Since the gas, flow was always directed form the RPV simulator to the SG separator, the test types are named according to the flow relation.

4.2.1 Co-current Flow Experiments

This experiment was started with a low water level in the SG-separator and a level at the bottom of the horizontal channel in the RPV-simulator (see red line in figure 4.1). With the open valve 834RVA, water was injected into the RPV-simulator and flows co-currently to the gas in the Hot Leg Model. The water level in the RPV simulator increased until the horizontal channel was filled enough to initiate some transport process of the water towards the SG separator.

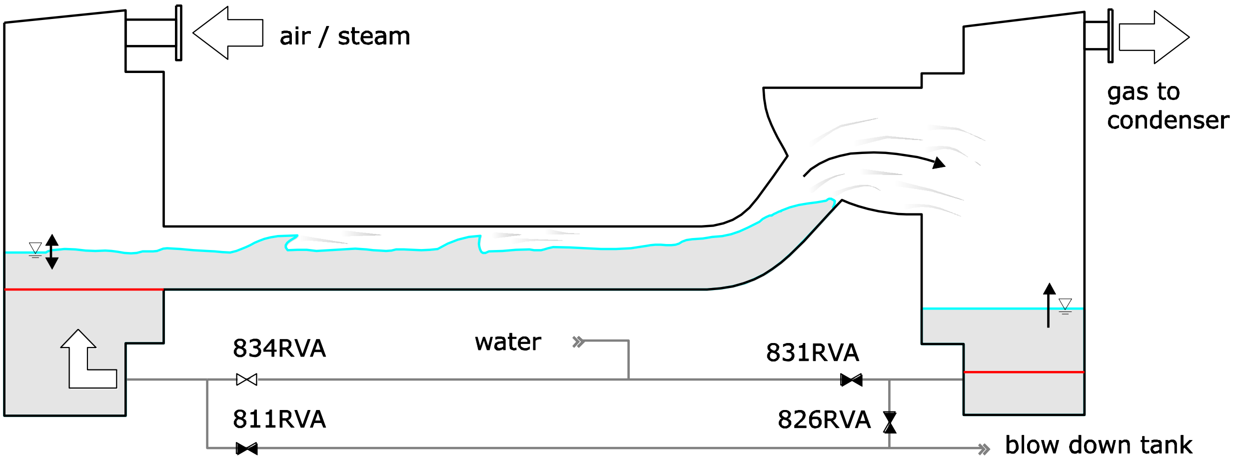

Fig. 4.1: Schematic illustration of the co current flow experiments
red line: start up condition, blue line: an exemplary flow condition

4.2.2 Counter-current Flow Experiments

This test started with a high water level in the SG-separator and a RVP level near the horizontal channel. It was initiated by opening the valve 831RVA and an overflow of water from the SG-separator to the RPV. A rising water level in the RPV leads to certain transport processes of water to the SG-separator, where the water level is rising then. (see figure 4.2)

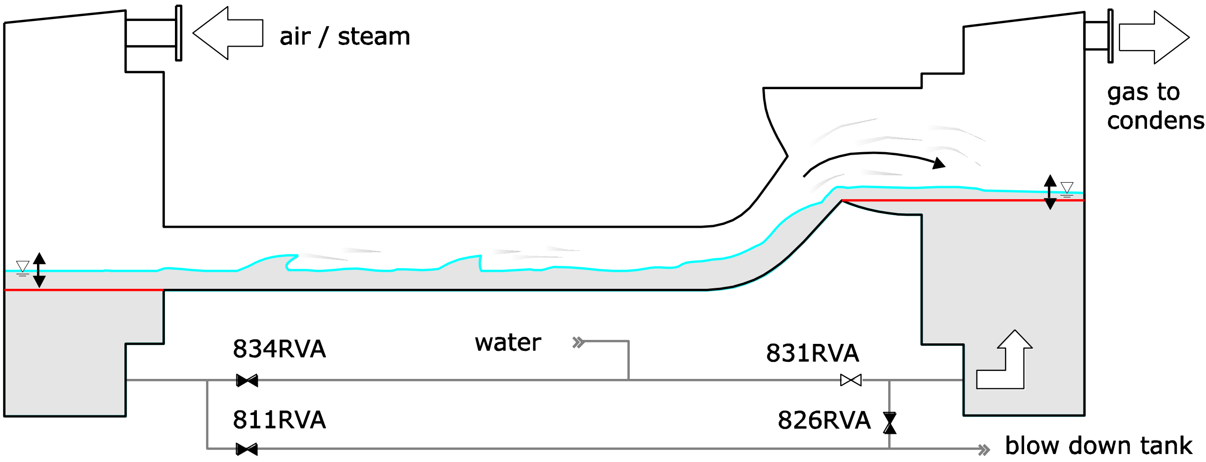

Fig. 4.2: Schematic illustration of the counter-current flow experiments
red line: start up condition, blue line: an exemplary flow condition

4.2.3 Counter Current Flow Limitation Experiments

As well as in counter-current Flow Experiments, the water flows downward to the RPV simulator first. However, with a water level in the RPV simulator below the horizontal cannel, all the water from the SG separator that passed the hot leg was able to run away to the bottom. Because of the closed valves 811RVA and 834RVA, the discharge flow rate was measurable by means of the RPV water level.

The water inflow rate was always kept constant and the gas flow rate was varied during the experiments. Thus, there were two different types of CCFL experiments: flooding experiments with rising gas flow rate and deflooding experiments with falling gas flow rate. (see figure 4.3)

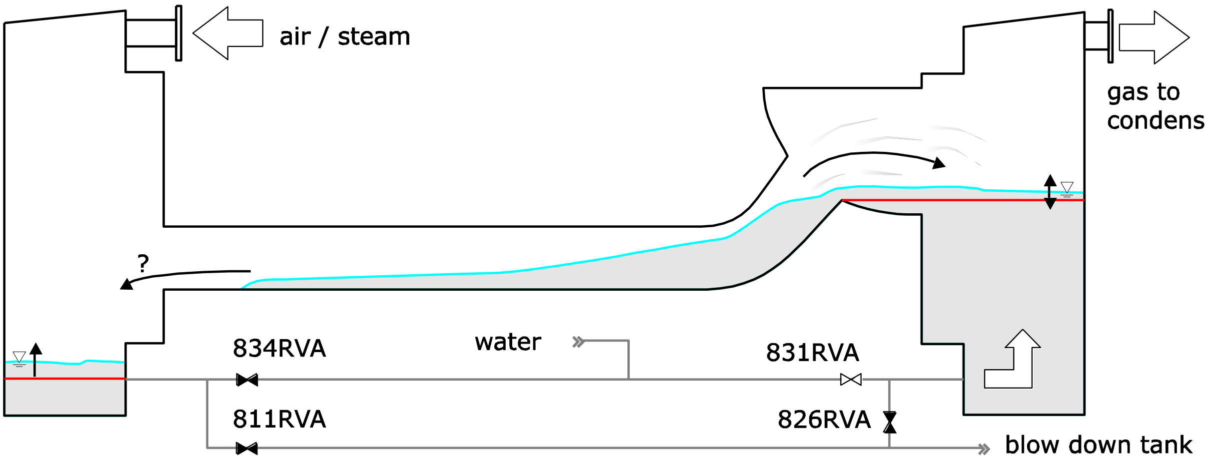

Fig. 4.3: Schematic illustration of the counter current flow limitation experiments (CCFL)
red line: start up condition, blue line: an exemplary flow condition

4.2.4 Experiments without feeding of water

When water levels in both separators are high enough for discharge and all inlet and outlet valves are closed, we refer to the experiment as experiment without feeding of water. At this condition, there is another free parameter in the test matrix. The flow phenomena also depend on the total water volume in the Model or rather the sum of both water levels. The gas flowing through the hot leg model entrains the stagnant water.

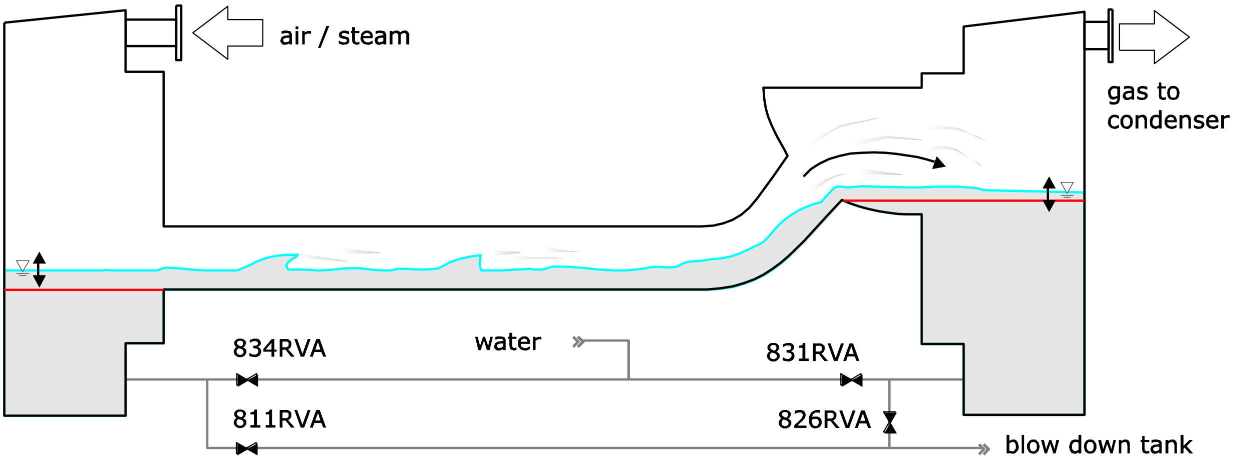

Fig. 4.4: Schematic illustration of the experiments without water injection
red line: start up condition, blue line: an exemplary flow condition

4.3 Boundaries and arrangement of the test matrix

The boundaries of the test matrix are limited on one hand by the installed hardware and on the other hand by physical or practical reasons. After the definition of the range of the possible, the test matrix can be arranged in details, defining the final number of runs. However, the test matrix defines only theoretical goal values that cannot be perfectly achieved during the experiment. Consequently, for exact information, please always refer to the measured values. The detailed test matrices as well as a complete overview of the boundary conditions of each experiment are presented in the appendix I.

First, the pressure levels of the experiments were chosen. The maximum value is limited by the design pressure of the pressure chamber of 50 bars. However, this is only possible for steam/water experiments, because the air supply system of the TOPFLOW test facility only works at pressures up to about 7 bar. Furthermore, for a safe operation of the test facility, and especially in order to treat the large glass windows with care, the occurrence of condensation shocks should be avoided. Therefore, it was chosen not to perform steam/water experiments at low-pressure levels, where condensation shocks may also occur with water subcooling of just a few Kelvin. The lowest pressure level for the steam/water tests was set to 15 bars, in order to enable comparisons with the results obtained at the UPTF test facility, where this value was often chosen for experiments (e.g. CCFL experiments in Test n° 11). Moreover, the temperature of the steam/water experiments always corresponds to saturation conditions, whereas the air/water tests were performed at room temperature.

The hot leg experiments were performed at the following pressure and temperature conditions:

- air/water: 3.0 bar / 14-29°C
- steam/water: 15.0 bar / 198°C, 30.0 bar / 234°C, 50.0 bar / 264°C

With the available hardware of the facility, the fluid flow rates can be varied in the following range:

- water:	0.3 … 1.0 kg/s	(flow meters FI8-31 and FI8-32)
- air:	0.002 … 0.340 kg/s	(flow meters FIC4-10 … 12)
- steam:	0.016 … 1.40 kg/s	(flow meter FIC4-04/FIC4-05 and max. heating power)

Since the possible range of water flow rates is narrow, this was completely used (0.3 to 1.0 kg/s) for all types of experiments with water injection. Some CCFL experiments were performed at lower water flow rates. In this case, the flow rate can only be estimated over the water level increase in the separators, because the flow meter gives no indication.

The test matrix of the counter-current flow limitation experiments (flooding and deflooding) was arranged in function of the gaseous medium, of the pressure level and of the inlet water flow rate. Because the gas flow rate was varied during these experiments, this parameter is not included in the test matrix. However, the number and duration of the gas flow rate plateaux as well as the difference between 2 plateaux were changed from run to run. Due to the limited measuring time of the high-speed video camera (internal buffer of 8 GB) as well as the water accumulation in the SG separator, a compromise had to be found in each run between the number and duration of the plateaux of gas flow rate. Furthermore, due to the difficulties to operate the test facility during the highly transient steam/water experiments, perfect steps could not be realised. In fact, the steam flow rate could not be stabilised perfectly after each increase, because it should be nearly doubled within a few minutes. In order to check the validity of the Wallis parameter, 2 air/water experimental series were performed at 1.5 and 3.0 bar. Furthermore, one single flooding experiment was performed with steam and water at the pressure of 2.36 bar. One similar experiment had been performed during the insulation commissioning tests at the same pressure, but with a straight horizontal channel with the same cross-section as the hot leg model (without high-speed camera observation). The two tests could be compared in order to show the influence of the test-section geometry on the flooding characteristics.

For all types of quasi-stationary experiments (all apart from the CCFL experiments), the test matrix was built in order to be able to match different parameters: points with equal mass flow rate $\dot{m}_i$, equal superficial velocity j_i and equal Wallis parameter J^*_i were chosen. This allows checking the possible similarities involving these parameters at different pressures. The relation between the parameters and the mass flow rate are:

$$\mathrm{j_i} = \frac{\dot{\mathrm{m}}_\mathrm{i}}{\rho_\mathrm{i} \cdot \mathrm{A}} \tag{4.1}$$

$$\mathrm{J^*{}_i} = \mathrm{j_i} \cdot \sqrt{\frac{1}{\mathrm{g} \cdot \mathrm{H}} \cdot \frac{\rho_\mathrm{i}}{\rho_\mathrm{L} - \rho_\mathrm{G}}} = \frac{\dot{\mathrm{m}}_\mathrm{i} / \mathrm{A}}{\sqrt{\mathrm{g} \cdot \mathrm{H} \cdot \rho_\mathrm{i} \cdot (\rho_\mathrm{L} - \rho_\mathrm{G})}} \tag{4.2}$$

Because of the variation of the fluid densities, the three parameters evolve differently with the pressure and temperature conditions, as shown in Table 4.1. As an example, a reference steam/water experiment at 15.0 bar and a steam mass flow rate of 0.150 kg/s is chosen. This corresponds to a superficial velocity in the horizontal part of the test section of 1.58 m/s and a Wallis parameter of 0.095. In order to obtain the same Wallis parameter at 50.0 bar, 0.256 kg/s of steam is necessary. The same gas superficial velocity is achieved at 0.501 kg/s of steam. This important difference in the mass flow rates was used for the arrangement of the test matrix: as shown in Table 4.2 and Figure 4.5, the intermediate points were chosen near the equivalent parameter values (e.g. 0.250 instead of 0.256 kg/s for the point with equivalent Wallis parameter of the example).

Furthermore, although the variation of the density with the pressure and temperature is not so significant for the water than for the gas, its influence is not negligible. In fact, for a mass flow rate of 0.900 kg/s at 15.0 bar, the same Wallis parameter and liquid superficial velocity are obtained at 50.0 bar with 0.798 and 0.807 kg/s, respectively (c.f. Table 4.1). Therefore, the water flow rate has to be chosen according to the same equivalent parameter as for the steam flow rate. This was originally intended but, unfortunately, after the conduction of the experimental series a systematic error in the measurement of the water flow rate during the steam/water experiments was identified. In fact, the measuring device FI8-31 was calibrated for a pressure of 62.0 bar and 260°C. For an application at other conditions the following correction function is necessary:

$$\dot{m}_{L,corr} = \dot{m}_{L,FI8-31} \cdot \frac{\rho_{L(p,T)}}{\rho_{L(62bar,260^\circ C)}} \tag{4.3}$$

Because this compensation of the density variations was not known at the moment of the arrangement of the test matrix, the real water flow rate deviates from the intended one. The most important deviations are obtained for the experiments at 15 bar and reach up to about 10% (e.g. 0.993 instead of 0.900 kg/s). However, in all data presented in this report as well as in the database, only the corrected water flow rate appears.

Furthermore, some single co-current and counter-current flow experiments were performed with air and water at the pressure level of 5.0 bar. These runs were conducted for comparison purposes with pre-test CFD calculations and are not included in the test matrices. After first experimental air/water tests in the hot leg model it was chosen to perform the main experimental series at 3 bar because this allows to cover a wider range of superficial velocities.

Table 4.1: Equivalences for the steam and water mass flow rates between 15 and 50 bar for the reference experiments with 0.300 and 0.900 kg/s of water as well as 0.075, 0.150 and 0.250 kg/s of steam at 15 bar

	Reference conditions			**Same Wallis parameter *J****		**Same superficial velocity *j***	
Pressure:	**15.0 bar**			**30.0 bar**	**50.0 bar**	**30.0 bar**	**50.0 bar**
Fluid [-]	**m [kg/s]**	**J* [-]**	**j [m/s]**	**m [kg/s]**	**m [kg/s]**	**m [kg/s]**	**m [kg/s]**
Steam	0.075	0.0474	0.790	0.102	0.128	0.148	0.250
Steam	0.150	0.0949	1.58	0.204	0.256	0.296	0.501
Steam	0.250	0.158	2.63	0.341	0.427	0.494	0.835
Water	0.300	0.0178	0.0277	0.283	0.266	0.285	0.269
Water	0.900	0.0533	0.0831	0.849	0.798	0.854	0.807

Table 4.2: Equivalences between the experimental points of the test matrix

15 bar experiments		**Equivalent 3 bar experiments**		**Equivalent 30 bar experiments**	**Equivalent 50 bar experiments**
Steam mass flow rate	**Equivalent parameter**	**Air flow rate**		**Steam mass flow rate**	**Steam mass flow rate**
[g/s]	**[-]**	**[Nm^3/h]**	**[g/s]**	**[g/s]**	**[g/s]**
35	mass flow rate	100	35.9	-	-
	Wallis parameter	60	21.5	-	-
75	mass flow rate	200	71.8	75	75
	Wallis parameter	-	-	100	130
	superficial velocity	100	35.9	150	250
150	mass flow rate	400	143.6	150	150
	Wallis parameter	300	107.7	200	250
	superficial velocity	200	71.8	320	500
250	mass flow rate	-	-	250	250
	Wallis parameter	-	-	320	430
	superficial velocity	300	107.7	500	835

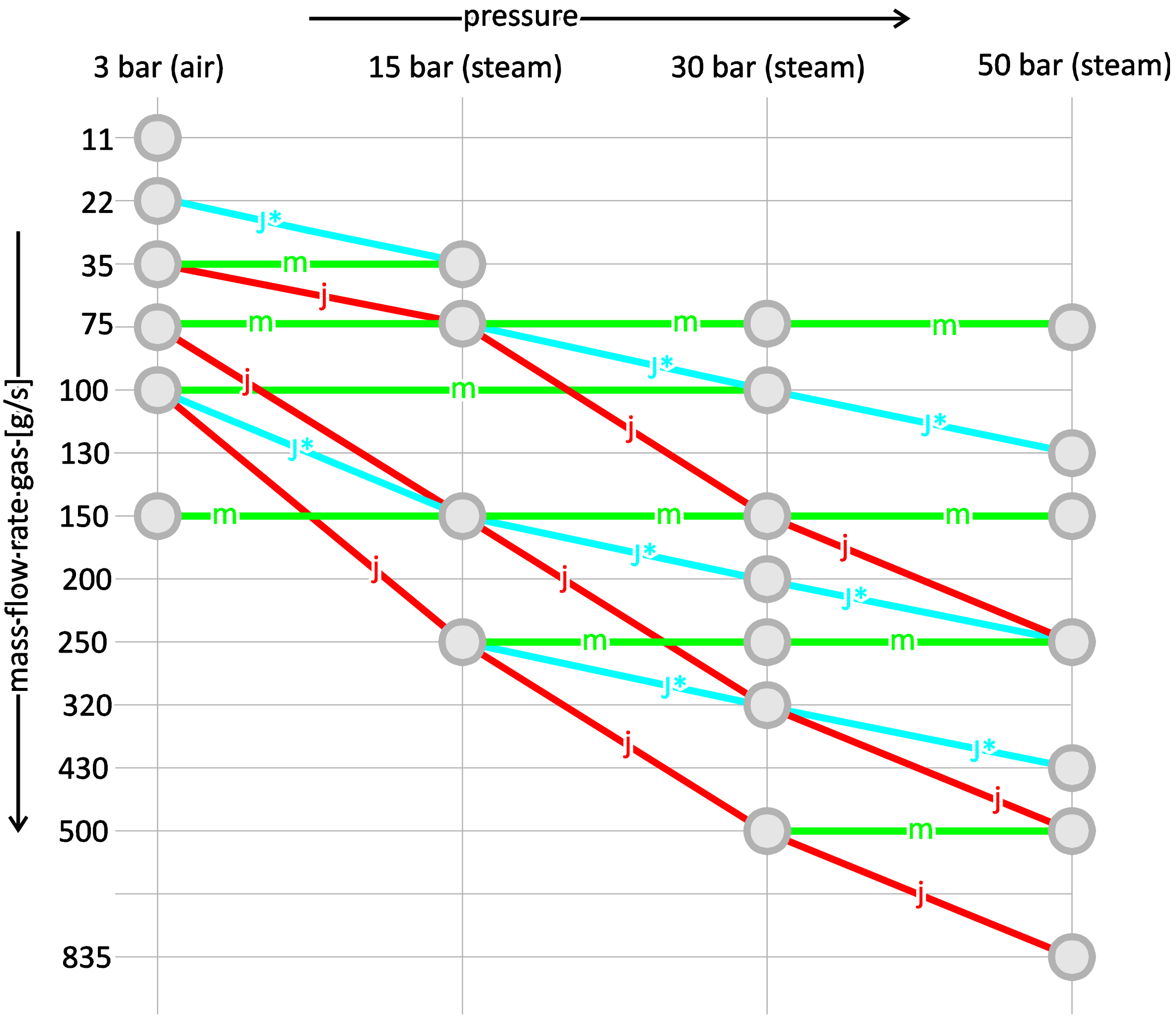

Fig. 4.5: Scheme of the steam test matrix

5 Available Data

5.1 Data access

The raw results of the measurement system is stored in an excel file called “allResults.xls” with the following layout. Shown in figure 5.1, there is a table sheet for each experiment with the name according to the list in appendix I.. The layout of each table is shown in figure 5.2. The first and the second row contain the name, description and the unit of each column, followed by 100 to 1000 rows of data, depending on the duration of the experiment. The first column always contains the timestamp with a typical increment of 1 s. The other rows hold different data for each experiment type, because there are different measurement instruments installed for different cases. For example, the shown experiment in the screenshots is has the name “14-01”. It is a steam/water co-current flow experiment with a steam mass flow rate of 35 g/s and a pressure of 15 bars in the pressure chamber. The gas flow is measured with the instrument FIC4-05, because it is designed for measuring steam flow and has the right sensitivity for this mass flow rate. In conclusion, the other flow meters are deactivated by closing the assigned valves. Consequently, their data is not shown (see Tab. 3.2 and the calibration protocols in the appendix for the ranges).

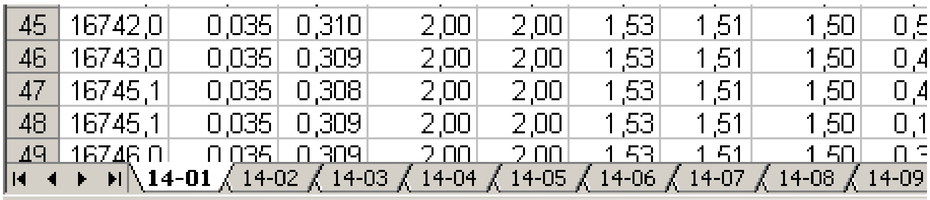

45	16742,0	0,035	0,310	2,00	2,00	1,53	1,51	1,50	0,5
46	16743,0	0,035	0,309	2,00	2,00	1,53	1,51	1,50	0,4
47	16745,1	0,035	0,308	2,00	2,00	1,53	1,51	1,50	0,4
48	16745,1	0,035	0,309	2,00	2,00	1,53	1,51	1,50	0,1
49	16746,0	0,035	0,309	2,00	2,00	1,53	1,51	1,50	0,

Fig. 5.1: Screenshot of the Excel file for the data access; experiments are stored in sheets

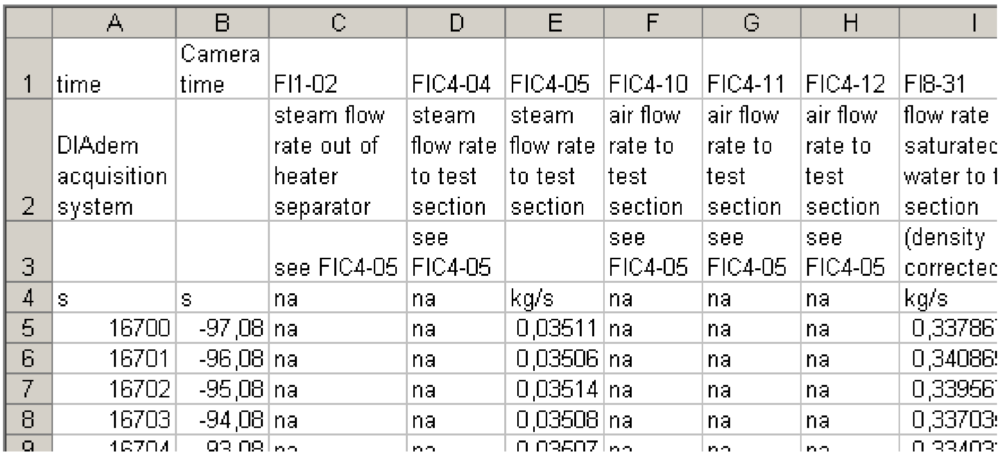

	A	B	C	D	E	F	G	H	I
1	time	Camera time	FI1-02	FIC4-04	FIC4-05	FIC4-10	FIC4-11	FIC4-12	FI8-31
2	DIAdem acquisition system		steam flow rate out of heater separator	steam flow rate to test section	steam flow rate to test section	air flow rate to test section	air flow rate to test section	air flow rate to test section	flow rate saturate water to section
3			see FIC4-05	see FIC4-05		see FIC4-05	see FIC4-05	see FIC4-05	(density correcte
4	s	s	na	na	kg/s	na	na	na	kg/s
5	16700	-97,08	na	na	0,03511	na	na	na	0,3378
6	16701	-96,08	na	na	0,03506	na	na	na	0,3408
7	16702	-95,08	na	na	0,03514	na	na	na	0,3395
8	16703	-94,08	na	na	0,03508	na	na	na	0,3370
9	16704	93,08	na	na	0,03507	na	na	na	0,3340

Fig. 5.2: Excel screenshot: organization in row and columns

One special column is the synchronisation (see chapter 3.3 for details), which is headed “Start2”. It has no unit, because it is a Boolean signal. In most rows, it contains a zero. In the moment, of symbolisation, it holds an ascending number followed by some rows filled with ones, which stand for the switched on LED.

Additional to the raw measured data, excel files are available with pre-processed data. They contain the measured RPV water level probability distribution (more precisely the frequency count) used in Chapter 6.1.2 (see figure 5.3) and the CCFL flooding data for Chapter 6.4.2 (see figure 5.4).

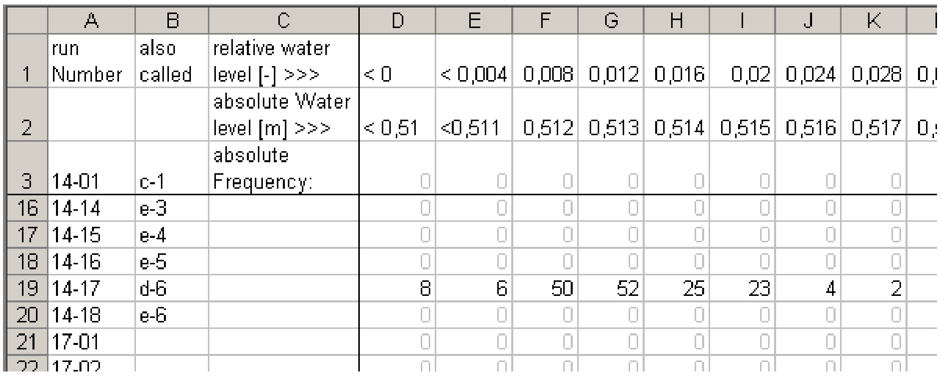

	A	B	C	D	E	F	G	H	I	J	K
1	run Number	also called	relative water level [-] >>>	< 0	< 0,004	0,008	0,012	0,016	0,02	0,024	0,028
2			absolute Water level [m] >>>	< 0,51	<0,511	0,512	0,513	0,514	0,515	0,516	0,517
3	14-01	c-1	absolute Frequency:	0	0	0	0	0	0	0	0
16	14-14	e-3		0	0	0	0	0	0	0	0
17	14-15	e-4		0	0	0	0	0	0	0	0
18	14-16	e-5		0	0	0	0	0	0	0	0
19	14-17	d-6		8	6	50	52	25	23	4	2
20	14-18	e-6		0	0	0	0	0	0	0	0
21	17-01			0	0	0	0	0	0	0	0
22	17-02			0	0	0	0	0	0	0	0

Fig. 5.3: Excel screenshot: water level absolute frequency

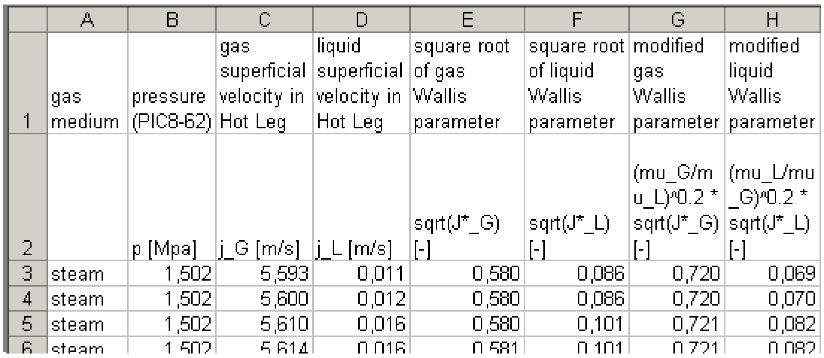

	A	B	C	D	E	F	G	H
1	gas medium	pressure (PIC8-62)	gas superficial velocity in Hot Leg	liquid superficial velocity in Hot Leg	square root of gas Wallis parameter	square root of liquid Wallis parameter	modified gas Wallis parameter	modified liquid Wallis parameter
2		p [Mpa]	j_G [m/s]	j_L [m/s]	sqrt(J*_G) [-]	sqrt(J*_L) [-]	(mu_G/mu_L)^0.2 * sqrt(J*_G) [-]	(mu_L/mu_G)^0.2 * sqrt(J*_L) [-]
3	steam	1,502	5,593	0,011	0,580	0,086	0,720	0,069
4	steam	1,502	5,600	0,012	0,580	0,086	0,720	0,070
5	steam	1,502	5,610	0,016	0,580	0,101	0,721	0,082
6	steam	1,502	5,614	0,016	0,581	0,101	0,721	0,082

Fig. 5.4: Excel screenshot: CCFL flooding data

The high-speed camera pictures are saved as Bitmap files with 8-bit depth and up to 1024 x 768 pixels size. Thus, a pixel equals about 1,2 mm² in the observed field. They are stored in folders, named according to the date of the experiment and the name in the experiment list, were also the shutter frequency can be found (Appendix I). See figure 5.5 for a screenshot of the folder structure. Every experiment-folder contains a RawData-folder, holding all the images and a SinglePics-folder with a picture of the empty test section in order to subtract the background later. This background picture is been generated by calculating the most frequent value of each pixel. Thus, the background picture can be uneven. Nevertheless, this picture can be exchanged between the experiments of each day, because the camera has not been moved during a day.

The quality of the images mainly depends on the intensity and the uniformity of the illumination. The LED lighting system is very smooth and diffuse and the results are easier to process than those with the optical fibre system (see Fig. 5.6 and 5.7). The systems are described in chapter 2.5.

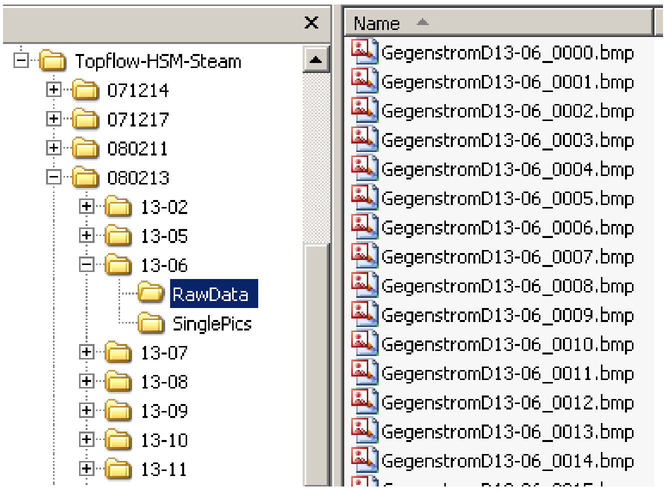

```
Topflow-HSM-Steam
  071214
  071217
  080211
  080213
    13-02
    13-05
    13-06
      RawData
      SinglePics
    13-07
    13-08
    13-09
    13-10
    13-11
```

```
Name
GegenstromD13-06_0000.bmp
GegenstromD13-06_0001.bmp
GegenstromD13-06_0002.bmp
GegenstromD13-06_0003.bmp
GegenstromD13-06_0004.bmp
GegenstromD13-06_0005.bmp
GegenstromD13-06_0006.bmp
GegenstromD13-06_0007.bmp
GegenstromD13-06_0008.bmp
GegenstromD13-06_0009.bmp
GegenstromD13-06_0010.bmp
GegenstromD13-06_0011.bmp
GegenstromD13-06_0012.bmp
GegenstromD13-06_0013.bmp
GegenstromD13-06_0014.bmp
```

Fig. 5.5: Example of the folder structure for the images

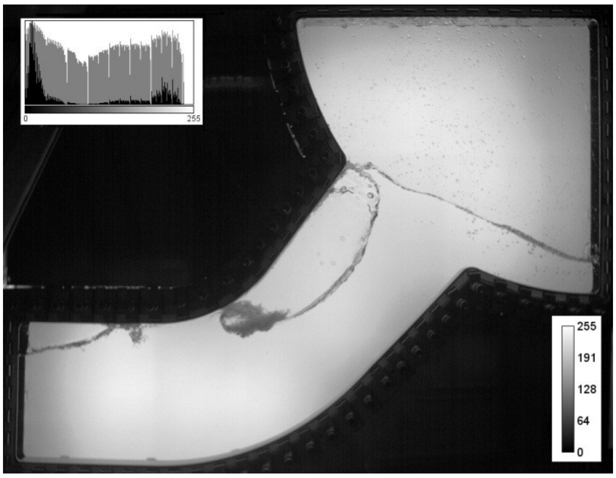

Fig. 5.6: example picture with use of LED lighting system with a linear (black) and a logarithmic (gray) scaled histogram

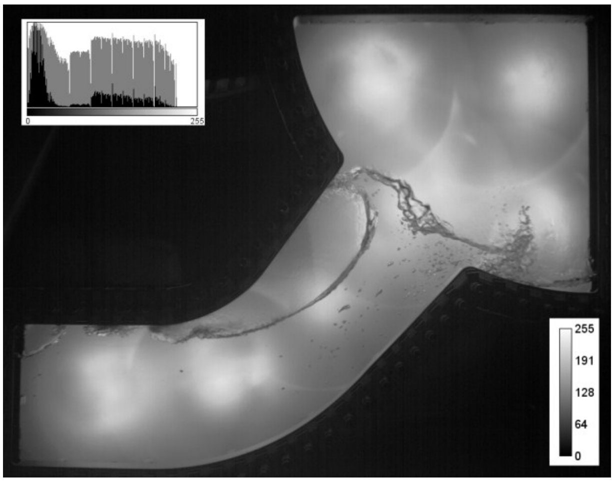

Fig. 5.7: example picture using the optical fibre system with a linear (black) and a logarithmic (gray) scaled histogram

5.2 Adjustment/processing functions

The following values have been calculated from the measured signals.

The *subcooling of the water* has been processed by calculating the saturation temperature at the test section pressure (PI8-01) and subtracting the measured temperatures.

$$t_{RPV/SG,sub} = t_s(p = p_{PC}) - t_{RPV/SG} \tag{5.1}$$

The water levels in both separators have been measured with a pressure difference method. Since the densities of the media vary over the different pressures, they had been calculated. Equation 3.1 is used to get the water level for the measured pressure difference with the height of the pressure impulse pipe $L_{imp} = 1{,}493\,m$ and the gravity acceleration $g = 9{,}81\,m/s^2$. The thermo physical properties have been calculated according to the IAPWS IF97 industry standard using LibIF97 of Zittau/Görlitz University of Applied Sciences - Department of Technical Thermodynamics.

At experiments with saturated water and steam, a formation of gas bubbles in the water line is possible due to pressure drops. This is a problem for the vertex-type water mass flow meter FI8-31. When gas is present at that device, the result is not reliable any more. The results are showing a drop of the mass flow rate at constant boundary conditions (see green line in figure 5.9). For this reason, a procedure described below was applied.

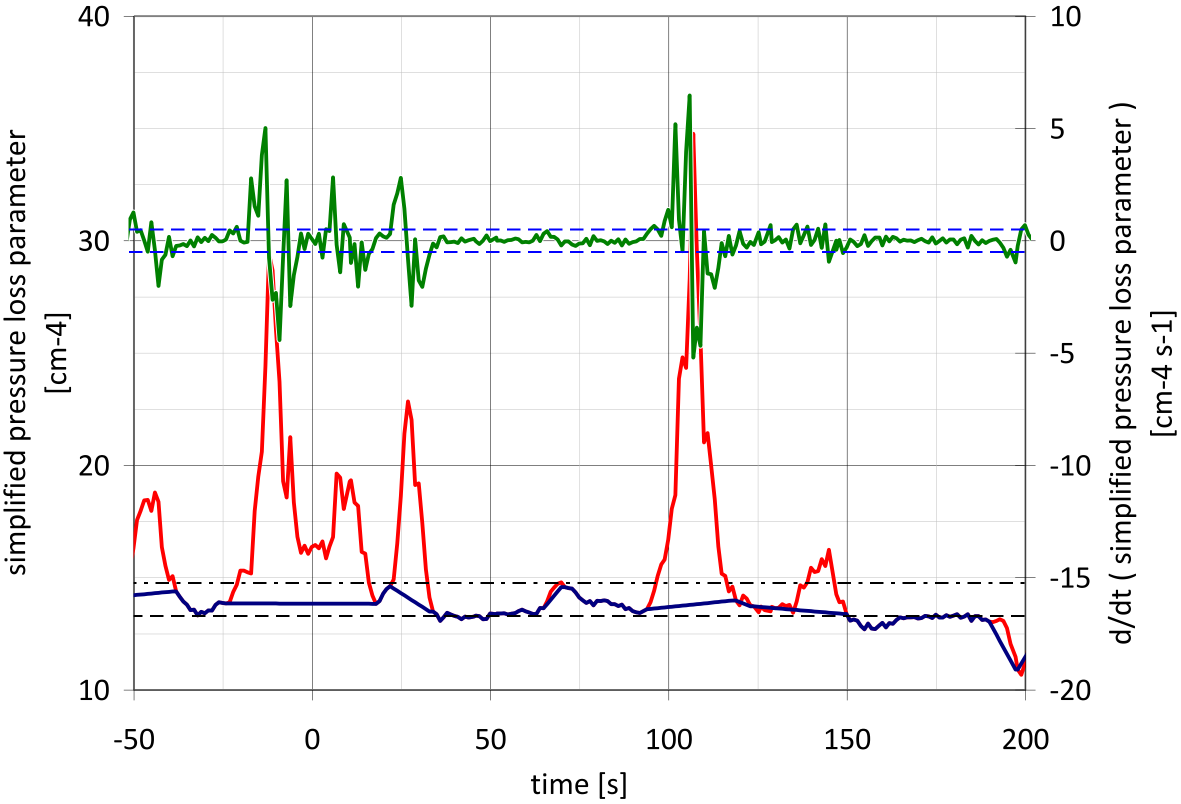

Fig. 5.8: Auxiliary values for the correction of the saturates water mass flow rate:
red: simplified pressure loss parameter, green: time derivative of the parameter;
blue: used interpolation of the pressure loss parameter for correction of mass flow
dashed line: normal pressure loss parameter; dot-dash line: maximal allowed parameter
blue dashed lines: limits of the time derivative

The mass flow through the piping $\dot{m}_W$ depends on the pressure difference between the TOPFLOW-separator p_{sep} and the pressure chamber p_{chamb}, the density of the saturated water ρ, the average flow cross-section A_R and the pressure loss parameter ς_{piping} of the whole piping and the regulation valves. In Order to correct the failed measurement, the pressure loss parameter of the valves and the piping has been monitored all the time. It is defined as follows:

$$\varsigma_{piping} = \frac{2 \cdot (p_{sep} - p_{chamb}) \cdot \rho \cdot A_R^{\;2}}{\dot{m}_W^{\;2}} \tag{5.2}$$

Technically, only the varying values have been used for a simplified pressure loss parameter ς_{simple} according to equation 5.3 with the unit [cm^{-4}].

$$\varsigma_{simple} = \frac{(p_{sep} - p_{chamb}) \cdot \rho}{\dot{m}_W^{\;2}} \tag{5.3}$$

Figure 5.8 shows the evolution of this parameter and its time derivative for the experiment 15-10. Two conditions are defined for characterising the incorrect mass flow value, assuming that the regulating valves have not been moved during experiments. The first is activated, when the absolute pressure loss parameter exceeds a certain limit (dot dash line). This threshold calculated from the 20 %

percentile of the whole run pressure loss parameter, which came out to be a good normal pressure loss parameter (dashed black line). The second condition is the exceeding of 0.25 cm^{-4} s^{-1} of the time-derivative pressure loss parameter (blue dashed lines). When one of the conditions is fulfilled, the pressure loss parameter is replaced by an interpolation between the last and the next valid value (blue line in figure 5.8).

In figure 5.9 the mass flow rate is shown, that results form the backward calculation of the corrected pressure loss parameter with the pressure difference and the density of the water. When the water mass flow is feasible, the corrected value is equal to the measured. Only, when the recorded mass flow drops down without changing the position of any valve or the water density, the correction gives an estimation of the flow condition. In general, it follows the tendency of the pressure difference.

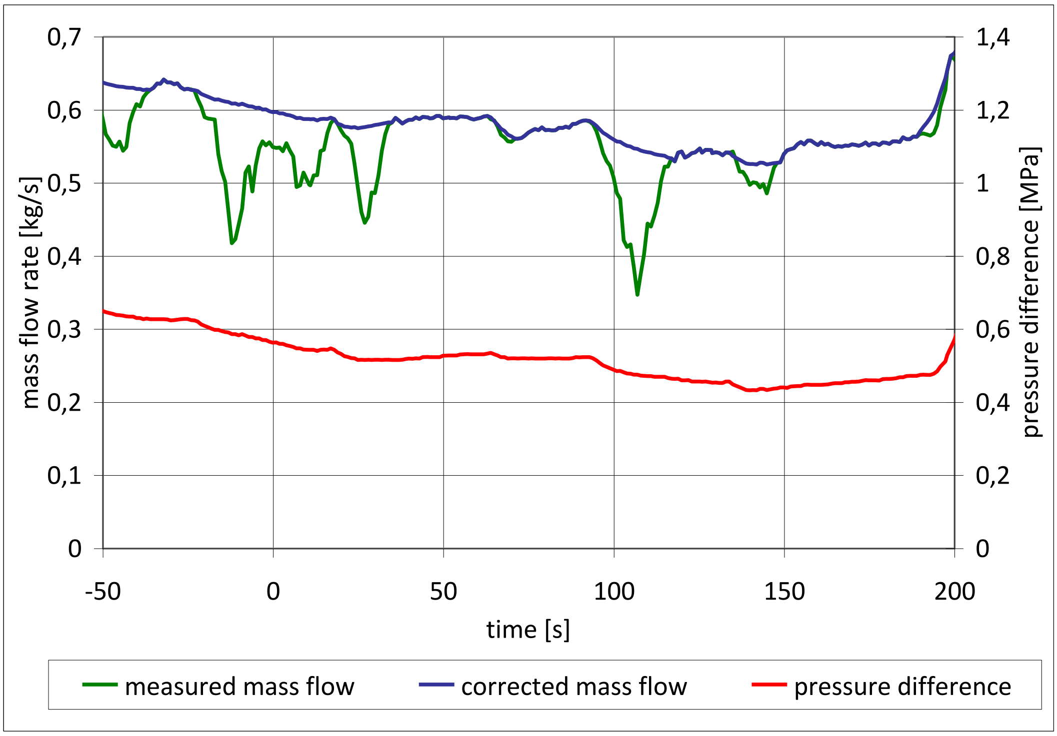

Fig. 5.9: Resulting mass flow correction for experiment 15-10

5.3 Accuracy estimation for the levels in the separators

The water level has been calculated with eqaution 5.4.

$$L = \frac{H \cdot (\rho_{KW} - \rho'') - \Delta p / g}{\rho' - \rho''} \tag{5.4}$$

See the definition of the variables below. Thus, the uncertainty (Δ_F) of the level is (5.5).

$$\boxed{\Delta_F L = \Delta_F \rho_{KW} \cdot \left|\frac{\partial L}{\partial \rho_{KW}}\right| + \Delta_F \rho'' \cdot \left|\frac{\partial L}{\partial \rho''}\right| + \Delta_F \rho' \cdot \left|\frac{\partial L}{\partial \rho'}\right| + \Delta_F \Delta p \cdot \left|\frac{\partial L}{\partial \Delta p}\right|} \tag{5.5}$$

The steam density ρ'' is certain by (5.6)

$$\begin{aligned}\Delta_F \rho'' &= \Delta_F\left(\rho_{LIBIF\,97}(\mathrm{PIC8-62})\right)\\ &\le \Delta_F p \cdot \left|\frac{\partial \rho''_{LIBIF\,97}}{\partial p}\right|_{\max}\\ &\le 0.0413\,\mathrm{bar}\cdot 0.536\,\frac{\mathrm{kg}}{\mathrm{m^3\ bar}} \le 0.0222\,\frac{kg}{m^3}\end{aligned} \tag{5.6}$$

and influences the water level by the value of (5.7),

$$\begin{aligned}\frac{\partial L}{\partial \rho''} &= \frac{H\cdot(\rho_{KW}-\rho') - \Delta p/g}{(\rho'-\rho'')^2}\\ &\le \frac{\left.H\cdot(\rho_{KW}-\rho')\right|_{\max} - \Delta p_{\min}/g}{\left.(\rho'-\rho'')^2\right|_{\min}}\\ &\le \frac{1.493\,\mathrm{m}\cdot 222\,\frac{\mathrm{kg}}{\mathrm{m^3}} - 0}{\left(746\,\frac{\mathrm{kg}}{\mathrm{m^3}}\right)^2} \le 5.956\cdot 10^{-4}\,\frac{\mathrm{m^4}}{\mathrm{kg}}\end{aligned} \tag{5.7}$$

resulting in a deviation of the level by (5.8). $\left.x\right|_{\max}$ and $\left.x\right|_{\min}$ stand for the maximum or minimum possible value over the whole possible range of values in all the experiments. These values have been calculated manually using a set of representative points.

$$\underline{\Delta_F \rho'' \cdot \left|\frac{\partial L}{\partial \rho''}\right| \le 0.013\,mm} \tag{5.8}$$

The uncertainty of the cold-water density ρ_{KW} in the chamber is expressed by:

$$\begin{aligned}\Delta_F \rho_{KW} &= \Delta_F\left(\rho_{LIBIF\,97}(\mathrm{PIC8-62;TIC8\text{-}61})\right)\\ &\le \Delta_F p \cdot \left|\frac{\partial \rho_{LIBIF\,97}}{\partial p}\right|_{\max} + \Delta_F t\cdot\left|\frac{\partial \rho_{LIBIF\,97}}{\partial t}\right|_{\max}\end{aligned} \tag{5.9}$$

$$\left|\frac{\partial \rho_{LIBIF\,97}}{\partial t}\right|_{\max} \cong \max_{t,p}\left(\left|\lim_{\Delta t\to 0}\left(\frac{\rho(p,t+\Delta t)-\rho(p,t)}{\Delta t}\right)\right|\right)\ ;\ \left|\frac{\partial \rho_{LIBIF\,97}}{\partial p}\right|_{\max}\ \text{analogue} \tag{5.10}$$

$$\Delta_F \rho_{KW} \le 0.0413\,\mathrm{bar}\cdot 0.045\,\frac{\mathrm{kg}}{\mathrm{m^3 bar}} + 1\,\mathrm{K}\cdot 0.500\,\frac{\mathrm{kg}}{\mathrm{m^3 K}} \le 0{,}502\,\frac{\mathrm{kg}}{\mathrm{m^3}} \tag{5.11}$$

$$\frac{\partial L}{\partial \rho_{KW}} = \frac{H}{\rho'-\rho''} \le \frac{H}{(\rho'-\rho'')_{\min}} \le \frac{1.493m}{746\,\frac{kg}{m^3}} \le 2.0002\cdot 10^{-3}\,\frac{m^4}{kg} \tag{5.12}$$

$$\underline{\Delta_F \rho_{KW} \cdot \left|\frac{\partial L}{\partial \rho_{KW}}\right| \le 1{,}005\,mm} \tag{5.13}$$

The saturated water densities ρ' impact is:

$$\begin{aligned}\Delta_F \rho' &= \Delta_F\left(\rho'_{LIBIF\,97}(\mathrm{PIC8-62})\right)\\ &\leq \Delta_F p \cdot \left|\frac{\partial \rho'_{LIBIF\,97}}{\partial p}\right|_{\max}\\ &\leq 0.0413\,\mathrm{bar} \cdot 3.811\,\frac{\mathrm{kg}}{\mathrm{m}^3\ \mathrm{bar}} \leq 0.1574\,\frac{kg}{m^3}\end{aligned} \tag{5.14}$$

$$\begin{aligned}\frac{\partial L}{\partial \rho'} &= \frac{H \cdot \left(\rho_{KW} - \rho''\right) - \Delta p / g}{\left(\rho' - \rho''\right)^2}\\ &\leq \frac{H \cdot \left(\rho_{KW} - \rho''\right)\Big|_{\max} - \Delta p_{\min} / g}{\left(\rho' - \rho''\right)^2\Big|_{\min}}\\ &\leq \frac{1.493\,\mathrm{m} \cdot 996.3\,\dfrac{\mathrm{kg}}{\mathrm{m}^3} - 0}{\left(746\,\dfrac{\mathrm{kg}}{\mathrm{m}^3}\right)^2} \leq 2.673 \cdot 10^{-3}\,\frac{\mathrm{m}^4}{\mathrm{kg}}\end{aligned} \tag{5.15}$$

$$\underline{\Delta_F \rho' \cdot \left|\frac{\partial L}{\partial \rho'}\right| \leq 0.421\,mm} \tag{5.16}$$

The pressure difference measurement Δp accuracy leads to:

$$\Delta_F \Delta p \leq 95\ \mathrm{Pa} \tag{5.17}$$

$$\begin{aligned}\left|\frac{\partial L}{\partial \Delta p}\right| &= \left|\frac{-1}{g \cdot \left(\rho' - \rho''\right)}\right| \leq \left|\frac{1}{g \cdot \left(\rho' - \rho''\right)\Big|_{\min}}\right|\\ &\leq \frac{1}{9.81\,\dfrac{\mathrm{m}}{\mathrm{s}^2} \cdot 746\,\dfrac{\mathrm{kg}}{\mathrm{m}^3}}\\ &\leq 1.367 \cdot 10^{-4}\,\frac{m^2 s^2}{kg}\end{aligned} \tag{5.18}$$

$$\underline{\Delta_F \Delta p \cdot \left|\frac{\partial L}{\partial \Delta p}\right| \leq 12.99\,\mathrm{mm}} \tag{5.19}$$

Finally, the uncertainty of the water level $\Delta_F L$ is smaller than $\boxed{14.43\,\mathrm{mm}}$.

$$\boxed{\begin{aligned}&\Delta_F L \leq 1.005\,\mathrm{mm} + 0.013\,\mathrm{mm} + 0.421\,\mathrm{mm} + 12.99\,\mathrm{mm}\\ &\underline{\underline{\Delta_F L \leq 14.43\,\mathrm{mm}}}\end{aligned}} \tag{5.20}$$

5.4 Test Data Sheets

To give a fast access to the main collected data of the experiments, data sheets have been created for each test. The header of every sheet contains (See Figure 3.1 for the nomenclature of the instrumentation):

- the name and the test type of the experiment;
    - average and experimental standard deviation[1] of:
        - pressure in the chamber (PIC862),
        - mass flow of the steam (FIC4-04/05) or the air (FIC4-10/11/12) and
        - mass flow of water (FIC8-31/32).
- A Diagram for the localisation of the test in the matrix is given in the top right corner.

Several diagrams below show the evolution of different signals over the time. The time scale is that of the high-speed camera. It begins with the first picture taken. A gray background represents the recording period. In order to understand the initialisation and some global processes, some seconds before and afterwards are shown in the plots. Vertical dashed lines are standing for begin and end of the period, where parameters for the test are set properly (e.g. valves are constant in a position).

- The first Diagram contains the pressure (in MPa) in the TOPFLOW facility separator (PIC1-06), the steam line before and after the control valves (PI1-07 -> PI4-06), the steam line next to the steam inlet (PI8-01) and the pressure chamber (PIC8-62).
- The second diagram shows the water level (in m) in the RPV simulator (LIC8-02) and the SG separator (LIC8-01).
- The next row displays the mass flow rate (in kg/s) of the liquid (for saturated water: FI8-31; for cold water: FI8-32) and the gas (for steam: FIC4-04/05; for air: FIC4-10/11/12). In addition, the corrected flow rate of the saturated water according to Chapter 5.2 is shown.
- The two diagrams in the bottom contain the pressure difference between both sides of the hot leg (PDI8-01) on the left side and the temperatures of the fluids on the right. More precisely, it is the subcooling of the fluids according to Equation 5.1 for steam experiments or respectively the absolute temperature for air experiments.

5.5 Water level plots

A good way of evaluating the experiments is the use of water level plots. A compilation is available in appendix VI. On the abscissa, the relative water level in the hot leg is represented; zero being the lower end (0.51 m) and one represents the upper end (0.76 m) of the horizontal channel. The ordinate displays the water level in the steam generator separator above 0.86 m, which is the vertical position of

---

[1] Average and standard deviation has been calculated for the time-frame, where the high speed camera was recording.

the overflow border in the model of the steam generator inlet-chamber. If this is above zero, water can run down into the hot leg model. Also in the water level plots, there are some diagonal lines labelled V_{tot}. They are isovolumetric-lines, which show the direction of the plot if there is no water injected and no condensate accumulated, but water may be interchanged between the two reservoirs. With their help, it is possible to estimate the amount of condensation during experiments without water injection. The difficulty, using these plots is that the time scale is not visible. Therefore, it is not noticeable, if the process is slow or fast.

6 Results

6.1 *Co-current Flow Experiments*

6.1.1 Observed Phenomena

As an example, one co-current flow experiment (13-22) was chosen to illustrate the observed phenomena. This run was performed at a system pressure of 30 bars and a temperature of about 230 °C, which is close to the saturation conditions. The mass flow rates were 0.31 kg/s for the water and 0.15 kg/s for the steam. Figure 6.1 shows the evolution in time of the water level in the separators and of the pressure drop over the test section. It is remarkable that the water level in the SG separator increases stepwise. This indicates that despite of the constant inlet flow rates, the water transport to the SG separator is discontinuous. This behaviour explains the periodic variation of the water level in the RPV simulator between 640 and 660 mm as well as the regular increase of the pressure drop over the test section.

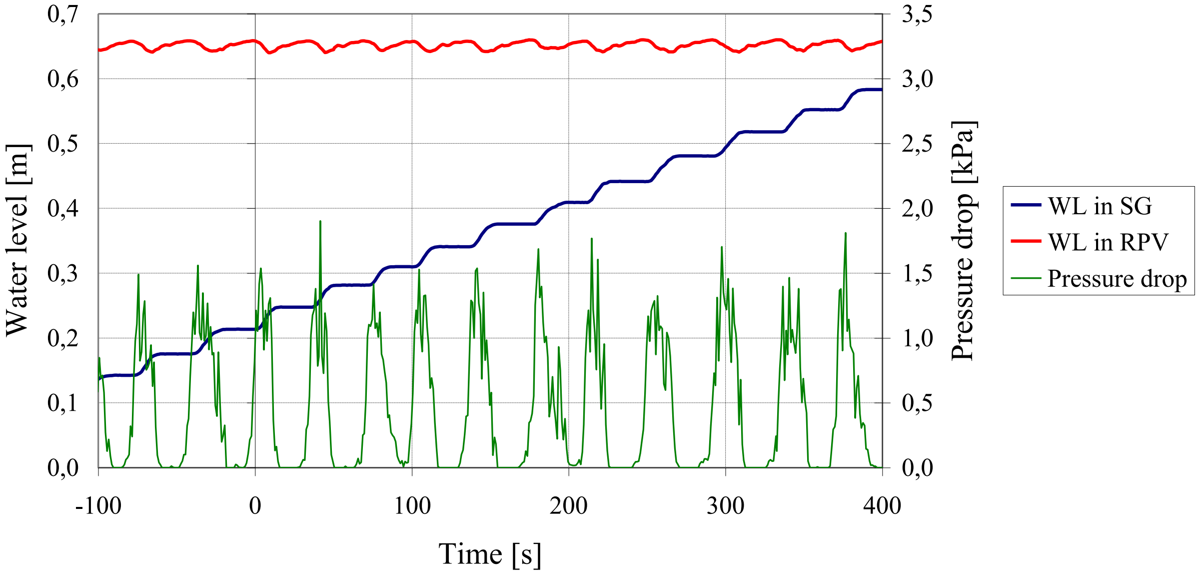

Fig. 6.1: Evolution of the water levels and pressure drop in time during a co-current flow experiment at 30.0 bar and 230 °C, with 0.31 kg/s water mass flow and 0.15 kg/s steam mass flow (exp. 13-22)

According to the flow structures observed with the high-speed camera over one period (c.f. Fig. 6.2), the following two flow regimes were observed:

1. First, for t < 31.6 s, the flow in the horizontal part of the channel is stratified wavy (Fig. 6.2-a) and no water is transported to the SG separator. This flow regime is characterised by a negligible pressure drop over the test section.

2. Afterwards, the water level in the horizontal part of the hot leg obstructs the steam flow enough to generate instable wave growth to plugs (Fig. 6.2-b and 6.2-c). Consequently, water is transported to the SG separator and the pressure difference between the separators increases and becomes unstable. For 40 < t < 45 s, the plugs become bigger (Fig. 6.2-d) and the amount of

transported water is higher than the injected flow rate. Therefore, the water level in the RPV simulator decreases, affecting the plug flow regime, which cannot be sustained after about 48 s (Fig. 6.2-e).

Subsequently, the flow in the horizontal part of the hot leg quiets and comes back to a wavy flow (Fig. 6.2-f), before the sequence starts over.

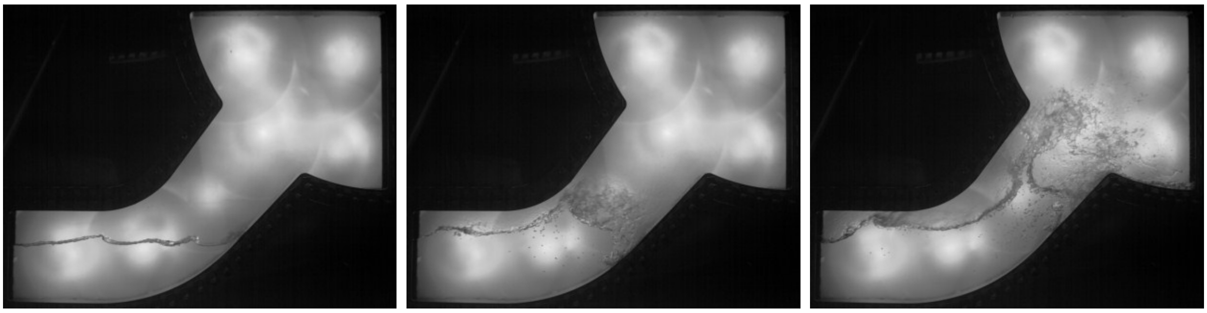

(a) t = 17.70 s (b) t = 31.75 s (c) t = 35.55 s

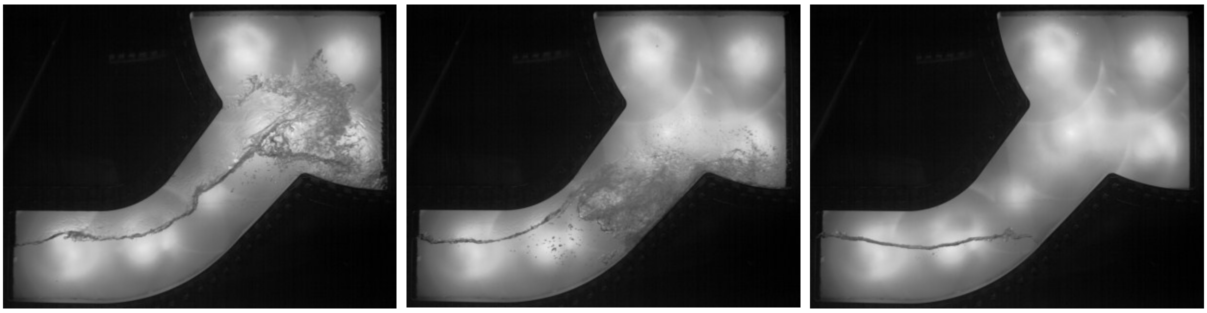

(d) t = 41.60 s (e) t = 46.80 s (f) t = 50.00 s

Fig. 6.2: Evolution of the interphase structure during a co-current flow experiment at 30.0 bar and 230°C, with gas mass flow0.30 kg/s and 0.15 kg/s

6.1.2 Probability distribution of the water level measured in the RPV simulator

The RPV water level is good measurable and gives valuable information about the flow condition in the riser. A statistical approach was applied to obtain quantitative data that can be compared to the results of CFD simulations.

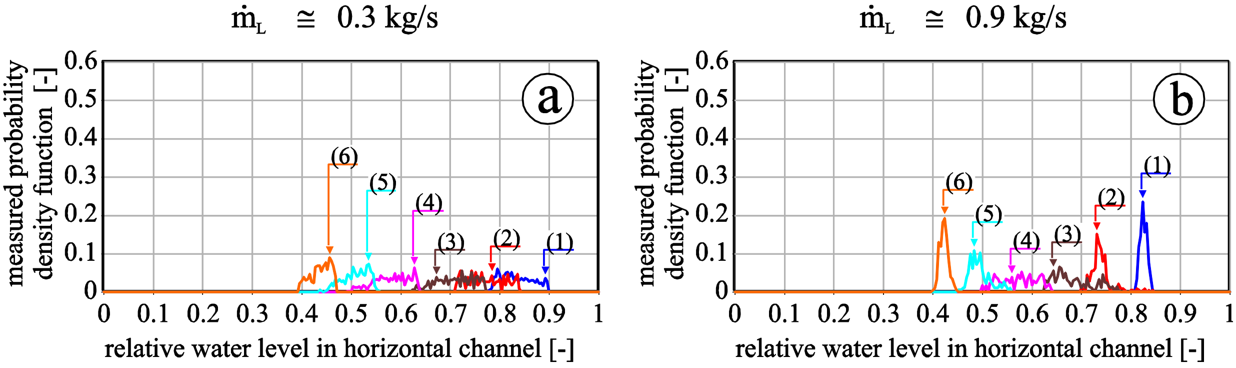

Fig. 6.3: measured probability density of the relative water level for different co current air/water flow experiments at 3 bars

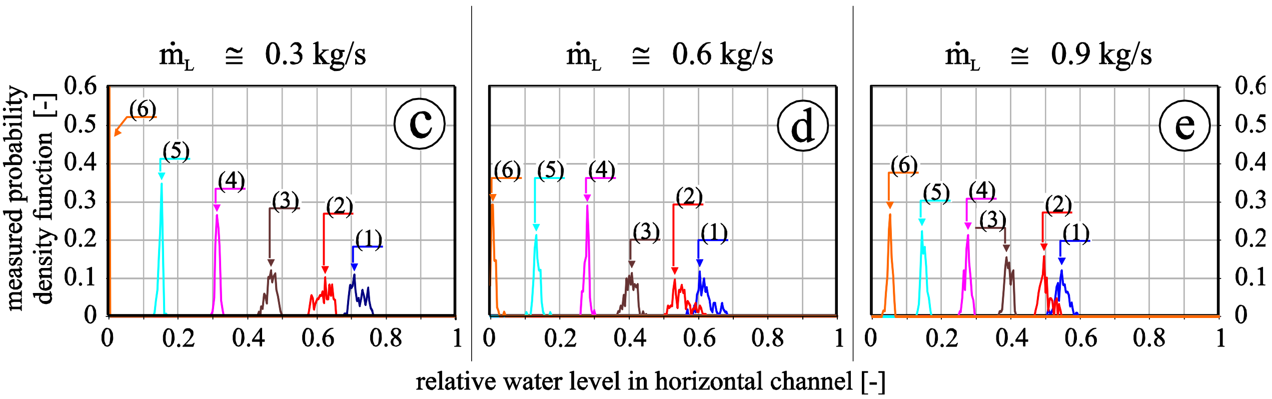

Fig. 6.4: measured probability density of the relative water level for different co current steam/water flow experiments at 15 bars

Probability density distributions of the water levels in the RPV-simulator were calculated from the available time series (for about 250 to 800 s, depending mainly on the water flow rate). In the mathematic strict sense, it is the relative frequency, but the more graspable notation was selected. The water level in the RPV simulator was scaled relatively to the height H of the horizontal part of the hot leg model as follows:

$$l = \frac{L - L_H}{H - L_H} \qquad (6.1)$$

with L_H being the level of the lower edge and H the higher edge of the horizontal channel.

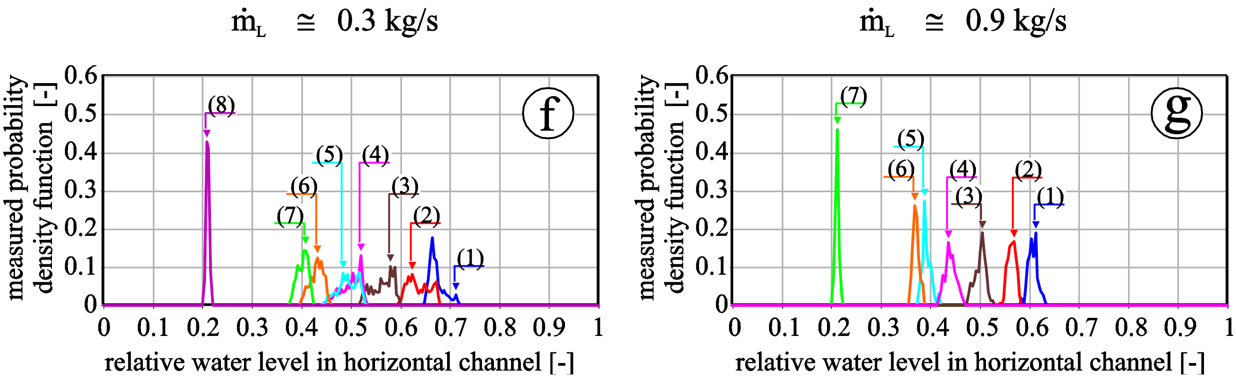

Fig. 6.5: measured probability density of the relative water level for different co current steam/water flow experiments at 30 bars

Probability distributions for different boundary conditions are presented in Figures 6.3 to 6.6. They are separated by the pressure, the used gas medium and the liquid injection mass flow. The exact flow rates measured during each experiment are listed in Table 6.1, where the runs are numbered according to the diagram letter followed by the number of the plot.

In all cases the water level in the RPV simulator, and consequently in the test section, decreases with an increase of the gas flow rate. Furthermore, the form of the distribution varies with the boundary conditions: the air/water experiments at 3.0 bars with $\dot{m}_L \cong 0.3\, kg/s$ (Diagram a) present very large and flat distributions whereas peaked curves were obtained with steam and water at 50.0 bar and $\dot{m}_L \cong 0.9\, kg/s$ (Diagram i).

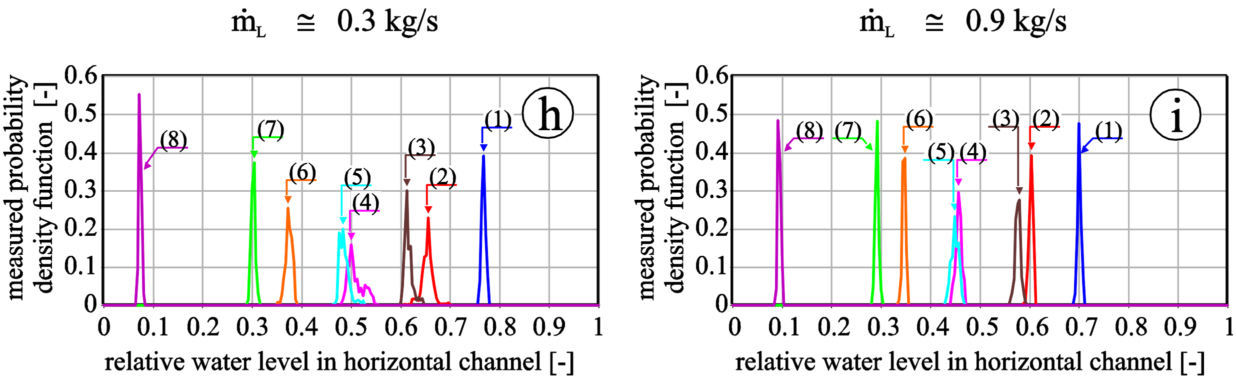

Fig. 6.6: measured probability density of the relative water level for different co current steam/water flow experiments at 50 bars

The form of the distribution informs about the stationarity of the water flow to the steam generator: the broader the distribution, the more discontinuous the transport is of water over time.

In this case, a narrow distribution is caused by a continuous transport of water, which characterises the presence of one stable flow condition. The broad distribution indicates that plug flow transports spontaneously more water to the SG separator than the water flow rate injected in the RPV simulator. In fact, when the injected water flow rate is lower than a certain value, the inequality in the input and output mass flow rates leads to an intermittent discharge of the water in the horizontal channel and consequently to a broad probability distribution. A flow regime transition is possible than.

Table 6.1 Specific measured data for the experiments shown in Figures 6.3 to 6.6. The plot number is combined of the diagram letter (a to i) and the plot number (1 to 8).

plot No.	Gas	Pressure [bar]	Mass flow rate liquid [g/s]	Mass flow rate gas [g/s]	Expe-riment No.
a-1	air	3.11 ±0.05	322 ±6	10.8 ±0.1	23-07
a-2	air	3.2 ±0.01	325 ±3	21.6 ±0.1	23-01
a-3	air	3.2 ±0.13	324 ±7	35.9 ±0.1	23-02
a-4	air	2.94 ±0.13	331 ±9	71.7 ±0.3	23-04
a-5	air	3 ±0.02	330 ±4	108 ±1	23-05
a-6	air	3.2 ±0.05	324 ±5	144 ±1	23-06
b-1	air	3.14 ±0.02	903 ±9	10.8 ±0.1	23-08
b-2	air	3.2 ±0.02	885 ±12	21.6 ±0.1	23-09
b-3	air	3 ±0.19	901 ±17	35.9 ±0.1	24-01
b-4	air	2.82 ±0.01	894 ±52	71.8 ±0.3	24-02
b-5	air	2.91 ±0.01	879 ±11	108 ±1	24-03
b-6	air	3.08 ±0.02	883 ±11	144 ±1	24-04
c-1	steam	15 ±0.1	335 ±3	35 ±0.3	14-01
c-2	steam	15 ±0.1	340 ±3	69.4 ±0.5	14-02

plot No.	Gas	Pressure [bar]		Mass flow rate liquid [g/s]		Mass flow rate gas [g/s]		Experiment No.
c-3	steam	15	±0.1	331	±3	150	±3	14-03
c-4	steam	15	±0.1	341	±3	251	±2	14-04
c-5	steam	15	±0.1	334	±3	402	±6	14-05
c-6	steam	15	±0.1	335	±4	585	±16	14-06
d-1	steam	15	±0.1	658	±4	36.3	±0.5	14-11
d-2	steam	15	±0.1	660	±2	68.1	±0.5	14-10
d-3	steam	15	±0.1	666	±2	150	±1	14-09
d-4	steam	15	±0.1	656	±1	249	±1	14-08
d-5	steam	15	±0.1	646	±2	403	±3	14-07
d-6	steam	15	±0.1	638	±2	597	±4	14-17
e-1	steam	15	±0.1	979	±4	36.7	±0.4	14-12
e-2	steam	15	±0.1	980	±5	69.4	±0.7	14-13
e-3	steam	15	±0.1	964	±5	150	±1	14-14
e-4	steam	15	±0.1	967	±5	248	±2	14-15
e-5	steam	15	±0.1	967	±6	394	±13	14-16
e-6	steam	15	±0.1	966	±3	608	±4	14-18
f-1	steam	30	±0.1	317	±1	74.9	±1	13-24
f-2	steam	30	±0.1	293	±2	99.4	±12.5	13-23
f-3	steam	30	±0.1	311	±2	149	±2	13-22
f-4	steam	30	±0.1	298	±2	197	±5	13-21
f-5	steam	30	±0.1	291	±2	200	±12	13-20
f-6	steam	30	±0.1	305	±1	249	±4	13-19
f-7	steam	30	±0.1	291	±1	320	±4	13-18
f-8	steam	30	±0.1	295	±1	500	±4	13-17
g-1	steam	30	±0.1	931	±5	74.8	±0.6	13-10
g-2	steam	30	±0.1	880	±3	100	±1	13-11
g-3	steam	30	±0.1	911	±5	150	±2	13-12
g-4	steam	30	±0.1	880	±6	200	±3	13-13
g-5	steam	30	±0.1	939	±5	250	±2	13-14
g-6	steam	30	±0.1	877	±4	315	±4	13-15
g-7	steam	30	±0.1	867	±7	499	±4	13-16

plot No.	Gas	Pressure [bar]		Mass flow rate liquid [g/s]		Mass flow rate gas [g/s]		Expe-riment No.
h-1	steam	50.2	±0.1	299	±1	75.9	±3.3	29-31
h-2	steam	50.4	±0.1	274	±1	135	±34	29-32
h-3	steam	50	±0.1	287	±1	152	±6	29-33
h-4	steam	50	±0.1	262	±3	249	±11	29-34
h-5	steam	50	±0.1	289	±3	250	±8	09-11
h-6	steam	50	±0.1	268	±2	425	±11	09-10
h-7	steam	50	±0.1	271	±2	510	±21	09-09
h-8	steam	50	±0.1	260	±2	834	±13	29-45
i-1	steam	50	±0.1	881	±7	76.7	±1.3	29-41
i-2	steam	50	±0.1	788	±10	131	±2	29-40
i-3	steam	50	±0.1	886	±5	152	±2	29-38
i-4	steam	50	±0.1	773	±8	246	±5	29-35
i-5	steam	50	±0.1	885	±5	254	±6	29-36
i-6	steam	50	±0.1	779	±6	433	±6	29-42
i-7	steam	50	±0.1	786	±9	502	±6	29-43
i-8	steam	50	±0.1	790	±8	835	±13	29-44

In order to interpret the evolution of the form of the distributions with the gas flow rate, typical flow pictures taken during different co-current flow experiments are presented in Figure 6.7. As an example, the experiments were chosen at the extrema of the available boundary conditions.

At low gas flow rates, the flow regime was identified as elongated bubble flow (Fig. 6.7, left column) and as slug flow at high gas flow rates (Fig. 6.7, right column). The probability distributions corresponding to these experiments are peaked. In the case of elongated bubble flow, the transport of water is continuous due to overflow as can be seen in the images. During slug flow, the transport of water occurs with droplets that detach from the wave front, which is also a continuous mechanism. At intermediate gas flow rates (Fig. 6.7, middle column), the water transport is periodic and the probability distribution of the water level is flat, like in the experiment presented in section 6.1.1. These observations allow concluding that a change in the form of the probability distribution from peaked over flat to peaked indicates different flow regimes.

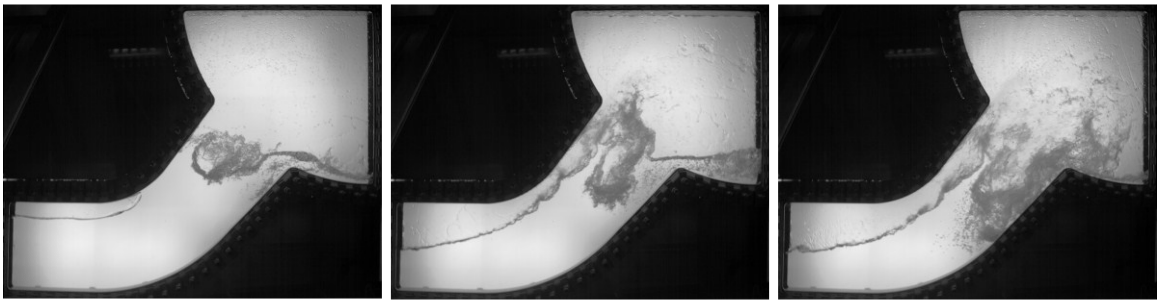

Exp. b-1: = 11 g/s Exp. b-4: = 72 g/s Exp. b-6: = 144 g/s

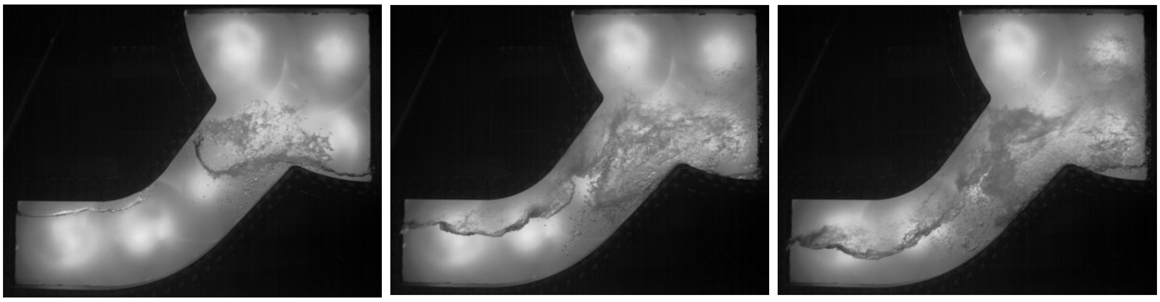

Exp. i-1: = 76 g/s Exp. i-6: = 0.43 kg/s Exp. i-8: = 0.84 kg/s

Fig. 6.7: Typical flow pictures taken during different co-current flow experiments with ≈ 0.90 kg/s

6.2 *Counter Current Flow Experiments*

6.2.1 Observed phenomena

As an example, the counter-current flow experiment 13-08 was chosen to illustrate the available data. This run was performed at a system pressure of 3.0 MPa and a temperature of about 232°C, which is close to the saturation conditions. The mass flow rates were 0.88 kg/s for the water and 0.20 kg/s for the steam. Figure 6.8 shows the evolution of the water level in the separators and of the pressure drop over the test section.

Before the beginning of slug flow generation in the test-section ($t \leq 20$ s), the water injected in the SG separator flows through the test section to the RPV simulator (Fig. 6.9-a). Therefore, the water level in the SG separator is constant at about 0.86 m and the water level in the RPV simulator increases. At about $t = 20$ s, the water level in the horizontal part of the hot leg obstructs the steam flow enough to generate waves at the interface, which finally grow to slugs (Fig. 6.9-b). Consequently, the pressure difference between the separators increases and becomes unstable. Afterwards, the gas hindering the water to flow to the RPV, it accumulates in the SG separator. The mean pressure drop over the test section increases with the water level in the SG and the slugs become bigger (Fig. 6.9-c).

To illustrate the experiments further, a series of counter-current flow runs performed at similar Wallis parameters J^* were compared. The boundary conditions of the compared experiments are given in table 6.2. The flow rates correspond to a Wallis parameter of about 0.050 for the water and about 0.094 for the gas. Figure 6.10 shows camera pictures of the flow at a water level of about 1 m in the SG-separator (i.e. at t = 60 s for the 3.0 MPa experiment – see Fig. 6.8). The aspect of the flow shown at different boundary conditions presents qualitative similarities. However, because of the unsteady character of slug flow, a detailed analysis of various global parameters is necessary. Furthermore, the application of image processing methods to the picture sequences could deliver local information in order to complete this analysis.

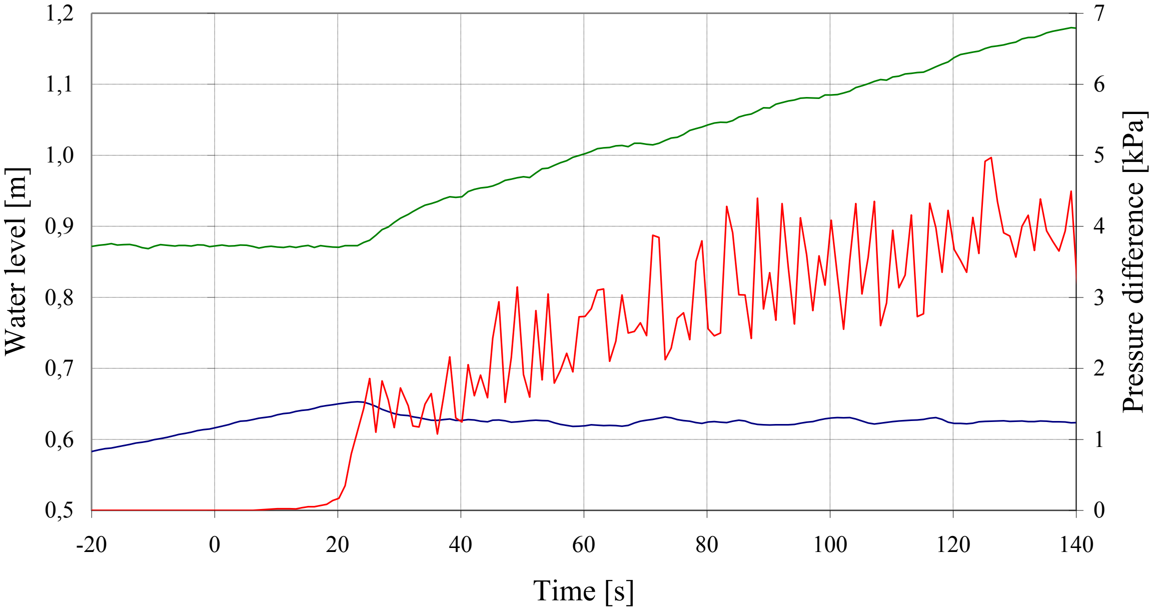

Fig. 6.8: Evolution of the water level in the RPV simulator (in blue) and SG separator (in green) and of the pressure difference (in red) during a counter-current flow experiment at 3.0 MPa with $\dot{m}_L$ = 0.88 kg/s and $\dot{m}_G$ = 0.20 kg/s

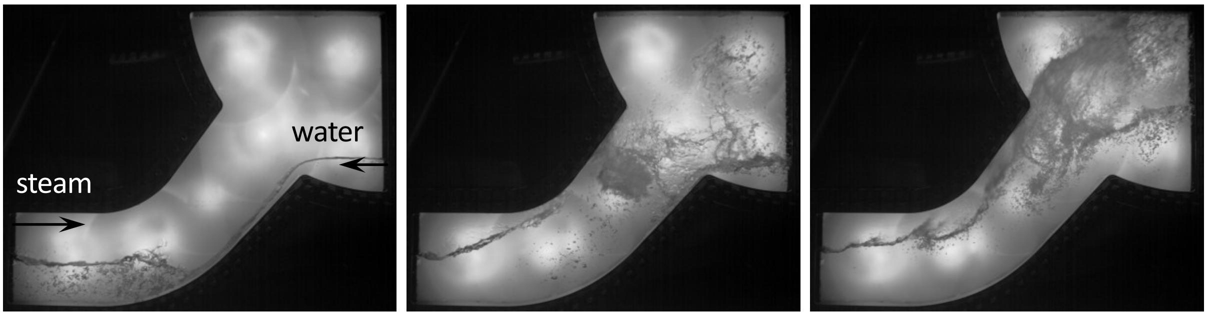

a) *t* = 0.00 s

b) *t* = 23.00 s

c) *t* = 80.00 s

Fig. 6.9: Evolution of the flow during the steam/water counter-current flow experiment performed at 3.0 MPa with $\dot{m}_L$ = 0.88 kg/s and $\dot{m}_G$ = 0.20 kg/s

Table 6.2: Boundary conditions of the compared counter-current flow experiments

gas / run number	air / 24-12	steam / 17-13	steam / 13-08	steam / 15-15
pressure [MPa]	0.3	1.5	3.0	5.0
temperature [°C]	20 - 25	197	232	262
gas flow rate [kg/s]	0.108	0.15	0.20	0.25
water flow rate [kg/s]	0.90	0.98	0.88	0.78

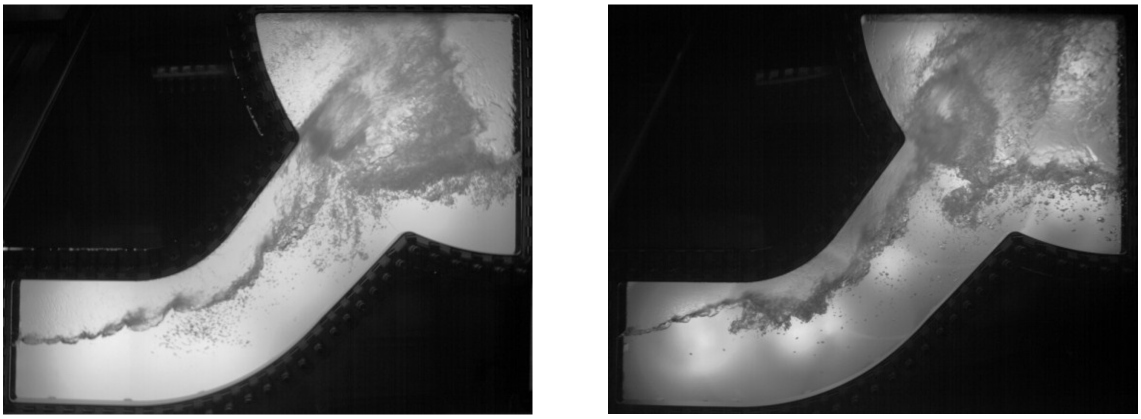

a) air/water – 0.3 MPa b) steam/water – 1.5 MPa

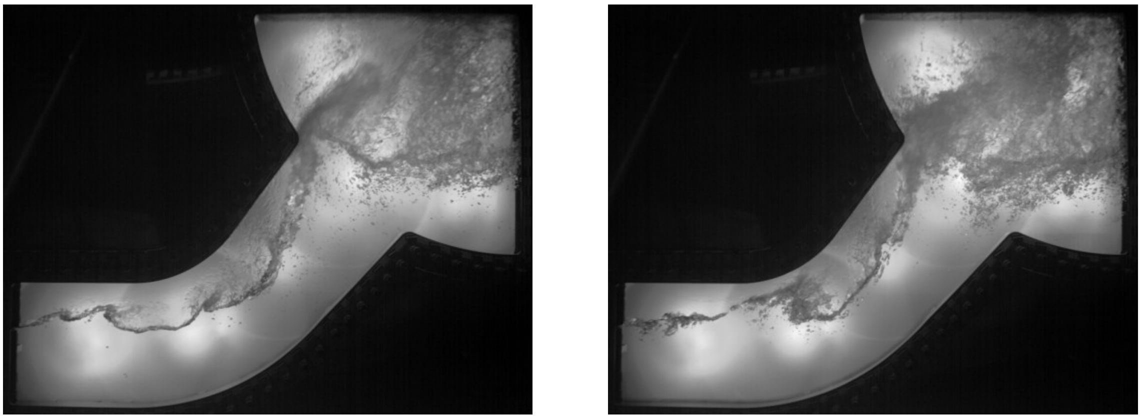

c) steam/water – 3.0 MPa d) steam/water – 5.0 MPa

Fig. 6.10: Example of images obtained at different pressures during counter-current flow experiments

6.3 Experiments without water injection or drainage

The experiment 30-22 was chosen to illustrate the flow conditions at experiments without water injection. It was performed at a pressure of 0.3 MPa and an air mass flow rate of about 43 g/s. Figure 6.11 shows the evolution of the water level in the separators and of the pressure drop over the test section. The dashed lines stand for the water level position of the horizontal channel (0.51 m to 0.76 m) and height of the water spill edge of the steam generator separator (0.86 m). A periodic process is observed in all three shown plots. Several exemplary pictures are shown in figure 6.12. To understand the flow pattern easier, we discuss a period between the time steps 14 s and 61 s. At 14 s the water flows down from the SG-separator to the horizontal channel. The level in the channel is not high enough for the gas flow to transport water back to the steam generator. The water blocks the gas flow in the end of the horizontal part at the first time at 16 s. That leads to an increase of the gas pressure difference. Due to the blocked channel, the gas with the increasing pressure can assign its momentum to the blocking water layer, which is accelerated and transported to the SG-separator (see figure 6.12-c). Due to this movement of the generally constant water volume, the water level falls in the RPV-simulator and rises in the SG-separator. At approximately 32 s the level in the horizontal channel is so low, that the back flowing water does not reach the upper wall of the channel (see figure 6.12-d), so the water transport stops and the pressure difference falls down to nearly zero. Between 34 s and 61 s, the water just flows down from the SG-separator and the process begins again.

Not all the experiments show such periodic processes. There are also runs with a nearly steady state of the water levels and the pressure difference. (see the data sheet of 30-26 as an example)

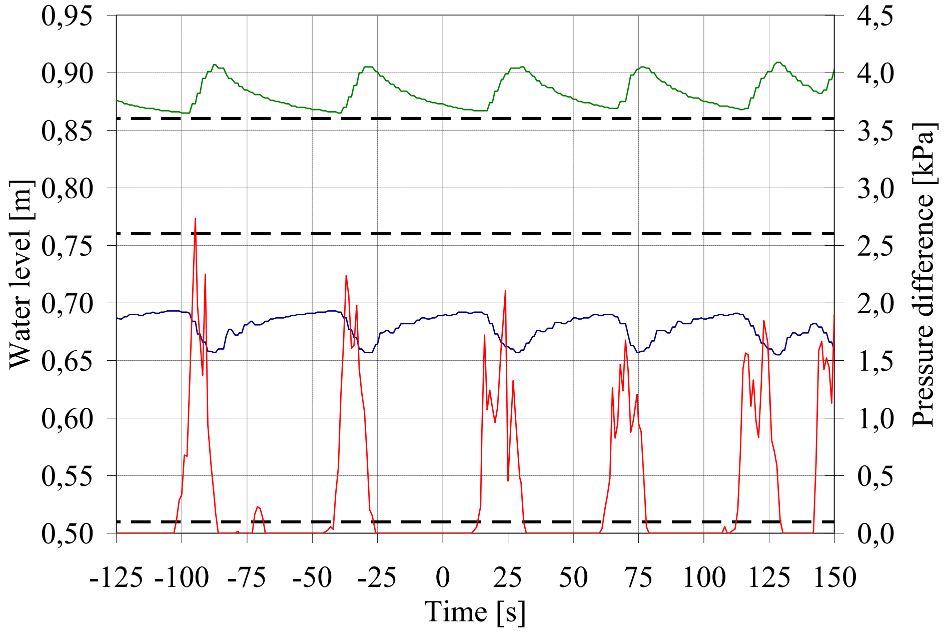

Fig. 6.11 Evolution of the water level in the RPV simulator (in blue) and SG separator (in green) and of the pressure difference (in red) during an air/water experiment without water injection at 0.3 MPa with $\dot{m}_G$ = 43 g/s (exp. 30-22)

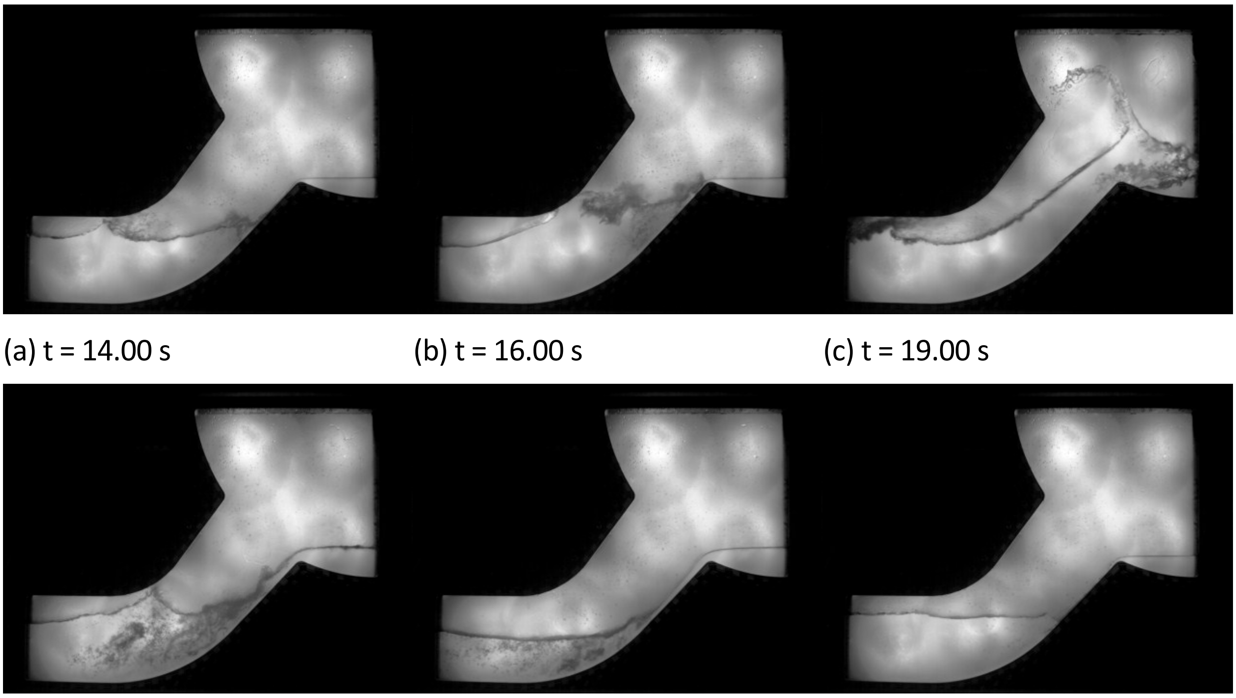

(a) t = 14.00 s

(b) t = 16.00 s

(c) t = 19.00 s

(d) t = 31.60 s

(e) t = 34.00 s

(f) t = 61.00 s

Fig. 6.12 Observed flow behaviour during the exemplary experiment without water injection (exp. 30-22)

6.4 Counter Current Flow Limitation Experiments

6.4.1 Flow behaviour

6.4.1.1 Flow behaviour observed with air/water

The phenomena are illustrated by an air-water experiment at a water mass flow of 0.3 kg/s. Fig. 6.13 shows the water levels measured in the SG and RPV separators, the pressure difference between the two vessels and the injected air mass flow rate. During this flooding experiment (increasing gas mass flow) performed at a system pressure of 3.0 bar, constant water mass flow rate of 0.3 kg/s was injected. The water levels inside both separators are shown in the upper graph. The pressure difference between the vessels and the injected air mass flow rate are represented in the lower graph of this figure. From the slopes of the curve of the water level in the RPV simulator shown in Fig. 6.13, the experiment can be divided into three regions:

(1) In the first region (Fig. 6.13: Region I), the water level in the RPV simulator increases with the increase of air mass flow rate, meanwhile the water level in the SG separator is almost constant. This means that all the injected water flows from the SG separator to the RPV simulator. In this region, it is also found that the pressure difference between the vessels is still low, and slightly increases with the air mass flow rate. We defined this region as the stable counter-current flow. The flow behaviour illustrated by high-speed camera images is shown in Fig. 6.14. It should be noticed that the flow pattern on the inclined plane of the riser is a supercritical stratified flow for $t < 61.0$ s. Supercritical flow means that the local Froude number of the liquid film is larger than unity. In the geometry of the hot leg, the supercritical flow condition is due to gravity acceleration. In the horizontal part of the hot leg, the supercritical flow changes to subcritical flow, and a hydraulic jump as a transition from supercritical to subcritical flow is observed near the bended region (Fig. 6.14-a). Furthermore, the air/water interface in the inclined riser is stable; indicating that the water flow is not disturbed by the air stream.

(2) At an injected air mass flow rate of 0.30 kg/s (Fig. 6.13: $t = 61.0$ s), a limitation of the discharge water flow is detected. Here the slope of the curve of water level in the RPV simulator and SG separator begin to decrease and increase, respectively. This means that a part of the water injected in the SG separator does not flow to the side of the RPV simulator. This point is defined as the onset of flooding, and the subsequent region II as the partial delivery region. Around the onset of flooding, the pressure difference between the vessels begins to present higher fluctuations as shown in the lower graph of Fig. 6.13. Visual observation indicates that at this point, the air/water interface becomes wavier and a large amplitude wave grows with droplet entrainment from its crest. This phenomenon was captured by the camera and is shown in Fig. 6.14-b. Due to the waves, the free cross-section available for the air flow decreases. Therefore the air is accelerated above the wave, this starts to blow up the liquid slug, finally breaking up the slug into small droplets. With further increase of the air mass flow rate, the liquid slugs reduce and sometimes block the whole cross section for the air flow in the test section. Consequently, the pressure drop over the test-section increases at these flow conditions (= 0.32 kg/s), which is revealed by the pressure difference measured between the vessels.

(3) With further increasing of the air mass flow rate up to 0.34 kg/s (Fig. 6.13: $t = 97.9$ s), all the injected water mass flow rate of 0.3 kg/s is hindered to flow to the RPV simulator and the water level

measured in the RPV shows a plateau (region III). Therefore, the water remains completely in the test section and in the SG separator, where the water level rises. This region corresponds to the zero liquid penetration. The visual observations indicate that large amplitude rolling waves are formed near the bend and block the cross section of the rectangular duct. Furthermore, large two-phase mixing regions were observed with droplet detachment at the wave crest and bubble entrainment in the bended region due to the rolling flow pattern (see Fig. 6.14-c).

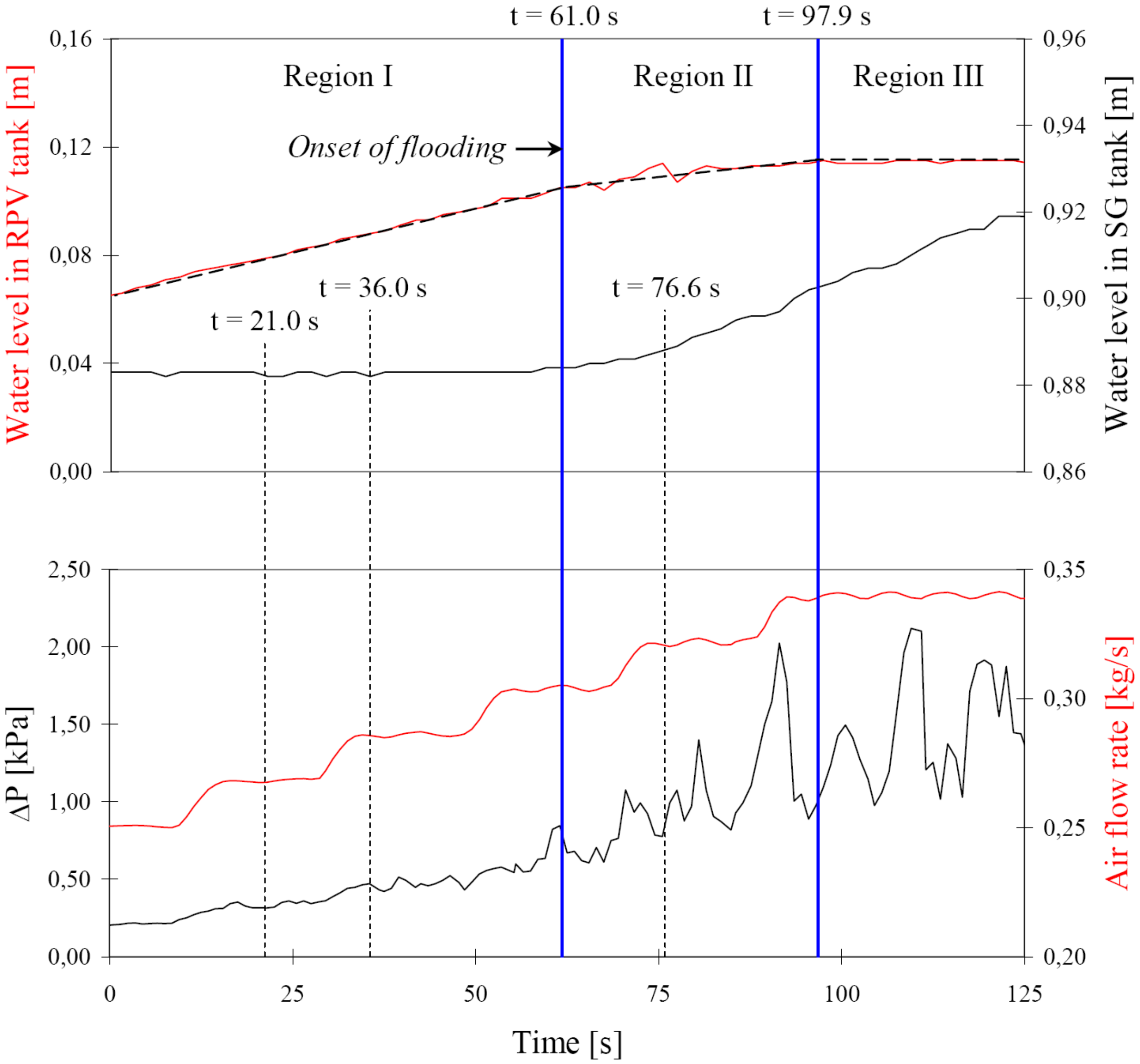

Fig. 6.13: Variation of the water levels in the RPV simulator (top diagram, red curve with dashed linear regression) and in the SG separator (top diagram, black curve), of the air mass flow rate (bottom diagram, red curve) and of the pressure drop over the test-section (bottom diagram, black curve) measured at a water mass flow rate of 0.3 kg/s and a pressure of 3.0 bar (exp. 30-05)

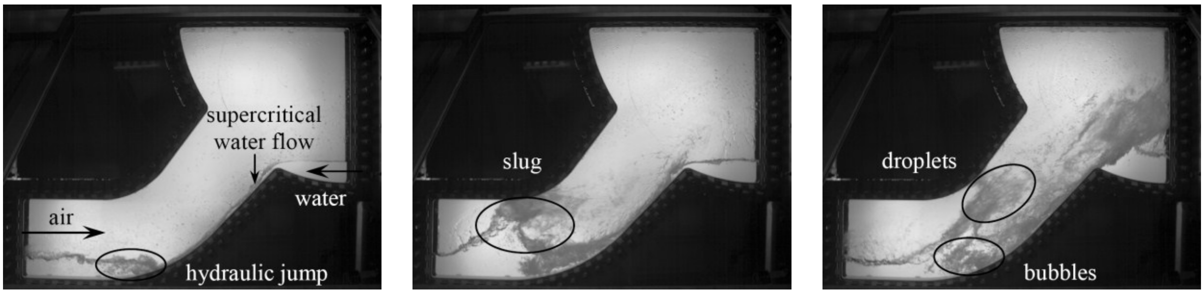

(a) $\dot{m}_G$ = 0.27 kg/s; t = 21.00 s (b) $\dot{m}_G$ = 0.32 kg/s ; t = 76.59 s (c) $\dot{m}_G$ = 0.34 kg/s ; t = 97.92 s

Fig. 6.14: Flow behaviour during the counter-current flow of air and water at a water flow rate of 0.3 kg/s, and a pressure of 3.0 bar (exp. 30-05)

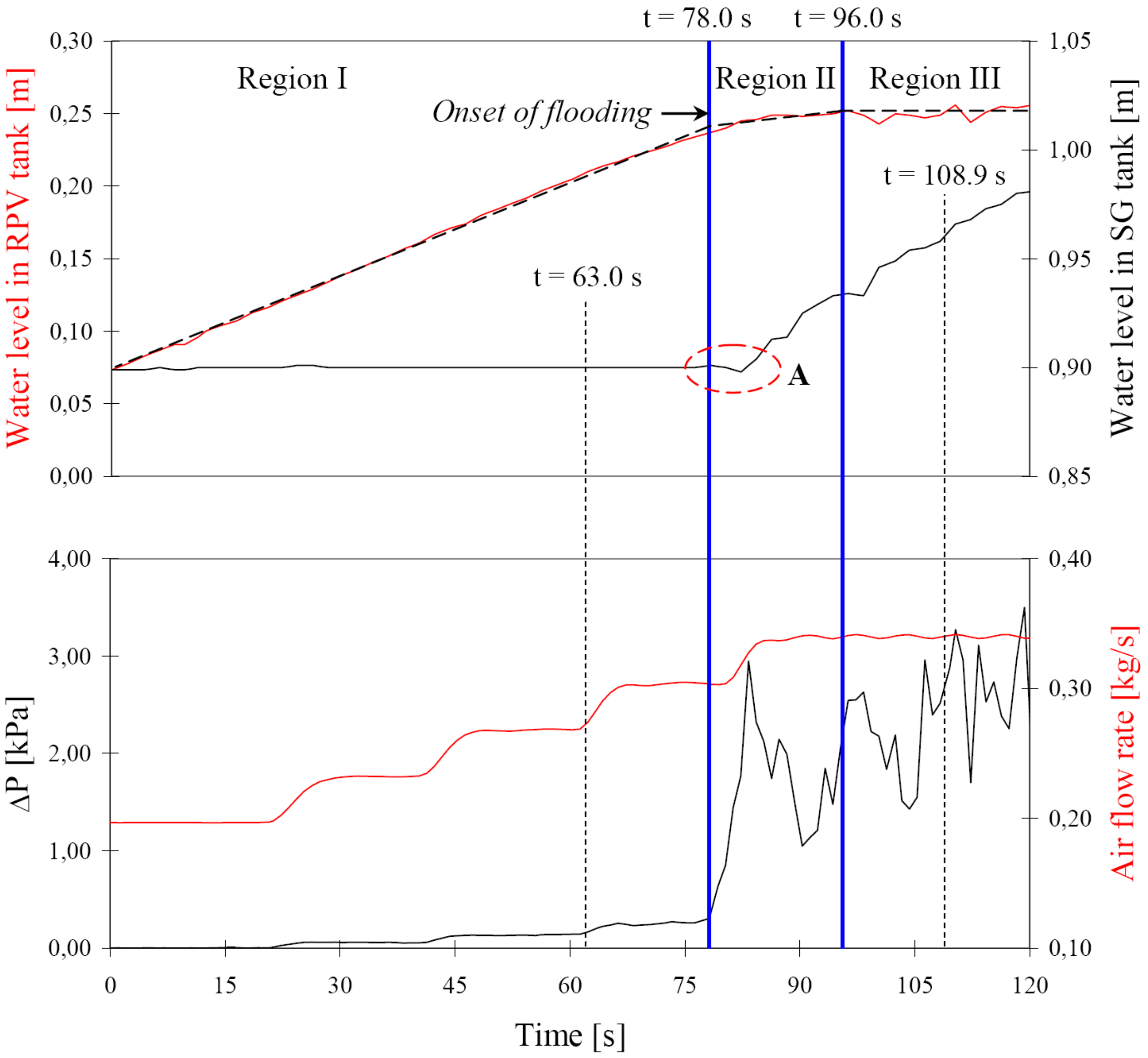

Fig. 6.15: Variation of the water levels in the SG separator (top diagram, black curve) and in the RPV simulator (top diagram, red curve and dashed linear regression), of the pressure difference between the vessels (bottom diagram, black curve) and of the air mass flow rate (bottom diagram, red curve) measured at a water mass flow rate of 0.9 kg/s and a pressure of 3.0 bar (exp. 30-01)

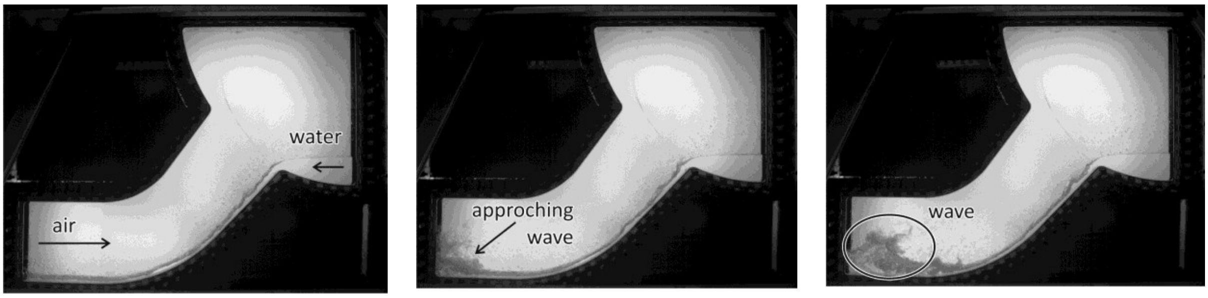

(a) before the onset of flooding
(t = 63.00 s; $\dot{m}_G$ = 0.27 kg/s)

(b) at the onset of flooding
(t = 78.00 s; $\dot{m}_G$ = 0.30 kg/s)

(c) t = 78.60 s; $\dot{m}_G$ = 0.30 kg/s

(d) t = 79.10 s; $\dot{m}_G$ = 0.30 kg/s

(e) t = 96.00 s; $\dot{m}_G$ = 0.34 kg/s

(f) t = 108.90 s; $\dot{m}_G$ = 0.34 kg/s

Fig. 6.16: Flow behaviour observed during the counter-current flow experiment at a water flow rate of 0.9 kg/s and pressure of 3.0 bar (exp. 30-01)

To illustrate the effects of a different water flow rate, an air-water experiment with a higher water mass flow rate of 0.9 kg/s is considered. The measured global parameters are shown in Fig. 6.15, which indicate also three main flow regions are similar to the before dicussed:

(1) In Region I of stable counter-current flow, the water level in the RPV separator increases and the water level in the SG simulator keeps constant. The pressure difference between the vessels is low and stable. From visual observations, it is noted that before the inception of flooding (t = 78.0 s), the flow pattern is also a supercritical stratified flow, but no hydraulic jump is detected in the bended region as shown in Fig. 6.16-a.

(2) Again an injected air mass flow rate of 0.30 kg/s (Fig. 6.15: t > 78.0 s), a limitation of the counter-current flow is detected, as marked as the onset of flooding in Fig. 6.15. Close inspection of the figure reveals that the behaviour of water levels changes a little with the increased water mass flow rate. At the initiation of flooding, the slope of water level in the RPV simulator begins to decrease. Meanwhile, the water level in the SG separator remains almost constant for about 5.5 seconds. This phenomenon is marked as ”A” in Fig. 6.15 and means that a part of the liquid does not flow to either of the tanks. During this period of time, the high-speed camera images indicate that the water flow begins to be partially reversed. Therefore, at the initial stage of flooding, the flow in the horizontal part of the hot leg becomes subcritical and bigger waves are observed (Fig. 6.16-b to d). This causes an accumulation of water in the test section, which explains the decrease of the slope of water level measured in the RPV simulator. Furthermore, no liquid is transported to the steam generator inlet chamber, neither from waves nor from droplets. Consequently, the water level in the SG separator

remains relatively constant. In the region II, the behaviour of the pressure drop in the test section is found to be similar to that at lower water mass flow rate (= 0.3 kg/s), while the absolute maximum pressure difference measured increases with higher water flow rate.

(3) The zero liquid penetration is reached with further increasing of the air mass flow rate up to 0.34 kg/s (Fig. 6.15: t = 96.0 s). The visual observations (Fig. 6.16-e and 6.16-f) indicate that in the region III, the flow behaviour is similar to that at lower water mass flow rate (= 0.3 kg/s) with highly mixed zones.

6.4.1.2 Flow behaviour observed with steam/water

As an example, one of the steam/water experiments was chosen to compare the observed phenomena. This run was performed at following boundary conditions: a system pressure of 50.0 bar, a temperature of about 262°C and a water flow rate of 0.70 kg/s (exp. 06-14). An analysis of the evolution of the global parameters over time (Figure 6.18) allows characterising the flow behaviour.

I. For a steam flow rate lower than 0.82 kg/s (t < 65 s), the water level in the SG separator is constant and the slope of the water level increase in the RPV simulator corresponds to a water flow rate of 0.71 kg/s, which is very close to the injected mass flow rate. This indicates a stable counter-current flow, confirmed by the camera images (Figure 6.17-a), which is characterised by a constant and very low pressure drop over the test section (< 0.2 kPa).

II. At t = 65 s, the steam flow rate is increased to about 0.94 kg/s (±0.02). Immediately, the pressure difference between the separators increases, indicating the beginning of the counter-current flow limitation. With a delay of about 5 s, the slope of the water level in the RPV simulator decreases to a discharge water flow of 0.23 kg/s. Consequently, the water level in the SG separator increases significantly. Furthermore, the pressure difference between the separators becomes unstable and fluctuates between 1 and 2.5 kPa due to the slugs generated in the hot leg (Figure 6.17-b).

III. For 105 < t < 150 s, the steam flow rate is slowly increased to values up to 0.99 kg/s. This further reduces the discharge water flow to a minimum of 0.08 kg/s and the pressure drop over the test section increases up to values over 4 kPa. The camera pictures (Figure 6.17-c) reveal a highly mixed two-phase flow: big slugs are observed which flow up the riser and transport water into the SG separator, where the water accumulates. Zero penetration was not reached in the steam experiments.

The slight decrease of the steam flow rate at the end of the experiment leads to a decreasing CCFL intensity after t = 150 s, which is similar to the processes observed during df experiments. The flow conditions described here are similar to those observed during the air/water experiments reported in the previous sections.

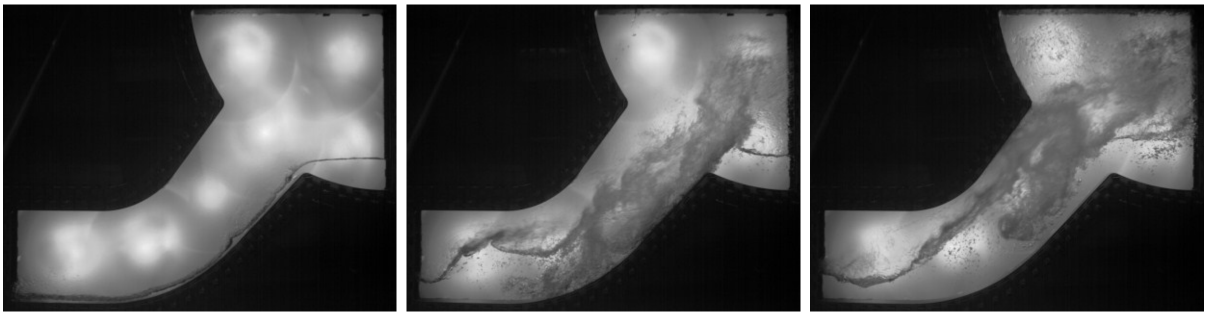

(a) t = 60.00 s (b) t = 80.25 s (c) t = 125.28 s

Fig. 6.17: Flow behaviour during steam/water counter-current flow at = 0.70 kg/s and p = 50.0 bar (exp. 06-14)

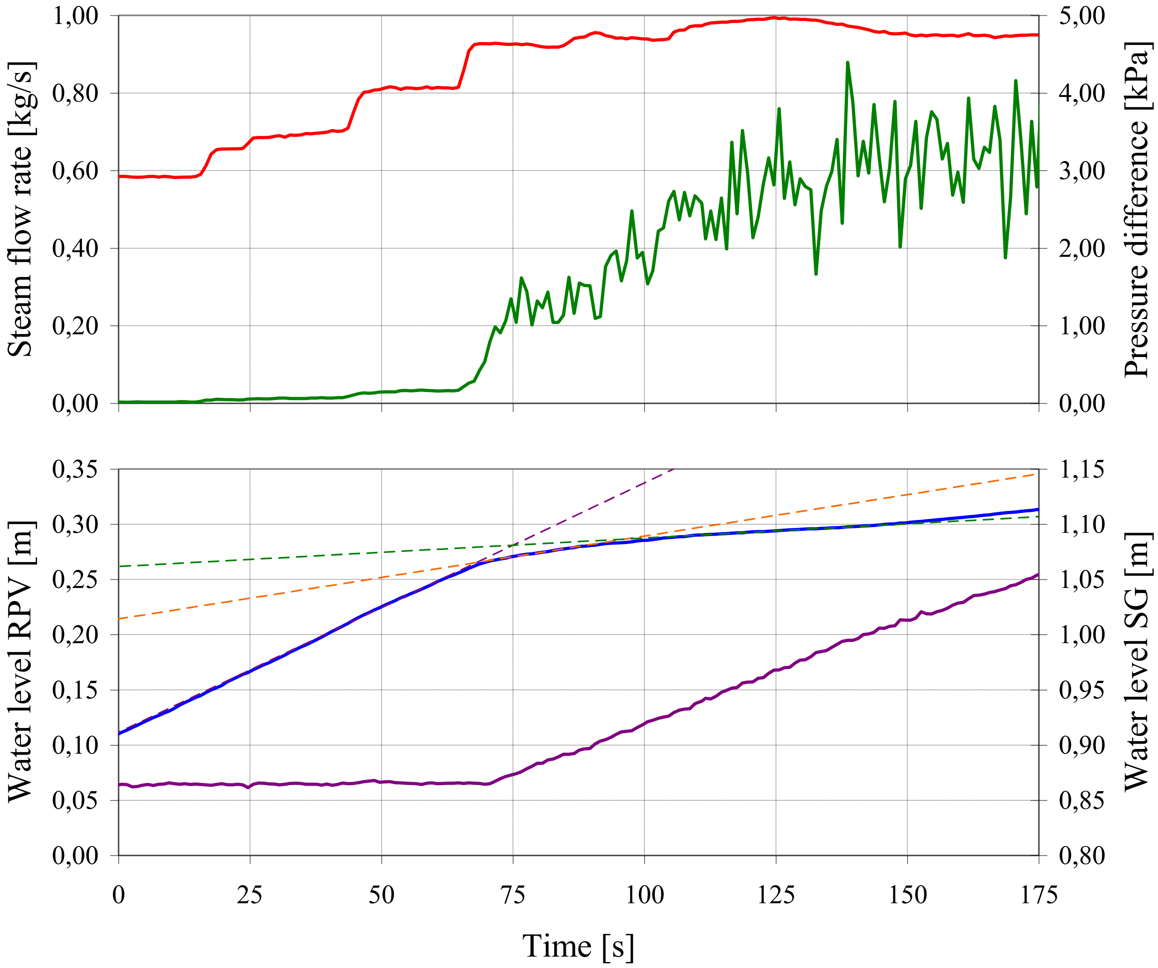

Fig. 6.18: Variation of the steam mass flow rate (top diagram, red curve), of the pressure drop over the test section (top diagram, green curve), of the water level in the RPV simulator (bottom diagram, blue curve) and in the SG separator (bottom diagram, purple curve) during the CCFL experiment at $\dot{m}_L$ = 0.70 kg/s and p = 50 bar (exp. 06-14)

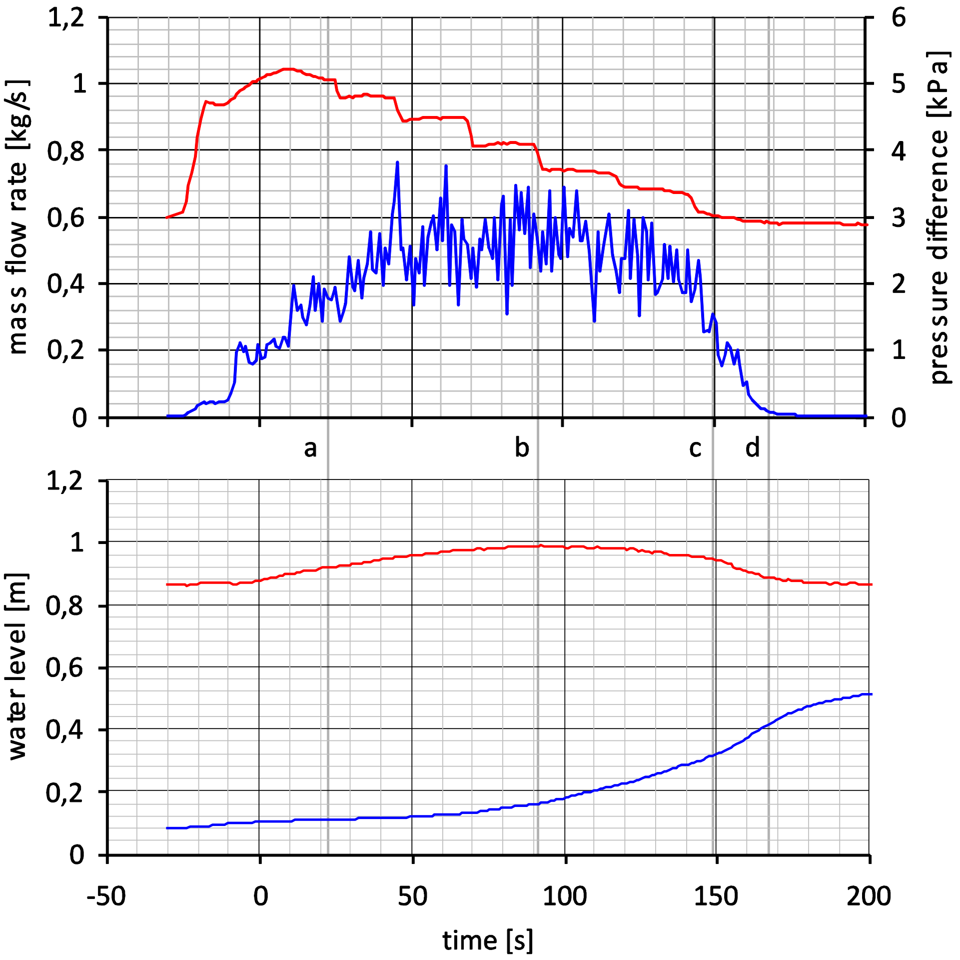

Fig. 6.19: Variation of the steam mass flow rate (red line in top diagram), of the pressure drop over the test section (blue line in top diagram), of the water level in the RPV simulator (blue line in bottom diagram) and in the SG separator (red line in bottom diagram) during the CCFL-deflooding experiment at $\dot{m}_L$ = 0.60 kg/s and p = 50 bar (run 06-18)

In order to illustrate the differences between flooding and deflooding experiments, the run number 06-18 is described below. It is a deflooding-CCFL experiment at 50 bar pressure and a liquid mass flow rate of 0.6 kg/s. Figures 6.19 and 6.20 show the evolution of the levels and the camera pictures for this experiment. Before the start of the experiment (-25s), the steam mass flow rate is too low to initiate flooding. At -20 s the gas flow rate was increased and, consequently, the pressure loss started to rise. The obstructed water flow that leads to the pressure drop is visible in picture 6.20a. The water discharge through the test section dropped down and the water level in the SG-separator began to rise. During the experiment, the gas mass flow rate was decreased stepwise and the water discharge rate accordingly increases. At about 90 s (Fig. 6.20b), the level in the SG-separator reaches its maximum. Due to the falling gas mass flow, the discharge to the RPV-simulator restarted.

At the end of the experiment, the accumulated water in the SG-separator discharges at a higher mass flow rate, than the injected mass flow. This makes it possible to calculate the deflooding line in this region.

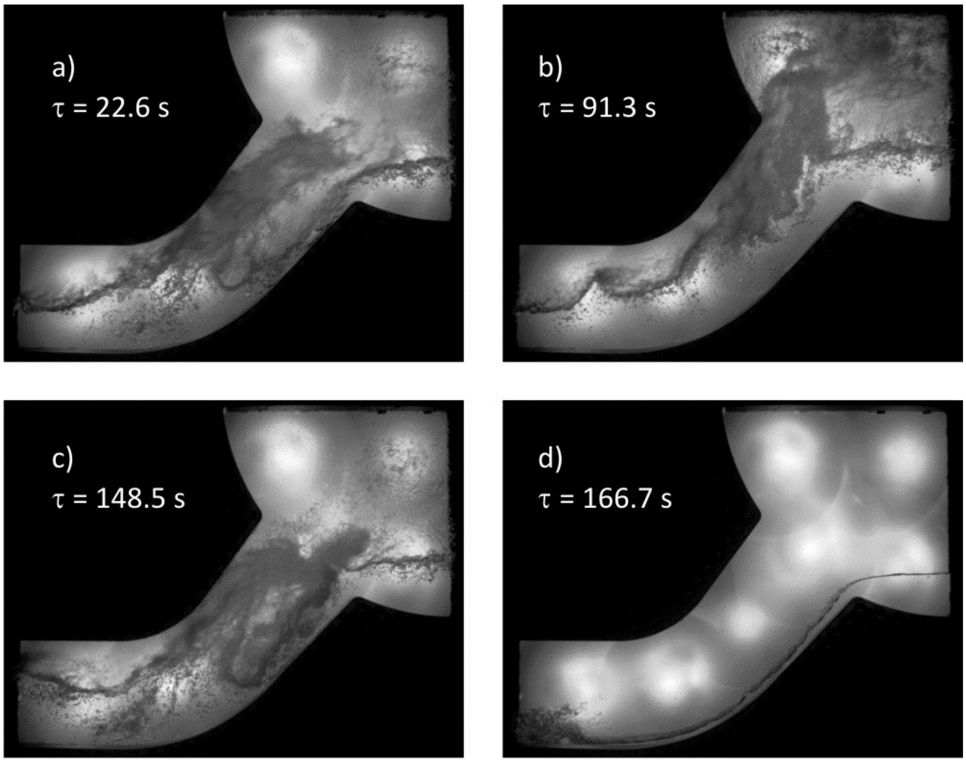

Fig. 6.20: high-speed camera pictures of experiment 06-18

6.4.2 Flooding characteristics of the hot leg model

6.4.2.1 Data processing method

The plot of the gas flow rate versus the discharge water flow rate during CCFL leads to the flooding characteristic. In order to automate the arrangement of the flooding diagram, a data treatment routine was developed. The water level in the separators is subject to different short time disturbances which result in high frequent variations of the measured signal. These variations get amplified during the numerical differentiation, which is needed for the calculation of the volumetric current. The water level signal had to be damped with a low-pass filter before differentiation, in order to avoid large fluctuations.

Technically, the low-pass filter was applied by multiplying a Gaussian weight function (see Equation 6.2) to each time step of the water level signal (see Equation 6.3).

$$\beta(\Delta\tau) = \exp(-\Delta\tau^2\omega^2) \tag{6.2}$$

$$L^*_i = \frac{\sum_{j=i-k}^{i+k} L_j \cdot \beta(\tau_i - \tau_j)}{\sum_{j=i-k}^{i+k} \beta(\tau_i - \tau_j)} \text{ , } i = 1..m \text{ , } k = \min(i-1, m-i, 25) \tag{6.3}$$

The remaining fluctuation of the resulting dumped water level signal L^* mainly depends on the width $T = \omega^{-1}$ of the weight function β; which represents the cut-off frequency ω of the low-pass filter.

After the low pass filtering, the time derivative of the water level was calculated, which is used to calculate the superficial velocity of the water according to equation 6.4.

$$j_{L,i} = \frac{L^*_i - L^*_{i-1}}{\tau_i - \tau_{i-1}} \cdot \frac{A_S}{A_C} \tag{6.4}$$

The areas of the water surface in the separator A_S and the cross section of the channel $\mathrm{A_C}$ is used to convert the velocity of rising water level in the separators into a flow velocity through the channel. The superficial liquid velocity $j_{L,i}$ is calculated for each time step i, using the one before (i-1).

Figure 6.21 shows the superficial velocity of the water and the gas for the above experiment 06-14. It starts with a liquid superficial velocity of 0.06 m/s and increasing gas velocities of 2.2 m/s to 2.6 m/s. With the gas velocity step from 2.6 m/s to 2.9 m/s the water discharge superficial velocity drops down to approximately 0.02 m/s. With increasing gas velocity up to 3.15 m/s, the liquid discharge velocity dropped down to 0.003 m/s. Shutting down the gas injection leads to an increase in water drainage, which is represented by a line towards the bottom right in the diagram.

In order to find a number of representative points, we defined some criteria that had to be fulfilled for representative and stationary points shown in figure 6.22. In order to select only points on the flooding curve, the pressure difference between the separators had to be above 5 kPa. Furthermore, we decided to exclude the transition processes between the stationary flooding conditions, so a limit is defined for the fluctuation of both velocities. The time derivative of the liquid discharge velocity should not exceed 0.0005 m/s², while the gas velocity change had to stay below 0,01 m/s². Moreover, the water feeding and drainage valves of the RPV-simulator had to stay closed; otherwise, the volume balance is incorrect. If all the criteria are fulfilled, the point is selected.

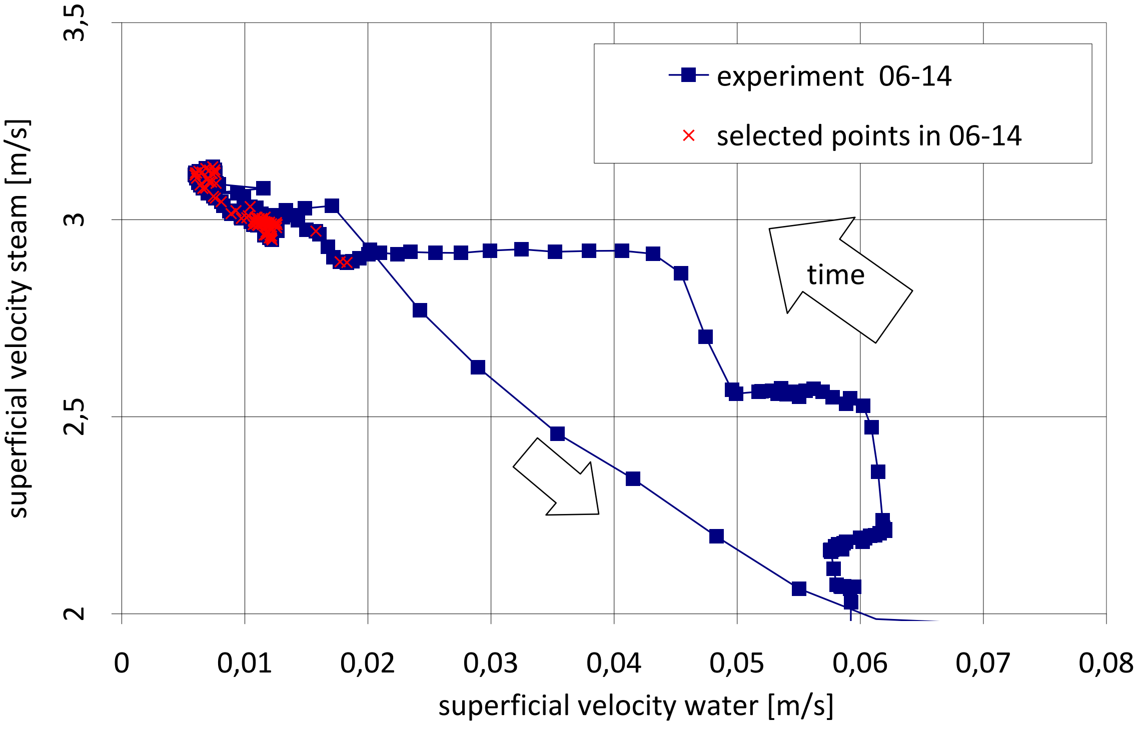

Fig. 6.21 superficial velocity plot of CCFL experiment 06-14

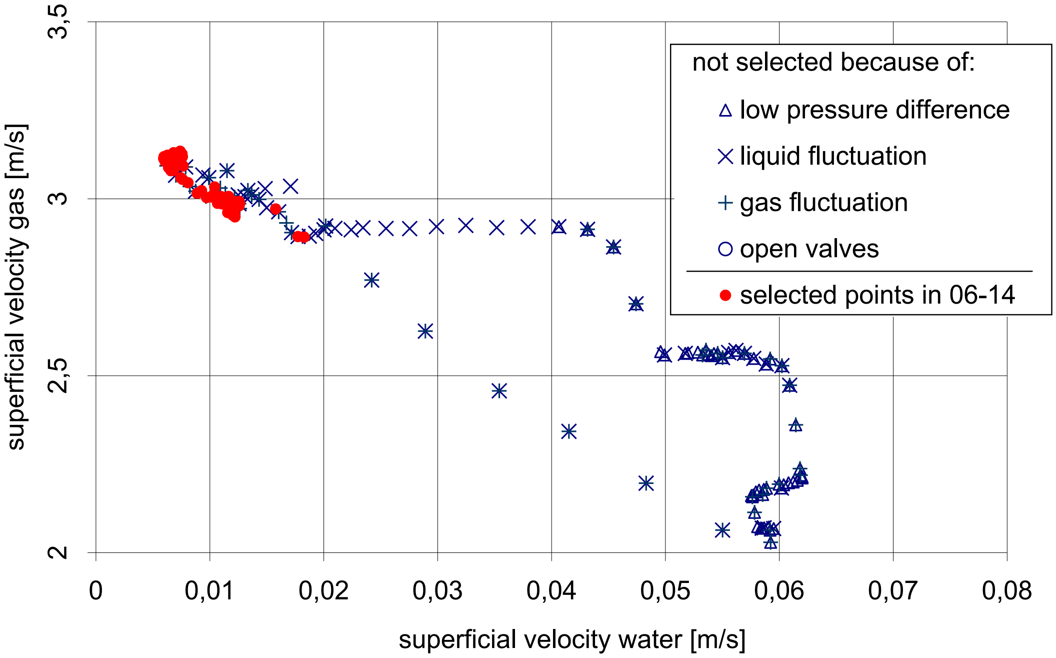

Fig. 6.22 superficial velocity plot with criteria for the selection of representative points

6.4.2.2 Flooding characteristics in the Wallis parameter diagram

For a meaningful comparison of experiment data, the non-dimensional superficial velocity J^*_i (or *Wallis parameter*) is commonly used to plot the flooding diagram for the phase *i*. This was defined by Wallis & Dobson (1973) for near horizontal channels with rectangular cross-section as follows:

$$J_k^* = \frac{j_k}{\sqrt{g \cdot D}} \sqrt{\frac{\rho_k}{\rho_L - \rho_G}} \tag{6.5}$$

The Wallis parameter is convenient for all types of comparisons because it is a non-dimensional parameter; it takes the effect of the pressure on the fluid densities into account.

The superficial velocity j_G and the dimensionless superficial velocity J^*_G of the gas flow were determined using the steam mass flow rate $\dot{m}_G$ or the air volumetric current $\dot{V}_G$ respectively. The volumetric current was divided by the density to obtain the mass flow rate. The dimensionless velocity J^*_L of the discharge liquid flow was also calculated according to equation 1.2.

For all the experiments, the points belonging to the flooding curve according to the described method were plotted in terms of the square root Wallis parameter in Figure 6.23. This shows the typical decreasing trend of the experimental points, indicating that during CCFL an increase of the gas flow rate decreases further the discharge water flow rate. Furthermore, Figure 6.23 reveals a clear segregation between the air/water and steam/water experiments: mainly due to a higher zero penetration point (interception of the flooding curve with the ordinate axis), the flooding of the steam/water flows was obtained at higher non-dimensional gas superficial velocities.

There was no significant relaxation or hysteresis identified in the comparison between flooding and deflooding experiments (not explicitly shown here).

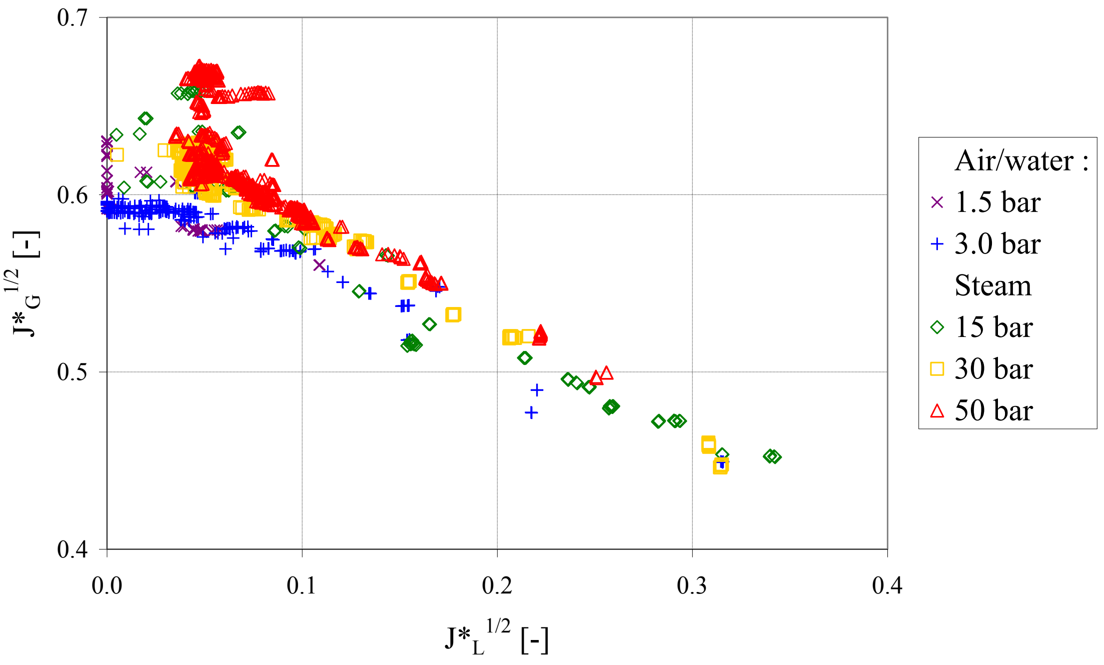

Fig. 6.23 Flooding characteristics of the hot leg model plotted in terms of the Wallis parameter

6.4.2.3 Flooding characteristics in the Kutateladze number diagram

To clarify the reason for the difference between air and steam experiments, other parameters than the Wallis parameter were used to correlate the CCFL data. One of them is the Kutateladze number which is commonly used to correlate flooding experiments in vertical flows through perforated plates (cf. Hawighorst et al., 1984 and No et al., 2005). This non-dimensional number is defined as:

$$K_k = j_k \left(\frac{\rho_k{}^2}{g \cdot \sigma \cdot (\rho_L - \rho_G)} \right)^{1/4}, \; k \in \{L, G\} \tag{6.6}$$

The Kutateladze number includes the surface tension σ and therefore one essential physical property of the fluids which was varied indirectly with the temperature in our experiments. Furthermore, according to Kim & No (2002), this is used with the Wallis parameter as a second possibility to predict counter-current flow limitation in the hot leg in the one-dimensional system code RELAP5.

As shown in Figure 6.24, the Kutateladze number also fails to correlate our flooding data, in particular the air/water and the steam/water experimental series. Furthermore, the steam/water series at 15, 30 and 50 bar tend to separate in the Kutateladze diagram compared to the Wallis diagram. These results show that the surface tension obviously does not explain the observed discrepancy.

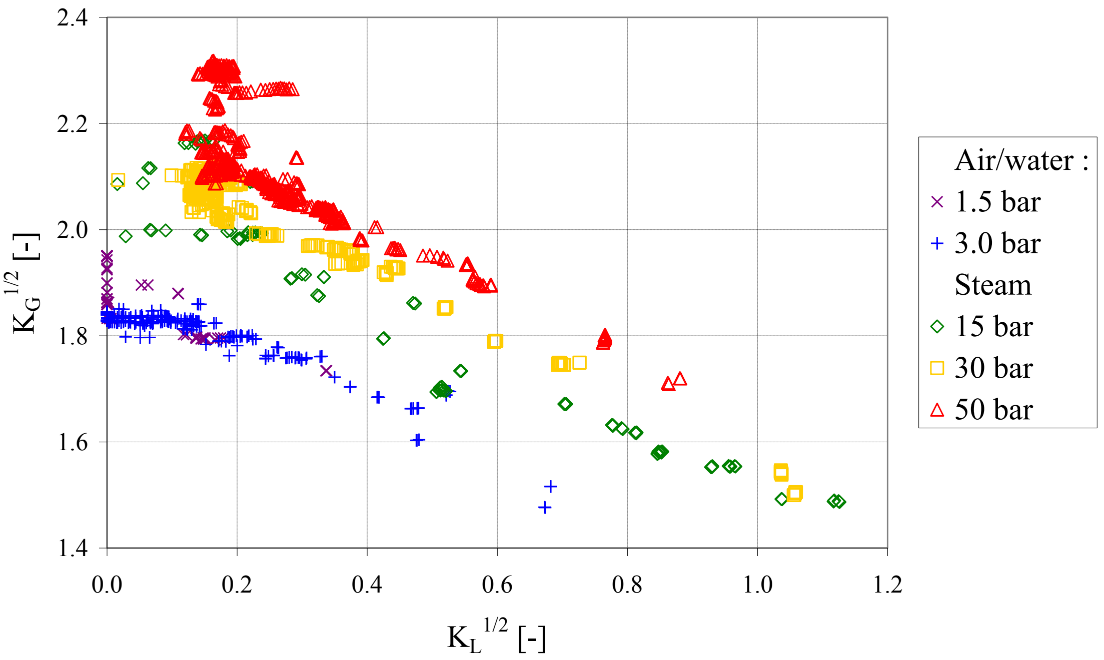

Fig. 6.24 Flooding characteristics of the hot leg model plotted in terms of the Kutateladze number

6.5 Consideration of the Effects of Wet Steam

As shown in the previous sections, the classical Wallis parameter and Kutateladze number both fail to properly correlate our flooding data. Discrepancies were found especially between the experimental series conducted with air/water on the one hand and steam/water on the other hand. The steam quality is one of the main uncertainties arising while conducting steam/water experiments. It can be deteriorated for instance by condensation in the system. Since these undesirable effects may explain the observed discrepancies, this issue is discussed in the following sections.

6.5.1 Qualitative considerations

The steam quality, and in particular condensation caused by heat losses in the test facility, could affect the effective gas flow rate available for flooding. In fact, the steam flow rate being measured upstream of the test section, an overestimation of the amount effectively streaming through the test section is possible. This explanation matches the fact that the gaseous Wallis parameter needed to reach flooding with steam/water was found to be higher than that with air and water. Unfortunately, no specific instrumentation was available during the experiments which could be used to measure the quality of the steam injected into the test section. Furthermore, no dedicated test was performed to estimate directly or indirectly the arising amount of liquid.

Nevertheless, in Figure 6.23 and 6.24 it is remarkable that zero liquid penetration was clearly reached during the air/water experiments (especially at 1.5 bar), but apparently not during the steam/water experiments. However, this observation becomes surprising when noticing that the flooding characteristics of the steam experiments present obviously two different parts:

- for $J^{*}_{L}{}^{1/2} > 0.05$ or $K_L^{1/2} > 0.2$ (in Figure 6.23 or 6.24 demonstrates that with this correction term, a good correlation can be achieved between the low pressure air/water and the high-pressure steam/water experiments), the CCFL characteristics describe a line almost parallel to that of the air/water experiments;

- for smaller parameters, the steam/water flooding points present a nearly vertical trend.

The nearly vertical evolution of the flooding characteristics at low liquid discharge flow rates is particularly distinctive for the 50 bar experiments (cf. diagrams). However, this trend is abnormal in a CCFL diagram plotted in terms of the square root of non-dimensional parameters. In fact, according to the knowledge of the authors, such behaviour has never been described in the relatively abundant CCFL literature.

Consequently, we will suppose hereafter that the nearly vertical part of the flooding characteristics is caused by a steam quality lower than unity. In that case, the liquid transported by the steam into the test section is likely to accumulate in the RPV simulator: due to the large cross-section, this is a place of low gas velocities and, furthermore, the lowest point of the overall experimental apparatus. If this hypothesis is right, the RPV simulator is filled on the one hand by the discharge water, but also by mist flowing with the steam on the other hand. This means that the method used to measure the discharge water flow, which is based on the water level increase in the RPV simulator, could include a disturbance due to a poor steam quality. In that case, the water level in the RPV simulator further increases also after the zero liquid penetration has been reached due to the parasitic liquid included in the steam. According to this analysis, the nearly vertical part of the steam/water flooding characteristics in Figures 6.23 and 6.24 should correspond to the zero liquid penetration. However, it has to be mentioned that the plot of the square root of the nondimensional parameters leads to a distortion of the diagram which enlarges distances close to the zero liquid penetration. This effect emphasises graphically the problem already at small liquid amounts.

6.5.2 Quantification of the parasitic amount of liquid

Following the reasoning of previous section, the flooding characteristics of the steam/water experiments have to be corrected in order to take into account the effects of a poor steam quality. A determination of the parasitic amount of liquid in retrospect is only possible over the abscissa of the near vertical part of the CCFL characteristics. In order to improve the statistical sample size, this amount of liquid is supposed to depend only on the system pressure. Consequently, for the determination of the parasitic amount of water, the flooding points were plotted in terms of the mass flow rate separately for each of the three pressure levels. As shown exemplarily for the experiments performed at 30 bar in Figure 6.25, the two regions of this CCFL diagram have been delimited by a line. The coordinates of the line were chosen manually to isolate above the points belonging to the zero liquid penetration. Finally, the parasitic liquid flow rate was calculated from the average abscissa of the selected points. At 30 bar, 33.7 g/s of water were obtained (cf. Figure 6.25), which corresponds to a vapour quality of 96.0% with the steam flow rate of about 0.8 kg/s measured during zero liquid penetration. Furthermore, this represents a liquid mass fraction of 4.2% or a volume fraction of only 0.8‰.

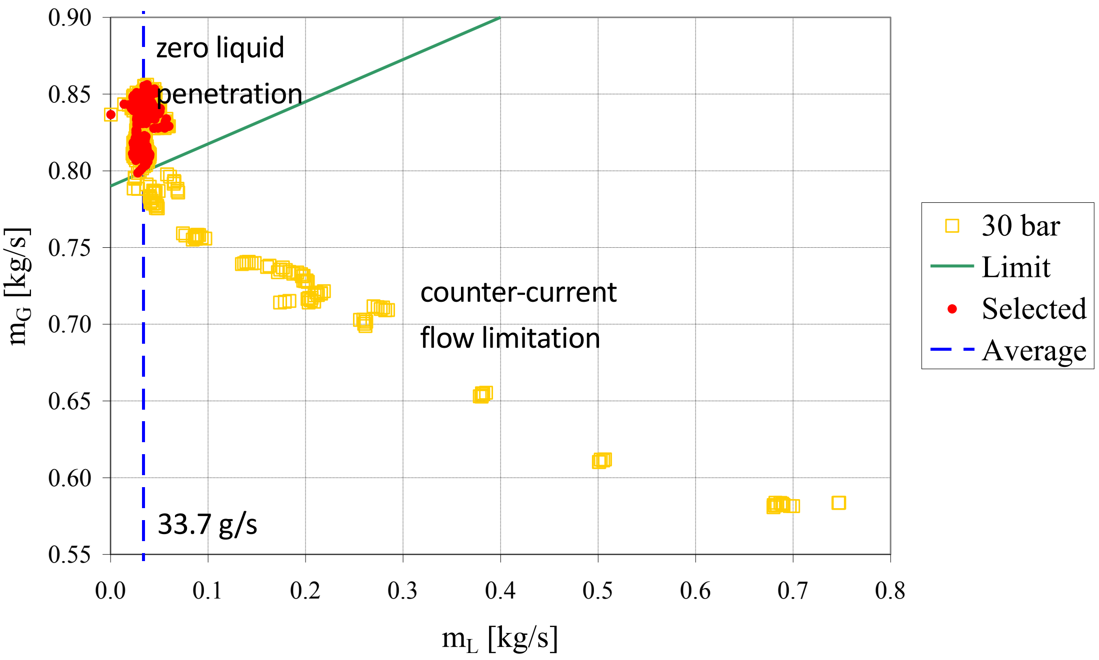

Fig. 6.25 Selection of the flooding points belonging to the zero liquid penetration (example for the 30 bar experiments - see table 6.3)

For the correction of the flooding characteristics, the obtained condensation rate $\dot{m}_c$ was subtracted from the discharge water flow $\dot{m}_L$ as well as from the measured steam flow rate $\dot{m}_G$ as follows:

$$\dot{m}_{L,\,corr}(t,p) = \dot{m}_L(t) - \dot{m}_c(p) \tag{4.1}$$

$$\dot{m}_{G,\,corr}(t,p) = \dot{m}_G(t) - \dot{m}_c(p) \tag{4.2}$$

The flooding characteristics obtained after application of the correction taking into account the condensation effects is presented in figure 6.26 and 6.27 in terms of the Kutateladze number and Wallis parameter, respectively. In the Kutateladze diagram, the agreement between the experimental series is not significantly improved by the correction (cf. fig. 6.24). In contrast, the plot in terms of the Wallis parameter shows a reasonable agreement between all the CCFL series, especially considering the scatter of the data (fig. 6.23). Consequently, this result corroborates the hypothesis made in previous section concerning the effect of heat losses and supports the method used to estimate the condensation rate. Furthermore, this shows that the Wallis similarity is appropriate to scale flooding in the hot leg of a PWR over a large range of pressure and temperature conditions. In particular, no significant discrepancy could be observed between the air/water and steam/water series, although the fluid properties vary noteworthy. This confirms the results of Ohnuki (1986) obtained in smaller scale pipes and over a more limited range of boundary conditions (atmospheric pressure). Consequently, the influence of viscosity and surface tension on the flooding characteristics described in the literature for vertical and inclined pipes seems not to be transferable to the hot leg geometry or to the couple of fluids air/water and steam/water. Finally, the flooding characteristics of the hot leg model can be approximated with the following linear regression function:

$$(J^*{}_G)^{1/2} + 0.533 \cdot (J^*{}_L)^{1/2} = 0.61 \tag{4.3}$$

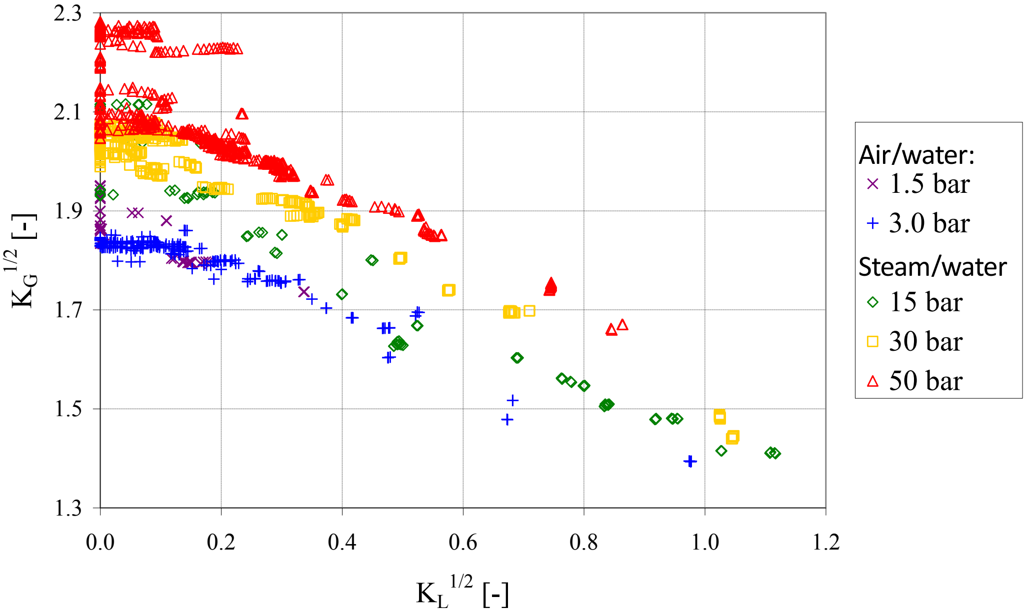

Fig. 6.26: Flooding characteristic of the hot leg model plotted in terms of the Kutateladze number after correction of the steam condensation effects

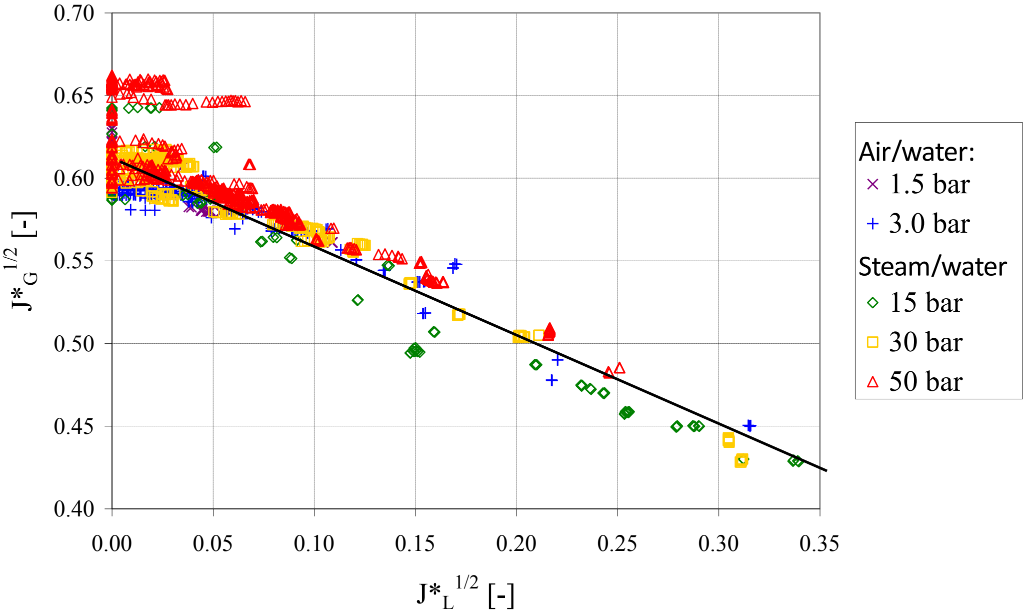

Fig. 6.27: Flooding characteristic of the hot leg model plotted in terms of the Wallis parameter after correction of the steam condensation effects

6.5.3 Plausibility check for steam condensation

In order to further support or invalidate the hypothesis of parasitic water entrainment in the steam flow, it was attempted to identify its origin. Therefore, a plausibility check concerning heat losses and the resulting steam condensation was performed. Indirectly it is possible to evaluate approximately the steam condensation amount over three different ways:

1. During other experimental series, steam flow rates down to 0.035 or 0.075 kg/s were injected in the test section. The high-speed camera observations indicate that steam was still flowing

through the riser of the hot leg. Therefore, the condensation amount must be significantly lower than 0.075 kg/s.

2. The heat flux released to the atmosphere over the air/air heat exchanger used to cool the inner atmosphere of the pressure chamber (see Fig. 2.3) was measured during the experiments. This heat flux was lower than 40 kW, which represents at 50 bar about 0.024 kg/s of steam condensation in the pressure chamber. Although this value only includes the heat losses of the components inside of the pressure chamber, this is in agreement with the maximisation of the condensation amount performed in the previous point.
3. The condensation rate in the steam line was evaluated with a theoretical model. The empirical correlations recommended by the VDI-Wärmeatlas (1994) were used to calculate the heat flux through the insulation as well as the natural convection around the line. At each pressure level, steam saturation temperature was assumed at the outer wall of this DN100 pipe and the room temperature was supposed to be 20°C. The temperature dependency of the heat conduction of the insulation material was modelled with a polynomial function of the second degree according to the material properties for rock wool indicated in the VDI-Wärmeatlas (1994). Furthermore, the outer diameter of the steam line was set to 260 mm after measurements performed in the test facility and its total length (i.e. from the TOPFLOW separator outlet to the inlet of the pressure vessel) was evaluated to 44 m according to isometric drawings. Because of the complicated pipe routing, the natural convection was calculated with the correlations for horizontal pipes on one hand and for vertical pipes on the other hand. The temperature of the outer surface of the insulation material constitutes the interface between both models. Consequently, this was calculated iteratively in order to get convergence between the heat fluxes through the insulation and the heat losses due to natural convection. The correlations for natural convection around horizontal and vertical pipes lead to differences of less than 1%, therefore, the average values were taken. Heat losses of up to 4.4 kW were calculated, representing a maximum condensation rate of 2.6 g/s. Although the insulation conditions of the line are for sure worse compared to the model assumptions, the calculation results are about one order of magnitude lower than the heat losses measured in the pressure vessel. Consequently, the condensation effects along the steam line are probably of second order.

For the different possibilities mentioned previously, the variation of the evaluated amount of condensate in function of the pressure level is shown in Table 2. Furthermore, this is illustrated comparatively in figure 6.28 with base 100 at 50 bar. This comparison points out that the amount of condensate due to heat losses in the pressure chamber (from measurements of the cooling power) or in the steam line (from calculations) depends strongly on the pressure. However, the evolution of the parasitic amount of water measured from the zero liquid penetration ($\dot{m}_{ZLP}$, cf. previous section) is significantly less sensitive to the pressure. Besides of the absolute values, these different trends reveal that the water level increase measured in the RPV simulator after reaching zero liquid penetration is probably not only due to heat losses and the resulting steam condensation.

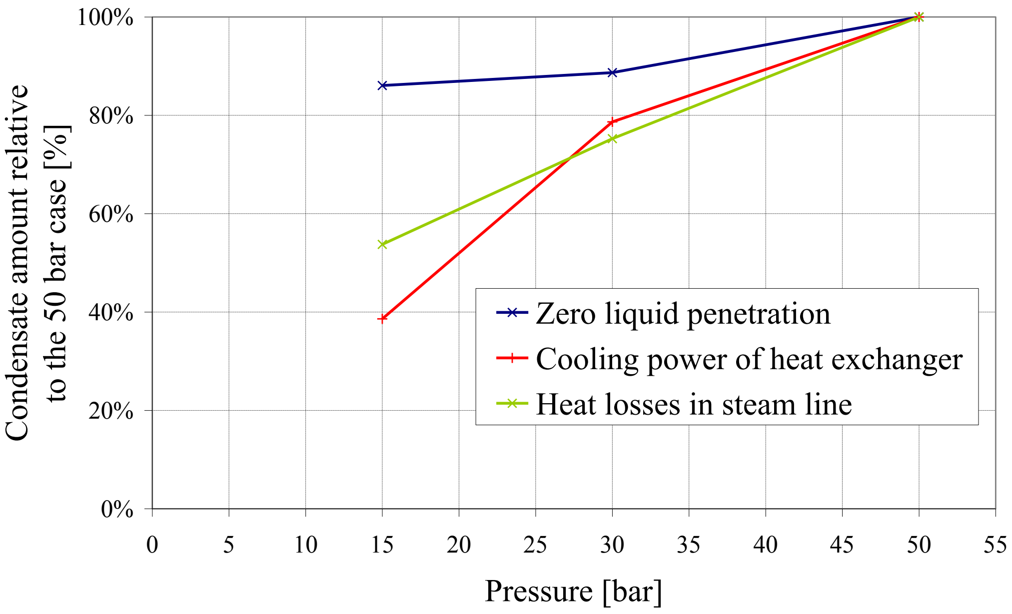

Fig. 6.28 Evolution of the relative amount of condensate in function of the system pressure (base 100 at 50 bar)

Table 6.3: Comparison of the amount of condensate determined by different methods

Pressure	$\dot{m}_{ZLP}$	(1) min. $\dot{m}_S$	(2) Cooling heat exchanger		(3) Heat losses in steam line	
[bar]	[g/s]	[g/s]	Power [kW]	$\dot{m}_{cond}$ [g/s]	Power [kW]	$\dot{m}_{cond}$ [g/s]
15	32.7	35	16.5	8.5	2.78	1.43
30	33.7	75	31	17	3.59	2.00
50	38.0	75	36	22	4.36	2.66

6.5.4 Plausibility check on liquid entrainment from the steam/water separator

Another parasitic source of liquid water in the steam line could be liquid entrainment from the separator of the heater circuit of the TOPFLOW test facility. In fact, the steam flow rate needed to reach CCFL, and a fortiori zero liquid penetration, is relatively high and a perfect separation of the two-phase flow in the separator cannot be guaranteed. During previous experimental series conducted at the TOPFLOW test facility, liquid entrainment has already been observed with help of conductivity probes installed in the steam line above the separator. Unfortunately, this instrumentation has been removed in the meantime and was not available during the hot leg experiments in order to support this hypothesis.

Therefore, again a dedicated plausibility check was performed. As shown in Table 6.4, the steam superficial velocity in the outlet pipe of the TOPFLOW separator is higher than 10 m/s at zero liquid penetration. In order to have an idea of the flow pattern reached in this section at such gas velocities and high void fractions, the flow regime transition-model for vertical pipes proposed by Taitel et al.

(1980) was used. According to their analysis, annular flow can only exist if the gas flow rate is sufficient to raise the droplets entrained in the gas core. Consequently, if the developed model predicts annular flow, the steam flow is likely to entrain liquid water out of the separator. The criterion proposed by Taitel et al. (1980) to describe the transition to annular flow is only a function of the fluid properties:

$$j_G = 3.1 \cdot \frac{(\sigma \cdot g \cdot \Delta\rho)^{1/4}}{\sqrt{\rho_G}} \tag{6.7}$$

The flow transition velocity was calculated accordingly in function of the pressure level as shown in Table 6.4. A comparison with the flow conditions at zero liquid penetration reveals that the superficial velocity is far above the transition, confirming that the steam injected into the hot leg model is probably wet.

Moreover, the liquid entrainment can explain why the parasitic amount of water measured over the zero liquid penetration is almost independent on the pressure. In fact, the superficial velocity at zero liquid penetration decreases with an increase of pressure (cf. Table 6.4). As a result, the amount of entrained water is expected to decrease as well. The dependency of the heat losses to the system pressure being inverse, the superposition of both effects can lead to a mutual compensation.

Table 6.4: Evolution of the steam flow rate at zero liquid penetration
in function of the pressure

Pressure level	$\dot{m}_S$ @ zero liquid penetration	j_S @ separator outlet	j_S @ transition to annular flow
[bar]	[kg/s]	[m/s]	[m/s]
15	0.67	24.8	4.76
30	0.80	15.0	3.14
50	1.05	11.6	2.22

All in all, liquid entrainment from the TOPFLOW separator is probably an important source of the parasitic water accumulating in the RPV simulator during zero liquid penetration. Although this hypothesis does not put into question the qualitative considerations of section 6.5.1, this has consequences on the correction of the flow rates. In fact, the assumption that the condensation rate only depends on the pressure level is legitimate, but the amount of entrained liquid should additionally be a function of the steam flow rate. Furthermore, both terms should be considered independently in the correction functions (cf. equations (4.1) and (4.2)) because the liquid entrainment only affects the discharge liquid flow. This means that the contributions of heat losses and liquid entrainment should be determined separately. As this is not possible in retrospect from the available data, dedicated experiments should address these uncertainties in a second experimental campaign.

6.6 Correction of the flooding characteristics

Finally, the parasitic water accumulating in the RPV simulator during zero liquid penetration is probably due to both steam condensation and liquid entrainment from the TOPFLOW separator. Consequently, for a proper correction of the flooding characteristics, the single contribution of each effect should be determined separately. In fact, liquid entrainment only affects the discharge liquid flow, while steam condensation also reduces the steam flow rate. Furthermore, the condensation rate probably only depends on the pressure level, but the amount of entrained liquid should additionally be a function of the steam flow rate. As these effects cannot be quantified in retrospect from the available data, only two limit cases are investigated here.

For the correction of the flooding characteristics, independently of its origin, the obtained parasitic amount of water $\dot{m}_{ZLP}$ was subtracted from the discharge water flow $\dot{m}_L$ as follows:

$$\dot{m}_{L,\,corr}(t,p) = \dot{m}_L(t) - \dot{m}_{ZLP}(p) \tag{6.8}$$

This is the sole needed correction while assuming that the parasitic water originates just from liquid entrainment. However, if on the contrary, the parasitic water is only due to steam condensation, its amount should be subtracted from the measured steam flow rate $\dot{m}_G$ as well, leading to:

$$\dot{m}_{G,\,corr}(t,p) = \dot{m}_G(t) - \dot{m}_{ZLP}(p) \tag{6.9}$$

The flooding characteristics obtained after application of these corrections for the limit cases are presented in terms of the Wallis parameter in Figure 6.29. On one hand, assuming liquid entrainment only (Figure 6.29-a), a small discrepancy between the air/water and steam/water experiments is observed. On the other hand, in case of pure steam condensation (Figure 6.29-b), a good agreement between all the experimental series is obtained. As the parasitic water is probably due to a combination of both effects, the real CCFL characteristics of the steam experiments should be in between of the investigated limit cases. This means that a slight difference may remain between the air and steam experiments. However, considering the scatter of the data as well as the remaining uncertainties, one can speak of a reasonable agreement between all the measured CCFL series. Consequently, this result shows that the Wallis similarity is appropriate to scale flooding in the hot leg of a PWR over a large range of pressure and temperature conditions. In particular, no significant discrepancy could be observed between the air/water and steam/water series, although the fluid properties vary noteworthy. This confirms the results of Ohnuki (1986) obtained in smaller scale pipes and over a more limited range of boundary conditions (atmospheric pressure).

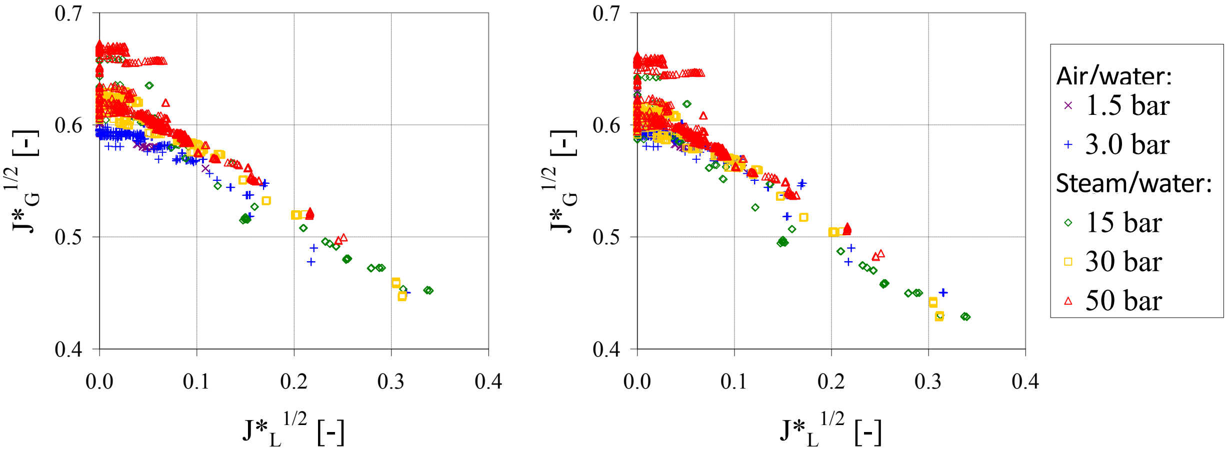

(a) Only liquid entrainment (b) Only steam condensation

Fig. 6.29 Flooding characteristic of the hot leg model plotted in terms of the Wallis parameter after correction of the steam quality effects

6.7 Comparison with the Results obtained at UPTF

The counter-current flow limitation in a hot leg was investigated at the original power plant scale in the Upper Plenum Test Facility (UPTF) during the dedicated test series n°11 reported by Weiss & Hertlein (1988) and in Siemens/KWU (1987). The experiments were performed with steam and saturated water at pressures of 3 and 15 bar in order to check the applicability of the Wallis similarity to the original NPP geometry and boundary conditions. Furthermore, investigations were focused on the influence of the several meters long pipe of the *Hutze* (ECC nozzle placed at the bottom of the hot leg) with respect to the flooding behaviour. As a result, it was recommended to calculate the Wallis parameter based on the flow path in the region of the *Hutze*. This concerns in particular the flow cross-section A for the calculation of the superficial velocity and the hydraulic diameter D_h as length scale. Later on, this approach was supported by the small scale experiments of Ohnuki et al. (1988).

The resulting data points (calculated with $A = 0.3974\ \mathrm{m}^2$ and $D_h = 0.639$ m) are compared with the own flooding characteristics in Figure 6.30-a. For clarity reasons, only the experiments performed at the same pressure levels as those of UPTF were plotted: the air/water tests at 3 bar and the steam/water tests at 15 bar (denoted as “S/15 bar” in Figure 6.30, the series (*a*) and (*b*) corresponding to the limit cases indicated in Figure 6.29). Figure 6.30-a shows an approximate agreement between both experimental works: at UPTF the zero liquid penetration was obtained at higher gas fluxes and the slope of the flooding characteristics is steeper. Consequently, in a second comparison presented in Figure 6.30-b, the UPTF data points were recalculated with the geometrical parameters in the parts of the hot leg without *Hutze*: $A = 0.4418\ \mathrm{m}^2$ and $D_h = 0.750$ m. In that case, the overall agreement with the own results is better, in particular for the zero liquid penetration. This may indicate that flooding does not mainly occur along the *Hutze*. However, close inspection reveals that the slope is again too steep, especially close to zero liquid penetration. Since none of the geometrical considerations gives satisfying agreement, the observed differences may also be due to the rectangular cross-section of the TOPFLOW hot leg model. Nevertheless, with respect to the uncertainty of the data, the differences between both experimental series are acceptable and precise explanations would require dedicated investigations.

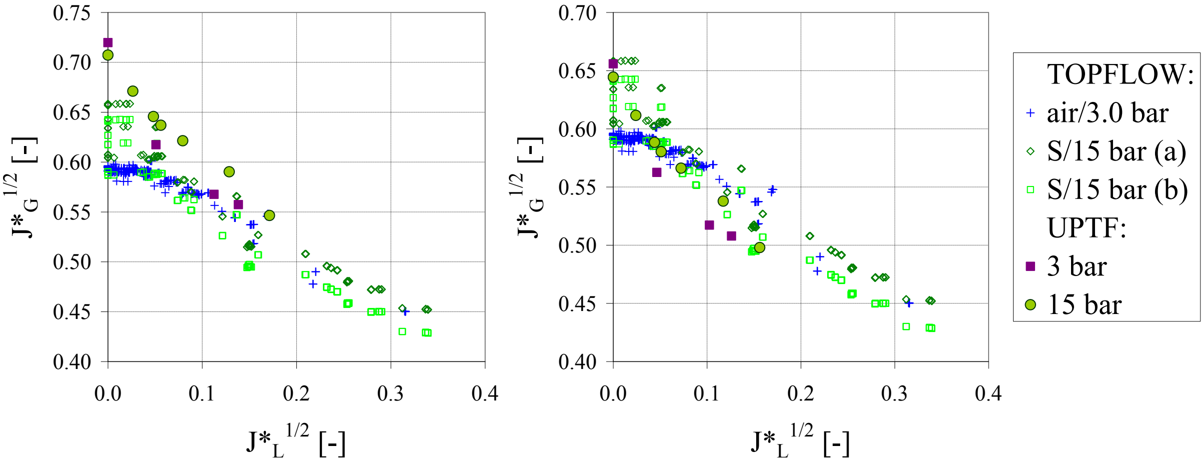

(a) With consideration of the *Hutze*

(A = 0.3974 m² / D_h = 0.639 m)

(b) Without consideration of the *Hutze*

(A = 0.4418 m² / D_h = 0.750 m)

Fig. 6.30 Comparison of the present data with the CCFL characteristics of UPTF (Weiss & Hertlein, 1988 and Siemens/KWU, 1987)

7 Summary and Outlook

This experimental report describes the complete evolution of the project related to the hot leg model experiments, from the design of the test facility to the analysis of the global parameters. The model of the hot leg has been designed, built and assembled for the pressurised tank in order to achieve the visual observation of large flow areas at high pressure. It helped developing the pressurized tank technology, being the first application for the tank. Especially the issues around thermal insulation and illumination had to be developed.

Finally, 194 Experiments have been performed at four different experiment types (co-current flow, counter-current flow, counter current flow limitation and flow without water injection), recording different process parameters (like temperature, pressure, mass flow and levels) and high-speed camera pictures at up to 100 Hz. The treatment of the conventional instrumentation leads to experimental data sheets and some analyses. For co-current flow experiments, RPV water level histograms have been shown. Water level plots, showing the relation between the water levels were processed for most of the experiments.

The flooding correlation has been calculated in terms of the Wallis parameter and the Kutateladze number. Because of a difference between air-water and steam-water experiments, a viscosity based correction function has been proposed and compared to available data from the literature.

Based on the experience gained during the execution and the analysis of the experiments, some improvements for a potential second series of tests could be identified. The images of the flow obtained with the fibre-optics illumination have shown that the light could not be distributed homogeneously with the 7 modules. This inhomogeneous background illumination emerges to make the image processing more difficult. If no proper correction algorithm can be found in future, a smoother illumination design should be developed for new experiments.

The observation of the flow in the bended region of the hot leg allows investigating the most important flow phenomena as slug formation and water recirculation. However, the additional observation of parts of the horizontal channel could be helpful for the comparison with CFD. In particular, during the CCFL experiments, the position of the hydraulic jump appears to be a very important at the onset of flooding.

The pressure difference between the separators appears to be a fast fluctuating value during slug flow; it is appropriate thou to increase its measurement frequency in order to see slug and plug frequencies in the horizontal channel.

In order to validate the viscosity ratio further as correction term for the Wallis correlation, CCFL experiments should be performed both, with low steam pressure and with high air temperature.

Steam injection into the RPV-simulator below the water surface would on the one hand keep the water saturated and on the other hand reproduce the reactor conditions better.

Using a recirculation pump could help increasing the range of possible water mass flow especially for co-current flow experiments.

In order to control the SG-separator level better, a overflow barrier inside the vessel is possible.

Literature

Asaka, H., Kukita, Y. (1996). Sub- to Supercritical Flow Transition in a Horizontally-Stratified Two-Phase Flow in PWR Hot Legs. Journal of Nuclear Science and Technology, Vol. 33/9, pp.696-702.

Beyer, M., Carl, H. (2004). Betriebshandbuch für die Mehrzweck-Thermohydraulicversuchsanlage TOPFLOW. Forschungszentrum Rossendorf, Wissenschaftlich-Technische berichte, FZR-405, Juli 2004, ISSN 1437-322X.

Damerell, P. S., Simons, J. W. (1993). Reactor Safety Issues Resolved by the 2D/3D Program. NUREG/IA-0127, U.S. Nuclear Regulatory Commission.

DIN EN ISO 5167-1 (2003). Durchflussmessung von Fluiden mit Drosselgeräten in voll durchströmten Leitungen mit Kreisquerschnitt – Teil 1: Allgemeine Grundlagen und Anforderungen.

Gardner, G. C. (1988). Co-current flow of air and water from a reservoir into a short horizontal pipe. International Journal of Multiphase Flow, Vol. 14/4, pp. 375-388.

Gardner, G. C. (1989). Air-water model studies of cocurrent flow into and along a PWR hot leg to the steam generator. Nuclear Engineering and Design, Vol. 117/3, pp. 251-261.

Gargallo, M., Schulenberg, T., Meyer, L., Laurien, E. (2005). Counter-current flow limitations during hot leg injection in pressurized water reactors. Nuclear Engineering and Design, Vol. 235/7, pp. 785-804.

Hawighorst, A., Kröning, H., Mayinger, F. (1984). Fluid dynamic effects in the fuel element top nozzle area during refilling and reflooding. Nuclear Science and Engineering, Vol. 88/3, pp. 376-385.

Kim, H. Y., No, H. C. (2002). Assessment of RELAP5/MOD3.2.2γ against flooding database in horizontal-to-inclined pipes. Annals of Nuclear Energy, Vol. 29, pp. 835-850.

Krolewski, S. M. (1980). Flooding Limits in a Simulated Nuclear Reactor Hot Leg. MIT, Submission as Part of Requirement for a B.Sc.

Kukita, Y., Nakamura, H., Anoda, Y., Tasaka, K. (1989). Hot leg flow characteristics during two-phase natural circulation in pressurized water reactor. Proceedings of the fourth International Topic Meeting on Nuclear Reactor Thermal Hydraulics (NURETH-4), Karlsruhe, Germany, Vol. 1, pp. 465-470.

Mayinger, F., Weiss, P., Wolfert, K. (1993). Two-phase flow phenomena in full-scale reactor geometry. Nuclear Engineering and Design, Vol. 145/1-2, pp. 47-61.

Minami, N., Nishiwaki, D., Kataoka, H., Tomiyama, A., Hosokawa, S., Murase, M. (2008). Experiments on air-water countercurrent flow in a rectangular duct simulating PWR hot leg. Proceedings of the 16th International Conference on Nuclear Engineering ICONE16 in Florida.

No, H. C., Lee, K.-W., Song, C.-H. (2005). An experimental study on air-water countercurrent flow limitation in the upper plenum with a multi-hole plate. Nuclear Engineering and Technology, Vol. 37/6, pp. 557-564.

Ohnuki, A. (1986). Experimental Study of Counter-Current Two-Phase Flow in Horizontal Tube Connected to Inclined Riser. Journal of Nuclear Science and Technology, Vol. 23, S. 219-232.

Petritsch, G., Mewes, D. (1999). Experimental investigations of the flow patterns in the hot leg of a pressurized water reactor. Nuclear Engineering and Design, Vol. 188/1, pp. 75-84.

Prasser, H.-M., Beyer, M., Böttger, A., Carl, H., Lucas, D., Schaffrath, A., Schütz, P., Weiß, F.-P., Zschau, J. (2005). Influence of the pipe diameter on the structure of the gas-liquid interface in a vertical two-phase pipe flow. Nuclear Technology, Vol. 152, pp. 3-22.

Prasser, H.-M., Beyer, M., Carl, H., Manera, A., Pietruske, H., Schütz, P., Weiß, F.-P. (2006). The multipurpose thermal-hydraulic test facility TOPFLOW: an overview on experimental capabilities, instrumentation and results. Kerntechnik, Vol. 71/4, pp. 163-173.

Prasser, H.-M., Beyer, M., Al Issa, S., Carl, H., Pietruske, H., Schütz, P. (2008). Gas-liquid flow around an obstacle in a vertical pipe. Nuclear Engineering and Design, Vol. 238, pp. 1802-1819.

Richter, H. J., Wallis, G.B., Carter, K.H., Murphy, S.L. (1978). Deentrainment and Countercurrent Air-Water Flow in a Model PWR Hot Leg. NRC-0193-9, U.S. Nuclear Regulatory Commission, Washington D.C.

Schaffrath, A., Krüssenberg, A.-K., Weiss, F.-W., Hicken, E. F., M. Beyer, H. Carl, J. Schuster, P. Schütz, M. Tamme. (2001). TOPFLOW - a new multipurpose thermalhydraulic test facility for the investigation of steady state and transient two-phase flow phenomena. Kerntechnik, 66/4, pp. 209-212.

Schmidt, H., Limprecht, H. (1991). Versuch PKL III B 3.4. Siemens/KWU Report No. KWU E312/91/16, Erlangen, Germany.

Schmidtke, M. (2008). Untersuchung der Dynamik fluider Partikel auf Basis der Volume of Fluid Methode. PhD Thesis, Fakultät für Naturwissenschaften, Universität Paderborn, Paderborn, Germany.

Tusheva, P., Reinke, N., Altstadt, E. (2009). Analysis of severe accidents in VVER-1000 reactors using the integral code ASTEC. 17th International Conference on Nuclear Engineering, ICONE17, Brussels, Belgium.

Vallée, C., Höhne, T, Prasser, H.-M., Sühnel, T. (2007). Experimental investigation and CFD simulation of slug flow in horizontal channels. Wissenschaftlich-Technische Berichte FZD-485, Forschungszentrum Dresden-Rossendorf, Dresden, Germany.

Wallis, G. B. (1969). One-dimensional two-phase flow. Mc Graw-Hill, New York, USA.

Wallis, G. B. & Dobson, J. E. (1973). The onset of slugging in horizontal stratified air-water flow. International Journal of Multiphase Flow 1, pp. 173-193.

Wan, P. T., Krishnan, V. S. (1986). Air-water flooding in an 90° elbow with a slightly inclined lower leg. Proceedings of the 7th Annual Conference in Toronto.

Wan, P. T. (1986). Countercurrent steam-water flow in an upright 90° elbow. Proceedings of the Eighth International Heat Transfer Conference in San Francisco.

Weiss, P. A., Hertlein, R. J. (1988). UPTF Test Results: First three separate Effect Tests. Nuclear Engineering and Desing, Vol. 108, pp. 249-263.

Weiss, P. (1992). UPTF-TRAM Versuch A2 – Ausbildung der Schichtenströmung in der heißseitigen Leitung. SIEMENS/KWU Quick Look Report S554/92/012, Erlangen, Germany.